Naval Research Laboratory
Washington, DC 20375-5350

NRL/MR/7130-xxxxxxxxxxx

Structural Acoustic UXO Detection and Identification in Marine Environments – Final Report to SERDP MR-2103

J. A. Bucaro[1]

[1]*On-Site Contractor with Excet, Inc.*
Springfield, VA 2215

A. Sarkissian, B.H. Houston, H. Simpson, Z.J. Waters, D. Amon,

Naval Research Laboratory
Washington, DC 20375

K. Jig, S. Liskey[2], and T. Yoder[2]

[2]*On-Site Contractor with Sotera Defense Technology & Systems, Inc.,*
Columbia, MD 21046

April 10, 2014

TABLE OF CONTENTS

LIST OF TABLES 1
LIST OF FIGURES 1
LIST OF ACRONYMS 4
KEYWORDS 4
ACKNOWLEDGEMENTS 4
ABSTRACT 5
Objective: 5
Technical Approach: 5
Results: 5
Benefits: 6
OBJECTIVE 7
BACKGROUND 7
MATERIALS AND METHODS 7
RESULTS AND DISCUSSION 8
Numerical Simulation Data Base 8
Sediment Pool Measurements 10
Feature Separation 11
Measurements at Duck, NC 16
Duck Exercise Details 18
Receiver Time Waveforms- Duck versus Sediment Pool facility 20
Numerical Simulation Results 21
Processed Duck Data 23
Scattering from Sediment Inhomogeneous Structure 37
Measurements in the Gulf of Mexico 41
Background 41
BOSS Exercises off the Coast of Panama City, FL 41
Analysis of BOSS Data 45
Overall Progress in Target Classification 55
CONCLUSIONS AND IMPLICATIONS FOR FUTURE RESEARCH/IMPLEMENTATION 58
LITERATURE CITED 59
APPENDICES 63
A. Supporting Data 63

B. List of Scientific/Technical Publications 65
C. Other Supporting Materials 66

LIST OF TABLES

TABLE 1 – Measurement Exercise Timeline
TABLE 2 – Signal Levels for Measurements and Simulations
TABLE 3 – Proud and Buried Target List

LIST OF FIGURES

Figure 1. Details for the two numerical simulations carried out for a buried five inch rocket for 90 vertical burial angles. Case 1 and 2 mimic the sediment pool and Duck, NC configurations, respectively.

Figure 2. Numerical results showing the plan view image and the narrow band x,y target strengths for several example rocket burial angles.

Figure 3. Sediment pool configuration and the eight buried targets.

Figure 4. Acoustic color plots (along x and y) for the rocket and no target case for both measurements and simulations.

Figure 5. Multi-dimensional feature spaces we have identified for the RVM identification algorithm with examples shown from numerical simulation results for the rocket buried at various vertical angles.

Figure 6. RVM feature separation performance based on numerical simulations vs receiver array area. Red lines are for the rocket UXO buried horizontally and nose down 30° and blue lines for the rock, cinderblock, and rolled cinderblock.

Figure 7. Definitions for the symmetry feature and for the target strength correlation feature. TS is the target strength and F and G are the upper and flipped lower half of the plan view images.

Figure 8. Target feature separation using a discriminatively trained RVM classification algorithm for the four buried targets shown above.

Figure 9. Target feature separation using a discriminatively trained RVM classification algorithm for the four buried targets shown below using all 90 burial angles in the training.

Figure 10. Target feature separation using a discriminatively trained RVM classification algorithm for the seven buried targets shown below using all 90 burial angles in the training.

Figure 11. Target feature separation using a discriminatively trained RVM classification algorithm for the seven buried targets shown below using all 90 burial angles in the training. Here the rockets and 155mm shell are the targets of interest.

Figure 12. Generatively trained RVMalgorithm using only the simulatedrocket data for 90 burial angles.

Figure 13. Buried target ID in the sediment pool using the numerically trained RVM classifier shown in Fig. 12.

Figure 14. Pier at Duck, North Carolina

Figure 15. ACE Field Research Facility

Figure 16. Rail look-down measurement system

Figure 17. The five inch rocket UXO

Figure 18. Rail-based measurement system dimensions

Figure 19. Rail-based sonardeployed using the coastal amphibious research buggy (CRAB)

Figure 20. Acoustic source time profile (upper-sediment pool and lower-Duck).

Figure 21. Numerical results for Duck simulation after time-alignment (target response increased by 10x)

Figure 22. Measured signals at the receivers (horizontal target)

Figure 23. Duck simulation with source convolution

Figure 24. Measured signals at the synthetic array receivers in the sediment pool facility

Figure 25. Preliminary processed data to extract target scattering levels.

Figure 26. Plan view image from Duck data and measured sediment pool data (horizontal)

Figure 27. Plan view image without time gate filtering of the initial specular return.

Figure 28. SA mechanism highlights in plan view rocket image.

Figure 29. Vertical side view images of rocket buried in sediment pool.

Figure 30. Depth-axial image (horizontal buried rocket target).

Figure 31. Depth-radial image (horizontal buried rocket target).

Figure 32. Depth images of rocket buried horizontally.

Figure 33. Depth images of rocket buried at 30 degrees.

Figure 34. Whitened symmetry feature versus target burial angle for Duck.

Figure 35. Whitened image correlation feature versus target burial angle for Duck.

Figure 36. Direct simulations with source convolution (left) and measure signals at receivers (right) with estimates of some of the echo level ratios at various times.

Figure 37. No target case for Duck measurements with 1m and 1/4m scattering locations indicated on the left.

Figure 38. Integrated levels seen in Fig 37 over all the receivers from 3.4ms out to 4.5ms.

Figure 39. Diagram used to compute the sediment scattering volume within various time windows.

Figure 40. Sandy sediment sound absorption (Kevin Williams, et. al. Ref. 18 .)

Figure 41. Predicted sediment scattering volume from Eq. 3 weighted by signal absorption versus window center depth.

Figure 42. Constructs to be generated from the BOSS scattering data.

Figure 43. General operations area for TREX-13 off the Coast of Panama City, FL.

Figure 44. Planned placement of the targets listed in Table 1.

Figure 45. Target locations relative to the east-west and north-south AUV flight paths.

Figure 46. Addition to Fig. 45 of the diagonal flight paths.

Figure 47. The six "constructs" described in Fig. 42 extracted from the measured data for the five buried 155mm shell.

Figure 48. The six "constructs" described in Fig. 42 extracted from the measured data for the three buried five inch rockets.

Figure 49. The six "constructs" described in Fig. 42 extracted from the measured data for the 120mm mortar, the rock, and the cinderblock.

Figure 50. Acoustic color plots (arbitrary decibel units), i.e. target scattering levels versus frequency and x position of the receiver for target N8, the 155mm shell buried nose-up 60 degrees. We have illustrated beneath the plots the various source (black sphere) and receiver (blue bar) locations along x to help one visualize the source/receiver angles relative to the x axis of the color plots.

Figure 51. Acoustic color plots (arbitrary decibel units), i.e. target scattering levels versus frequency and x position of the receiver for target N6, the five inch rocket buried horizontally. We have illustrated beneath the plots the various source (black sphere) and receiver (blue bar) locations along x to help one visualize the source/receiver angles relative to the x axis of the color plots.

Figure 52. Acoustic color plots for N6 the 155mm shell buried horizontally. On the left, earlier measurement made in the sediment pool facility versus angle with the target proud. On the right, BOSS measurement (arbitrary decibel units) versus x position with target buried.

Figure 53. Acoustic color plots (arbitrary decibel units), i.e. target scattering levels versus frequency and x position of the receiver for target N9, the 120mm mortar buried horizontally. We have illustrated beneath the plots the various source (black sphere) and receiver (blue bar) locations along x to help one visualize the source/receiver angles relative to the x axis of the color plots.

Figure 54. Probability that a target detected on a particular receiver is a UXO.

Figure 55. Probability that a target detected on a particular receiver is a UXO using the product of the probabilities shown in Fig. 54.

Figure 56. Elastic highlight image of 5inch rocket observed in the sediment pool (top).UXO geometry with color indicating each mechanism (bottom).

Figure 57. Example of an actual sediment profile obtained with EdgeTech's sub-bottom profiler off the coast of Boston.

Figure A1. Photograph of BOSS in the Water.

Figure A2. Plan view and head-on view of BOSS.

Figure A3. Photograph of BOSS prior to complete assembly showing some of the internal components.

Figure A4. Preliminary 3-D images obtained from June 23, 2014 BOSS data by Richard Holtzapple and Nick Pineda.

LIST OF ACRONYMS

ACE Army Corp of Engineers
AUV Autonomous Underwater Vehicle
BOSS Buried Object Scanning Sonar
CRAB Coastal Amphibious Research Buggy
DVL Doppler Velocity Log
FEA Finite Element Analysis
FM Frequency Modulated
FRF Field Research Facility
GDA Goal Driven Autonomy
ID Identification
IMU Inertial Measurement Unit
NRL Naval Research Laboratory
NSWC-PCD Naval Surface Warfare Center – Panama City Division
POMDP Partially Observable Markov Decision Process
RMS Root Mean Squared
RVM Relevance Vector Machine
ROC Receiver Operating Characteristic
SA Structural Acoustic
SAS Synthetic Aperture Sonar
S/N (SNR) Signal to Noise
STARS – (STARS3D) Structural Acoustics and Radiation Three Dimensional (Code)
TREX Transmission and Radiation Experiments
TS Target Strength
UUV Unmanned Underwater Vehicle
USACE-CEERD-HC - United States Army Corp of Engineers – Engineer Research and Development Center, Field Research Facility, NC
UXO Unexploded Ordnance

KEYWORDS

Underwater Buried UXO, structural acoustic target identification, sonar UXO detection

ACKNOWLEDGEMENTS

This work was performed under direct support from the SERDP Program Office. We would like to acknowledge the very positive and encouraging program management role played by Dr. Herb Nelson, SERDP Program Manager for Munitions Response. We would also like to acknowledge the significant impact made in these studies by the leveraging of results from scientifically related efforts funded by ONR.

ABSTRACT

Objective:

Many active and former military installations have ordnance ranges/training areas with adjacent water environments in which unexploded ordnance (UXO) now exists due to wartime activities, dumping, and accidents. SERDP goals require the development of innovative technologies able to separate UXO from false targets and to discriminate amongst UXO targets themselves. The objective of this program is to address the scientific and technical issues whose resolution would result in an efficient, high performance structural acoustic (SA) feature-based underwater sonar technology that can detect and localize buried (and proud) targets and separate the detections into UXO vs non-UXO. Our focus is on marine-based sonars that could look both downward (and sideways) in water depths ranging from several meters to tens of meters. The goal here is to develop a sonar approach which results in robust identification algorithms based on structural acoustic features and complementary 3-D SAS (synthetic aperture sonar) images and to demonstrate the ability to detect and classify proud and buried UXO in the presence of natural and man-made clutter with actual structural acoustic sonar systems at-sea.

Technical Approach:

In the SA regime, acoustic wavelengths are comparable to the target dimensions, and sound readily penetrates the target and the sediment with the echoes directly related to the vibrational dynamics of the target. Aspect-frequency features can then be used to "fingerprint" the target without requiring a high resolution image. In this program, we will develop approaches allowing the sonar to capture echo data over various aspects and angular apertures to provide robust target echo spatial/spectral maps (acoustic color) and the associated classifying features. Based on the observed scattering and the operative SA mechanisms, we will explore various "finger prints" and how they should be extracted from the measured scattering patterns. We will develop practical experimental/numerical methods for training the relevance vector machine (RVM) identification algorithms and demonstrate the advanced classifying sonar technology in a marine environment. This requires that we develop and demonstrate advanced statistical classifier techniques that have the ability to mitigate adverse effects on the identification algorithms caused by target burial in an absorptive sediment, unknown vertical orientations, UXO target variations, and variability in the acoustic environment and clutter. We envision a SA sonar implemented on an underwater platform/vehicle utilizing broadband, low frequency, compact acoustic source and receiver technology. Scattering data would be post processed in a synthetic aperture fashion providing multi-static scattering data from small volumes of the sediment at various target aspects for submission to the SA feature-based identification algorithm. After demonstration of the sonar technology and associated SA identification algorithms, existing sonars, or ones designed according to the program findings and acquired by an industrial organization, could then be utilized in actual clean-up operations.

Results:

In this SERDP program (MR2103), we demonstrated the structural acoustic technology with an autonomous underwater vehicle (AUV) - based SA sonar successfully detecting UXO buried in

the sediment in the Gulf of Mexico and showing that their structural acoustic features could be used to separate them from proud and buried false targets. In particular, the Buried Object Scanning Sonar (BOSS) was set up to fly at several meters altitudes in 18.3 meter water depths off the Coast of Panama, City in the Gulf of Mexico. This AUV-based sonar carried out north-south, east-west, and diagonal paths over a target field comprised of nine explosive simulant-filled UXOs buried about 10cm below the sediment/water interface, two buried false targets, and 23 proud targets. The scattered acoustic pressure signals from the target field received at each of the 40 wing sensors as the vehicle moved in a straight line were processed in a synthetic aperture manner yielding both 3-D images and several acoustic color constructs for all the buried targets and for seven of the proud targets considered to be non-UXO. Most of the images gave useful information related to the target size and burial orientation. A multi-dimensional feature extracted from the acoustic color maps demonstrated almost perfect separation between the nine UXO and the nine false targets. These results demonstrate that typical buried UXO can be detected, imaged, and classified (UXO versus non-UXO) using a structural acoustic sonar and a relevance vector machine identification algorithm. In addition, earlier measurements made with a rail-based structural acoustic sonar in 25 foot waters off the Duck, NC coast validated the new concept of short time (specular) versus long time (elastic highlight) plan view imaging. Finally, the first accomplishment early in the program involved the sediment pool demonstration of a numerically trained classifier. Here we demonstrated good classifier performance training the relevance vector machine algorithm on a finite element target burial angle simulation data set and testing on UXO and false targets buried in the sediment pool.

Benefits:

The high resolution imaging sonar technologies available today can prosecute targets lying on the sediment surface; but their high acoustic frequencies prevent seeing UXO buried in the sediment. Several SERDP Projects (MR-1513, MR-2103, etc.) have been exploring structural acoustics (SA) based sonar for detection and classification of underwater UXO. The structural acoustic approach offers significant advantages over these more conventional acoustic approaches which rely only on the formation of high resolution images. These advantages include a diverse set of spatial and spectral structural acoustic “fingerprints” leading to high probability of detection, low false alarm rates and low frequency sediment penetration permitting buried target prosecution. Further, the SA approach allows the formation through SAS processing of complementary three dimensional images of the sediment volume and of any targets buried therein. Even though the SA frequencies are relatively low, these images have sufficient resolution to allow determination of the approximate target size, burial depth, and burial angle. The combination of this information together with target identification/classification through structural acoustic “fingerprints” provides the necessary information regarding the presence, location, and identification of underwater UXO for effective inspection at sites requiring remedial action. Further, the ability to use a high fidelity finite-element-based numerical model (addressing both the complex elastic target and the acoustic propagation environment) to generate simulated data for classifier training is extremely important given the many targets, burial conditions, and environments of interest.

OBJECTIVE

The objective of this program is to address the technical issues whose resolution would permit the realization of an efficient, high performance structural acoustic feature-based underwater sonar technology[1-6] that can detect and localize buried targets and separate the detections into UXO versus non-UXO without the need for high resolution imaging. This will be realized by employing a marine-based down looking measurement sonar to conduct a series of measurement exercises in suitable marine environments and combining these data bases with numerical models. The overall goals are to develop a physics-based understanding of the structural acoustics, to develop robust identification algorithms based on the structural acoustic features, and to demonstrate the ability of the structural acoustic technique to detect and classify underwater buried UXO in the presence of natural and man-made clutter. In the SA regime, acoustic wavelengths are comparable to the target dimensions, and sound readily penetrates the target and the sediment with the echoes directly related to the vibrational dynamics of the target. Aspect-frequency features can then be used to "fingerprint" the target without requiring a high resolution image. Our focus is on marine-based sonars that could look both downward (and sideways) in water depths ranging from several meters to hundreds of feet. The goal here is to develop a sonar approach which results in robust identification algorithms based on structural acoustic features and complementary 3-D SAS images and to demonstrate the ability to detect and classify proud and buried UXO in the presence of natural and man-made clutter with actual structural acoustic sonar systems at-sea.

BACKGROUND

Many active and former military installations have ordnance ranges/training areas with adjacent water environments in which unexploded ordnance (UXO) now exists due to wartime activities, dumping, and accidents. SERDP goals require the development of innovative technologies able to separate UXO from false targets and to discriminate amongst UXO targets themselves. The sonar configuration of interest in this program is the shorter range, down-looking system which uses mono-static and bi-static echo responses over relatively limited angular apertures[6]. Because the downward-directed acoustic energy intercepts the water-sediment interface at angles well above the critical angle, sound penetration into the sediment is not an issue for most bottom types. However, for deeply buried targets to (and from) which the sound must propagate through the sediment, sound absorption could be important, especially at the higher frequencies. The outstanding issues include the impact of sediment absorption, limited angular apertures, the strong backscattered echoes from the sediment surface or sub-layer structure, and out-of-plane target orientations on the structural acoustic frequency/angle features and the effectiveness of the related identification algorithms.

MATERIALS AND METHODS

In implementing the structural acoustic concept for the large angle look-down configuration, a towed body or an AUV is implemented with an acoustic source which directs broadband acoustic energy at the bottom over a wide angular aperture thus illuminating a large area of the sediment

surface and the volume below. A good example of the latter is the BOSS system.[7] The echoes scattered back toward the vehicle are detected by a receiver array either mounted on its side or bottom or attached to appendages extending from its sides. The received signals are SAS processed to recover the individual echoes returned from each of the many focal points throughout the illuminated sediment volume. This data base can then be processed to yield conventional 3-D acoustic images and scattering cross sections of the small UXO-sized volume elements making up the larger illuminated region. The conventional images provide information regarding buried target size, shape, and orientation whereas the return signal from each target-sized voxel can be presented to an identification algorithm previously trained on UXO structural acoustic features. The initial at-sea studies carried out in this program utilized a rail-based sonar which mimics some of the parameters of the BOSS system implemented on an AUV with wing receivers. Subsequent measurements were carried out using the actual AUV-based BOSS system.

RESULTS AND DISCUSSION

Numerical Simulation Data Base

Prior to carrying out exercises in an actual marine environment, our plans included carrying out a detailed buried target identification study using simulations from our STARS3D[8,9] numerical code augmented by our sediment pool laboratory data. These efforts focused on (1) establishing that the features we have been considering would be effective in classifying buried targets and (2) developing a viable approach for training the RVM[10] identification algorithms without the need for detailed measurements carried out beforehand in the actual marine environment. In particular, such a simulation-based approach would provide training data related to the range of target vertical burial angles one might encounter at an actual UXO contaminated site. Once completed, this approach with its pre-trained identification algorithms would be tested in the Duck, NC and Panama City, FL experiments. In support of this study, we carried out the generation of two target echo numerical data bases for a five inch rocket buried 10cm below the sediment surface for 91 individual vertical target burial angles each 2º apart ranging from 0º to 180º. The first data base contains the broadband target strength versus frequency over a 1 meter square array 0.20 meters above the sediment-water interface and the second the broadband target strength versus frequency over a 2 meter by 4 meter receiver array 0.5 meters above the sediment-water interface. (See Figure 1.) The former mimicked the sediment pool measurements with the associated 2D synthetic receiver array while the latter mimicked the measurements made at Duck using the partially synthetic rail-based line

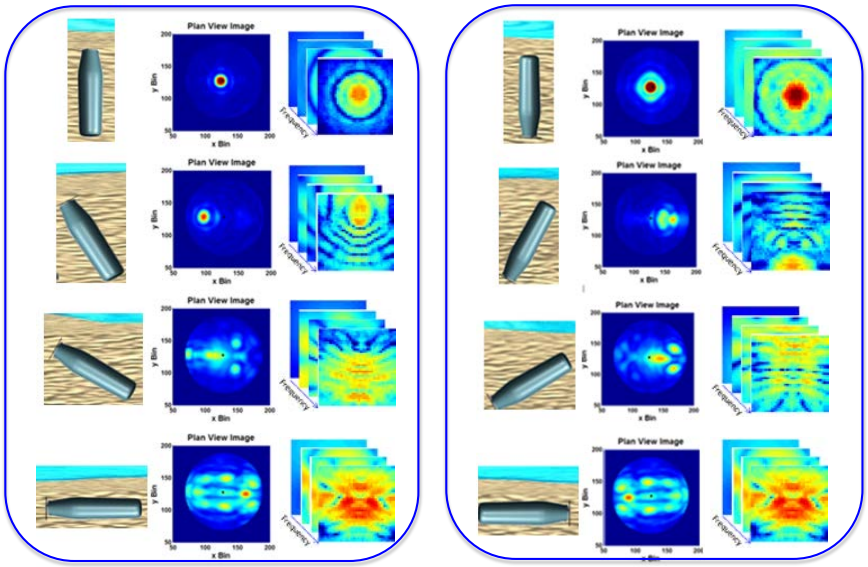

Figure 2. Numerical results showing the plan view image and the narrow band x,y target strengths for several example rocket burial angles.

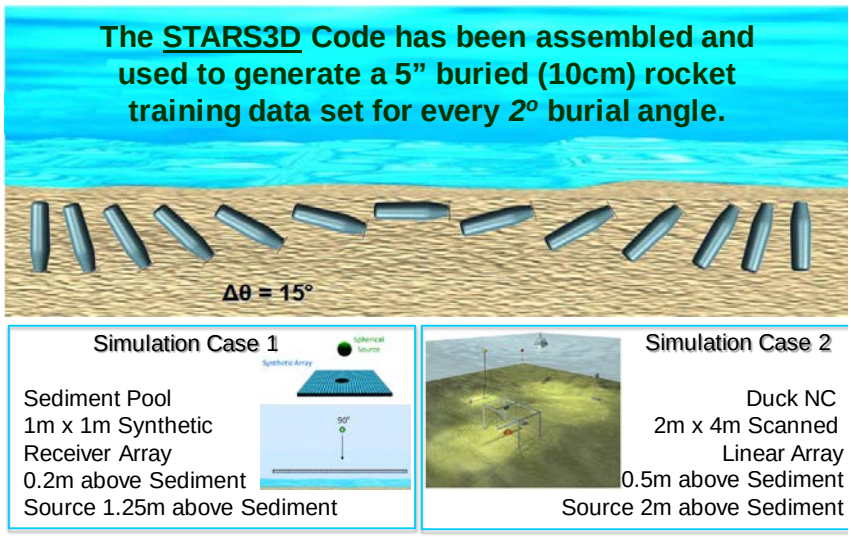

Figure 1. Details for the two numerical simulations carried out for a buried five inch rocket for 90 vertical burial angles. Case 1 and 2 mimic the sediment pool and Duck, NC configurations, respectively.

receiver array. The post-processing allowed the frequency-based STARS3D data to mimic the time-windowed measurements made in the sediment pool and at Duck. The numerical data bases (validated by the limited sediment pool data) were then used in the RVM identification algorithm training. We show in Fig. 2 the plan view images and single frequency target strength maps versus x and y for some example vertical burial angles obtained using the finite element numerical model for the five inch rocket. We point out the localized highlights observed in the plan view images for the horizontally buried rocket which will be discussed in more detail later in the report. These highlights are associated with the front and back air cavity resonances, the circumferential compressional wave in the shell wall, and the specular highlight.

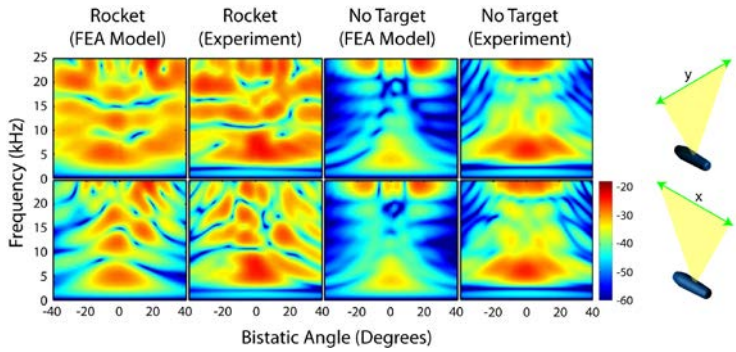

Figure 4. Acoustic color plots (along x and y) for the rocket and no target case for both measurements and simulations.

Sediment Pool Measurements

We also completed look-down measurements in the sediment pool facility using the system described in Fig.3. Here we use a single receiver hydrophone which is scanned over a one meter area as a function of x,y producing a synthetic square receiver array. The hydrophone is 20cm above the sediment-water interface. A broadband omnidirectional source is centered on the synthetic array and is 1.2 meters above the sediment surface. The source is excited with a narrow electrical impulse (shown later in the report) producing a broadband incident signal covering the band 2 kHz to 25 kHz. Eight targets were buried 10cm below the sediment surface one at a time and the scattered sound time signal was detected at each point of the synthetic array. As shown in Fig 3, the targets included three simulant filled five inch rockets at 0°, 30°, and 60°, two simulant filled 155mm shells buried at 0° and 30°, and three non-UXOs *viz.* a large rock, a cinder block, and a cinderblock rotated axially. By way of example, shown left to right in Fig. 4 are the x and y scan measurements of target strength versus frequency (acoustic color) for the five inch rocket simulation, the rocket measurement, the simulation for no target, and the measurement for no target. We make several points based on these results. First, the rocket measurement and simulation agree very well but not perfectly. Second, since the FEA "no target" case includes only the sediment/water interface, this interface must lead to some residual signal even after time windowing. Finally, comparing the two "no target" cases and recognizing that the facility sediment is very homogeneous leads to the conclusion that there must be an artificial layer created in the target seeding/burial process. Although not shown here, the quality of the above results are typical for the other targets as well.

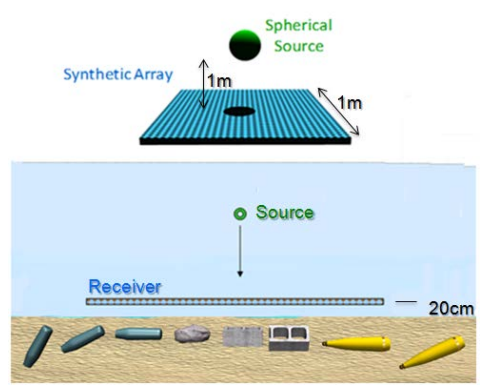

Figure 3. Sediment pool configuration and the eight buried targets.

Feature Separation

First, we used our numerical data base for the horizontally buried five inch rocket in the RVM training and tested our ability to separate it from three non-UXO targets buried in the sediment in the NRL pool facility. The three non-UXO targets included a large rock, a cinder block, and a second cinder block rolled 45 degrees. In addition, we included the no-target case, i.e. one in which the measured data over the 2D plane is due principally to scattering from the sediment-water interface. In the study, we considered the three feature spaces shown in Fig. 5 which we presented at the May 2011 In-Progress Review namely: (1) whole-body/linear x array, (2) whole-body/linear y array, and (3) whole-body/square array (see Fig. 5). In the first two, the x-array is along the rocket long axis and the y-array is perpendicular to the long axis. In the first two cases, we generated features based on integrating target strength over a number of sub-bands using a number of realizations of noise corrupted sediment pool data for training. We tested the resulting RVM identification algorithm on different realizations on noise corrupted sediment pool data and found good separation between the horizontally buried rocket and the other targets. The results for the y-array were somewhat better than those for the x-array. For case (3), we generated a band-limited correlation coefficient between the noise corrupted training data and the noise corrupted experimental data as a function of the lowest frequency of the band. We found that the targets separated fairly uniformly for all bands whereas the no-target case separated best when the band extended down to low frequencies. Further, for this case we used the simulation data base to determine the decrease in our ability to separate the buried targets as we decreased the size of the square receiver array. These results are shown in Fig. 6. Here the red lines are associated with the rocket buried horizontally and nose-down at 30°. We can see that for typical SNRs of 15dB, the hydrophone array can be reduced from $1m^2$ down to $3cm^2$ without losing much

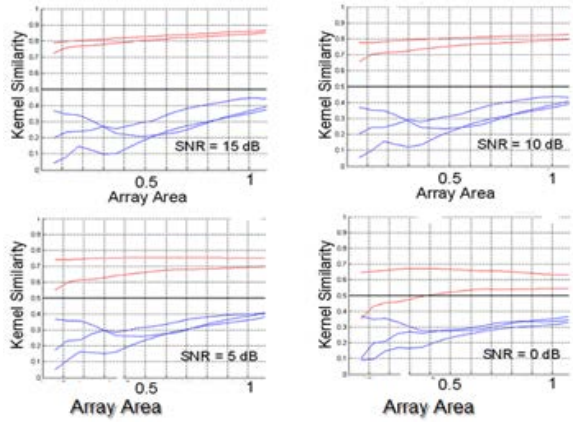

Figure 6. RVM feature separation performance based on numerical simulations vs receiver array area. Red lines are for the rocket UXO buried horizontally and nose down 30° and blue lines for the rock, cinderblock, and rolled cinderblock.

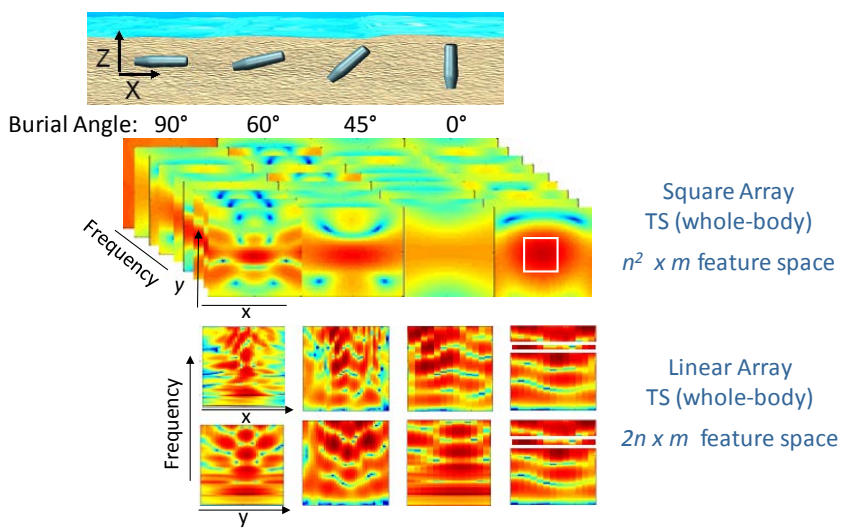

Figure 5. Multi-dimensional feature spaces we have identified for the RVM identification algorithm with examples shown from numerical simulation results for the rocket buried at various vertical angles.

performance regarding target feature separation. For our particular case here, this would correspond to a nine element receive array. We also see that the target feature separation performance stays fairly high down to an SNR of only 5dB.

Next we carried out a more detailed classification study using a simpler two dimensional feature space with just two features, *viz.* the plan view image *symmetry* and the target strength *correlation*[11]. These are defined in Fig. 7. These two simple features were employed to evaluate the degree of separation between the rocket UXO responses and those of the clutter. Perhaps the most salient features of the acoustic images distinct to the rocket UXO are the energy packets attributed to the circumferential compressional elastic wave components which we mentioned earlier in connection with the numerical simulations. It is noted that a certain degree of symmetry is inherent in the plan view images of the rocket, due to these effects. As such, we designed an algorithm to quantify the degree of symmetry in such images for use as the symmetry feature. This is accomplished as follows. Thresholds were applied to the plan-view acoustic images to remove low-level contributions attributed to volume scattering and array grating lobes. For the present study, a threshold is applied to reject image strengths less than 60% of the maximum value from each respective result. Images are then translated such that the

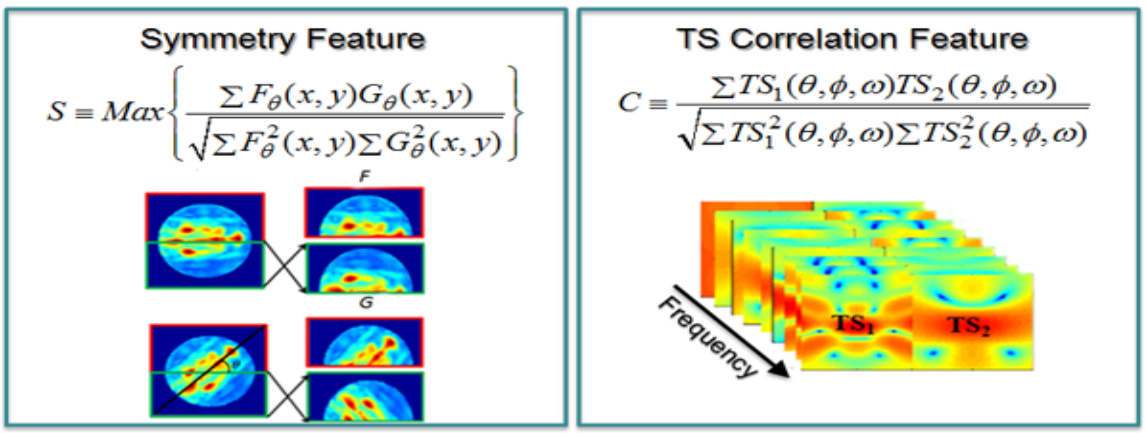

Figure 7. Definitions for the symmetry feature and for the target strength correlation feature. TS is the target strength and F and G are the upper and flipped lower half of the plan view images.

geometric center of the energy is located at the center of the image. The resulting image is then divided in two along the y=0 axis. The bottom image half is then mirrored in the vertical dimension. The normalized correlation between each image half is then computed. The original image is then rotated by some 'mirror' angle θ, and the process is repeated. The correlation is recorded over a full 360° range of rotation angles. The results demonstrate that plan-view images of the rocket UXO responses, from both experiment and simulation, possess a higher degree of symmetry than do the clutter objects and that such a feature may be employed to discriminate between the objects.

The second feature is derived from the target strength measurements and computations. We first note that the target strength results are typically displayed only over receiver aspects sweeping two orthogonal directions, along the beam and lengthwise target aspects. However, a projection algorithm[12] can be used to provide target strength information over a full hemisphere of receiving aperture. As such, the linear-scale magnitude of the band-limited frequency responses, over the full range of frequencies and receiver aspects, θ and φ, can be employed. The

normalized correlation is then computed between the response values predicted by the finite element simulation and each experimental result, and this is used as the second feature. We point out that the 'No Target' case, generated from experimental data, possesses a correlation value comparable to that of the clutter objects. In computing these correlation values, no threshold was employed, and it is likely that volume scattering and artifacts from the sediment interface reflection contribute significantly. We point out that our results here suggest the possibility of training an automated classification routine entirely with numerical data generated a-priori from time-harmonic finite-element computations, and we demonstrate this later.

The first tests using this two dimensional feature space involved discriminatively[13] training the RVM algorithm using the pool data on the horizontally buried five inch rocket and the three non-UXO targets shown in Fig. 8 (a large rock, and two differently oriented cinderblocks). The target strength correlation feature was constructed by correlating the measured target strength data with the numerical data for the horizontal rocket. The RVM testing results are shown in Fig. 8. As can be seen on the left of Fig. 8, in this two dimensional feature space, there is good separation between the three false targets and two different realizations of the horizontally buried UXO rocket (one being the case where the TS feature is obtained from the measured data correlated with the FEA result and the other the FEA result correlated with itself). On the right is shown the results when we create many more realizations (14) of each measurement by adding random noise (20 to 30 dB signal to noise) to produce the various realizations. As can be seen, as expected the separation has been reduced; however all non-UXO targets still separate from the two five inch rockets.

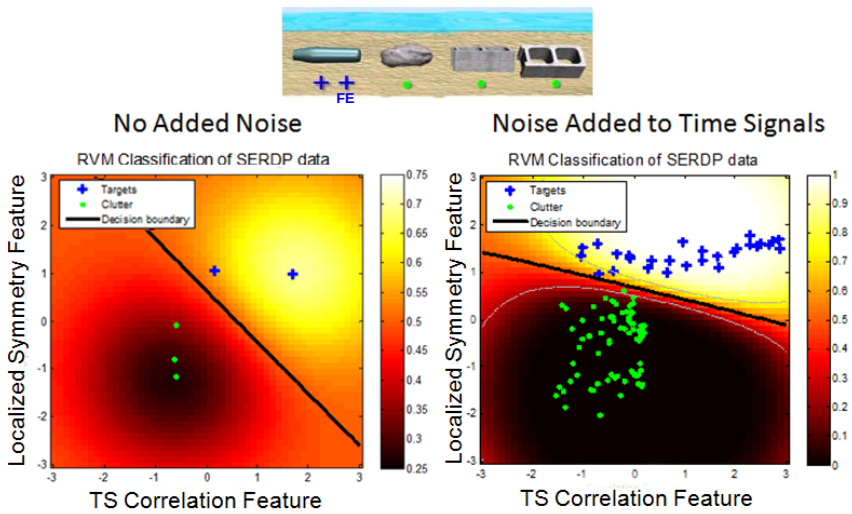

Figure 8. Target feature separation using a discriminatively trained RVM classification algorithm for the four buried targets shown above.

Next we trained using all 90 rocket burial angle cases taking the TS feature as the maximum correlation number, and these results are shown in Fig. 9. As can be seen, the separation between UXO and non-UXO is still good; however, the decision contour has been altered and now has some curvature. What impact this curvature may have in general upon the performance is not clear.

Next, we take a step forward and add several UXO targets to the training and testing data. As shown in Fig. 10, we now include measurements for three rockets buried nose down at 0°, 30°, and 60° and a horizontally buried 155mm shell. In the related test, we are considering the target of interest to be a five inch rocket at any of the three burial angles and the false targets to be the rock, two cinderblocks, and the 155mm shell. Again, the features are taken to be the maximum target strength correlation of pool data against rocket FEA data from 0° (nose up) to 180° (nose down) and the plan view image symmetry. As before, we generate a number of measured realizations by adding random noise to generate signals having from 20 dB to 30 dB S/N. The test results (shown in Fig 10) again demonstrate good target non-target separation and the decision boundary is deformed this time somewhat more drastically. As can be seen, there are only several targets that come even close to the boundary.

In the next study in this series, we take the four UXOs (the three five inch rockets at different burial angles *and* the 155mm shell) as the targets of interest. Again we generate a number of realizations by adding noise as described earlier. This case could be considered to be a preliminary test for a *class* based target ID algorithm. As can be seen, in the left side of Fig. 11, all the rocket targets separate from the three false targets. Most of the 155mm realizations (>90%) separate from them as well. Although the decision boundary is rather deformed, we believe that this result indicates that a class-based classifier using the 2-D features has promise. On the right side of Fig. 11 we show the effect of increasing the noise significantly so that S/N goes from 20 dB (Fig. 11 on left side) down to S/N of 0 dB . Although the decision boundary is quite deformed, the target separation is still good.

In the final study of this series, we take a major step forward by carrying out the training generatively[13] using *only* the numerically generated data. To mimic the measured echo data base

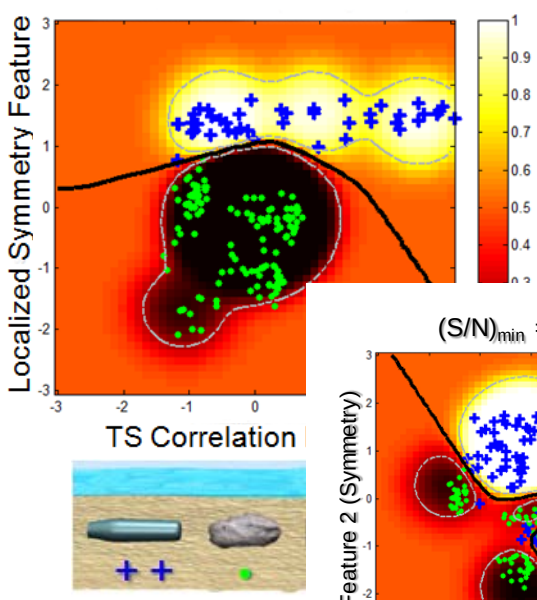

Figure 9. Target feature discriminatively trained algorithm for the four b below using all 90 burial ar

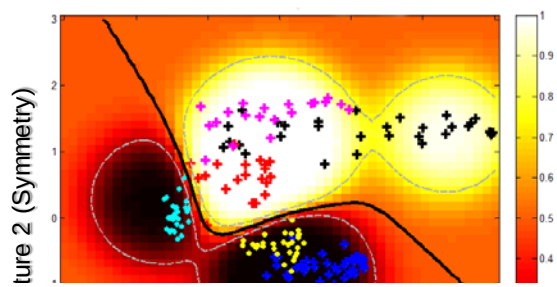

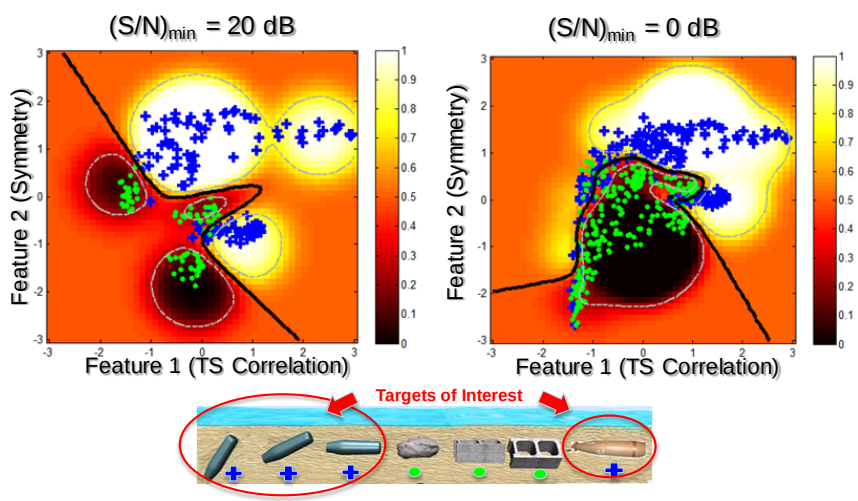

Figure 11 . Target feature separation using a discriminatively trained RVM classification algorithm for the seven buried targets shown below using all 90 burial angles in the training. Here the rockets and 155mm shell are the targets of interest.

as closely as possible, scattered time domain echoes were synthesized from the frequency-based numerical data so that the identical time gating, used to separate the target and sediment interface echoes, could be applied to both the experimental and numerical data bases. Each scattering data base is then used to generate target strength and localized image strength, σ, from which the two features are extracted. As in the previous discriminative cases, one feature is target strength correlation wherein the magnitude of the farfield TS associated with each angle (defined by the position of the receiver) is multiplied by the STARS3D simulated TS at that angle (the "template") and the resulting products summed over all angles in the aperture and over all frequencies in the band. Here the target strength, originally determined at a range defined by the position of the receiver array, is first propagated to the farfield using angular spectrum extrapolation. The second feature, as before, is the localized image symmetry obtained from the plan view localized image by first applying a threshold to reject image strengths less than 60% of the maximum, dividing the image into two about the geometric center, flipping one side, and computing the normalized correlation value as the sum over the images of the image products. This process is repeated $360/\Delta\theta$ times after rotating the image by angle $\Delta\theta$, and the maximum correlation coefficient in this set is selected as the symmetry feature. Both features are whitened such that the mean is zero and the variance is one.

A classification algorithm was constructed by training a relevance vector machine (RVM)[10] model using the image symmetry and farfield TS correlation features extracted from the numerically generated data for the 90 rocket burial angles. A number of scattering realizations (9) were created by adding various amounts of random noise (giving a range of S/N from 20 dB to 40 dB in steps of 2.5 dB) to all the simulated scattered time-domain echoes and carrying out 15 "trials" for each S/N. (Here S/N is defined as the peak level in the time echo over the rms noise integrated over the band.) The training was carried out generatively i.e. using only labeled target (i.e. rocket) data.[14] The symmetry features were obtained from the appropriately processed noise corrupted signals whereas the TS correlation features were obtained from the processed noise corrupted signals and the uncorrupted signals for the template. This process produced 12,150 values for each feature. A Gaussian radial basis function (of the Euclidean distance between points in feature space) with a standard deviation of 0.5 was chosen for the RVM kernel. The resulting RVM classifier is shown in Fig. 12. The color map presents the probability that a particular detected signal having the associated 2D feature is from a buried rocket. Here, three decision boundaries are indicated: 0.5 probability (black) and 0.8 and 0.2 probabilities (dashed gray).

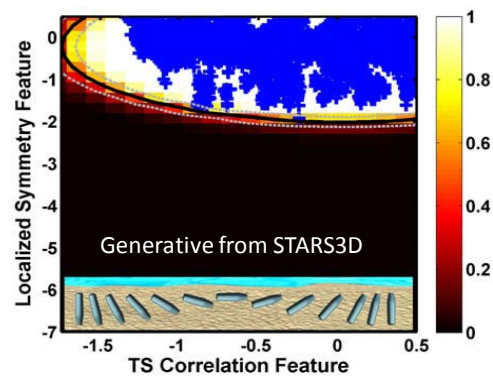

Figure 12. Generatively trained RVM algorithm using only the simulated rocket data for 90 burial angles.

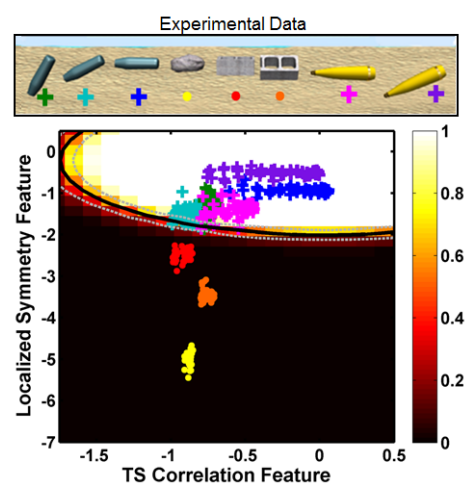

Figure 13. Buried target ID in the sediment pool using the numerically trained RVM classifier shown in Fig. 12.

The classifier trained as described above was tested on the sediment pool data in the following manner[14]. The measured time signals for each of the six buried targets were corrupted by adding various amounts of random noise (giving a range of S/N from 20 dB to 40 dB in steps of 1 dB). Five different realizations were obtained for each S/N resulting in 105 different echoes at each of the 1225 receiver locations for each of the six targets. In a sense, this expands the target test sample to a virtual 630-target set. These signals were processed to yield the farfield target strength and the localized image strength from which the TS correlation and image symmetry features were determined. Target calls are then automatically made based upon where these features fall with respect to the decision boundaries shown in Fig 12. The testing results are shown in Fig. 13. Although difficult to discern, for a 0.5 decision boundary, all of the rocket data points (regardless of burial angle) fall within the threshold for identifying it as a rocket. As for the false positives, about 30% of the false targets would be incorrectly labeled as a target, and these would all be associated with the cinderblock buried flat in the sediment. For this "perfectly" placed orientation, the symmetry feature is artificially high.

This and the more general performance of the classifier would be summarized by its ROC curve which is not shown here because it appears as a perfect "L-shaped" figure nearly indistinguishable from the vertical and horizontal axes themselves. The right-angle knee of the curve indicates an exceptionally high degree of performance for this classifier, at least for the small set of targets in this study. For example, a very high resolution map of the upper left corner of the ROC curve shows that for a decision threshold boundary near 0.99, the ROC curve indicates a probability of false alarm of < 1% and a probability of detection of > 99%.

These results, although statistically limited, support the following conclusions: (1) The localized image symmetry and target strength correlation 2D feature space described here appears to be an effective discriminator for separating UXO targets like the rocket from at least some non-UXO targets; and (2) generative RVM identification algorithm training can be carried out using a high fidelity structural acoustics numerical code. If further statistically significant target data supports this latter conclusion, then the fact that the training can be carried out using a numerical code has an important practical implication: future UXO sonar systems would be able to train for a variety of targets, burial angles, sediments, and acoustic conditions without the need for time-consuming, expensive scattering measurements.

Figure 16. Rail look-down measurement system

Measurements at Duck, NC

Rail-based measurements were carried out during the period May 14, 2012 through June 4, 2012 off the coast of Duck, NC using the Army Corps of Engineers Field Research Facility (FRF). (See Figs 14 and 15.) The measurements focused on the collection of bistatic (pseudo-monostatic) SAS measurements for large look-down angles on UXO's buried in the bottom next to the pier in a flat, sandy region where the water depth is between 25 and 30 feet. The buried UXO measurements employed a rail-based source/receiver system (Fig. 16) designed and constructed for this program. It was placed on the bottom nominally 30 m from the end of the pier and operated from the operations shack near the pier's end. Due to the arrival of two tropical storms in the area during this period, it was not possible to collect data from many of the

Figure 14. Pier at Duck, North Carolina

Figure 15. ACE Field Research Facility

Figure 17. The five inch rocket UXO

target scenarios originally planned even though the time on station was extended by a factor of two. As a result, data was collected on only a small subset of the originally planned target set.

The completed set of measurements included scattering from the five-inch rocket (Fig. 17) buried horizontally 10cm (nominally) below the sediment surface and the same target buried with the nose oriented 30 degrees below the horizontal. A third run was carried out with no UXO present so as to include only scattering from the sediment/water interface and from any naturally occurring scatterers in the sediment.

Divers were used to bury the targets. The burial process, known to be problematic even in a pool-based facility, involved the use of shovels and hands and a dig/roll procedure. The plan was to bury the UXO targets at a particular vertical burial angle in such a way that the shallowest point of the target was 10cm below the sediment-water interface and the long axis of the target was aligned with the axis of the real receiver array. Difficulties which arose with the original divers forced us to conscript a new diver team. This situation together with the consequences of dealing with the two tropical storms led to the actual target burial depth and in-plane orientation being different from that planned. Although we do not know for certain, the burial depth may have been shallower than the 10 cm goal, and the in-plane target orientation was 90° to that originally planned.

The data was processed during the period 7/1/12 and 9/30/12 followed by data analysis. For each of the above three cases (two buried rocket orientations and one no-target case), the measured time signals included the response of the SQ-26 hydrophones at each of the 4256 receiver positions. For the buried target cases, each of these time signals in principle contains (1) a replica of the incident acoustic signal as it passes a hydrophone on its way to the sediment interface, (2) any energy scattered back by the water/sediment interface, (3) the echo from the buried UXO target, (4) scattering from any inhomogeneous structure that might be present in the sediment, and (5) background ambient noise. The no-target case should include all but (3) above.

After completion of the data collection for the three cases, it was discovered that the measured data quality had been compromised because of a crack which apparently had developed in the acoustic source during the exercises. It was concluded that as a result, all the acoustic scattering data had been collected using a source signal considerably elongated in time instead of with an incident acoustic pulse having a uni-polar, narrow impulsive time history as has been the case in all our previous measurements[2-6]. This in turn impacted our ability to separate the buried target echoes both from the direct source signal and especially from the sediment interface echo which begins almost simultaneously with the target echo. Notwithstanding, we continued with the data processing and were able to extract lower quality target strength spatial maps and moderate quality 3-D images of the buried targets.

Our analysis of the limited data base collected led to the following results. (1) The Duck marine sediment produces volume scattering above that from the more homogeneous pool facility sediments. While the associated signal is only 5 dB below the target echo level, processing gain resulting from a narrower time signal would decrease this significantly. Notwithstanding, it should be taken into account in future simulations. (2) The image symmetry successfully exploited in the sediment pool work did not yield an effective classifying feature in the Duck case. However, we believe this is mainly a result of the poor image quality due to the malfunctioning source, and we hope to validate this conclusion by further simulation analysis. (3) A new feature was introduced, viz., the image correlation feature. Based on the limited data obtained in the exercise, this feature appears to have merit, and it may have impact especially regarding the non-horizontal burial angles. (4) The background acoustic noise level as monitored by our array hydrophones in the Duck environment is nominally about 10 dB below the buried target signal levels. This is encouraging in that in our previous simulations and successful RVM tests using the sediment pool facility measured data, we had intentionally added about this much random noise to the pristine, low noise time signals.

Duck Exercise Details

TABLE 1 – Measurement Exercise Timeline

Date	Operation	Comments
5/14	System Deployments	Stopped Ops due to weather
5/15-18	Slow Deployment	Deployment very slow/Diver not up to

		task
5/19-22	Stand Down for Hurricane Alberto	
5/23-24	Recovering Equipment after Hurricane Passed	
5/24	Deploy SERDP Rail	
5/25-28	Stand Down for Hurricane Beryl	
5/29	New Divers Hook Up Equipment Start SERDP Noise Measurements	New Commercial Diver
5/30	Finish Equipment Deployment SERDP No Target	
5/31	SERDP Measurements Rocket	
6/1	SERDP Measurements Rocket	
6/2-3	Stand Down for Weekend	
6/4-5	Recover Equipment	

The May-June 2012 rail-based measurements at Duck, NC were carried out by the coordinated effort of five teams: (1) The NRL- Physical Acoustics Branch At-Sea Measurement Group headed by Dr. Harry H. Simpson including Dr. Alain Berdoz, Mr. Dan Amon, Ms. Kyrie Jig, and Mr. Steve Liskey; (2) USACE-CEERD-HC-F Field Research Facility personnel including Mr. Mark Preisser, Mr. Brian Scarborough, Dr. Jesse McNinch, Ms. Judy Roughton, and Mr. Kent Hathaway; (3) Outer Banks Dive Center personnel including Mr. Bill McDemant; (4) Chesapeake Bay Diving, Inc.; and (5) NSWC-PCD including Mr. Gary Wommack (Mammal Watch/Safety Observer). The measurements originally planned for the period May 14, 2012 through May 25, 2012 had to be suspended and then extended twice due to the storms, first from May 29, 2012 through June 1, 2012 and then for a second time from June 3, 2012 through June 4, 2012. The actual measurement exercise time line is shown in TABLE 1.

The measurement rail system (Fig. 18) consists of a 2m wide by 2m high by 4m long aluminum frame structure. A 32-element array of equally spaced SQ-32 hydrophones was moved along the rail in 3cm steps at a height above the sediment of 0.5m. An omni-directional source was fixed to the array mounting 1. 5m above it and 0.5m in front of it. The receiver array and source moved rigidly together. The rail-based sonar system was deployed using the CRAB (Coastal Amphibious Research Buggy) as shown in Fig. 19. The rail system was placed on the bottom nominally 30 m from the end of the pier in 25-30 feet of water, and the sonar system was operated from the operations shack near the pier's end.

Receiver Time Waveforms- Duck versus Sediment Pool facility

Based on the time structure observed in the hydrophone responses, we concluded that the only both *clearly* observable and *directly* identifiable signal components are those associated with components (1) and (2) as listed on page 5, i.e., the incident acoustic signal and the signal scattered from the sediment-water interface. As we show later, this is not to say that target echoes cannot be extracted from the receiver signals but that they are not *directly* identifiable. This is not the case with the measured results made earlier in the sediment pool facility where signals from both (2) and (3), i.e., the sediment-water interface and target signals, are not only clearly evident but easily separable and exploitable for classification[11].

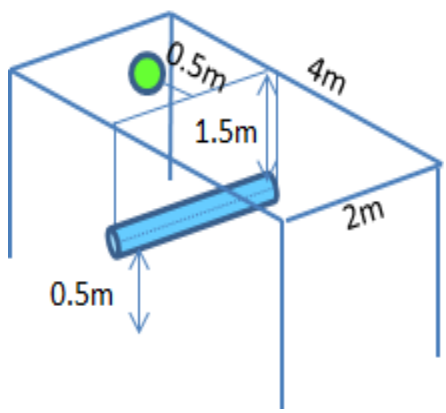

Figure 18. Rail-based measurement system dimensions

Figure coastal

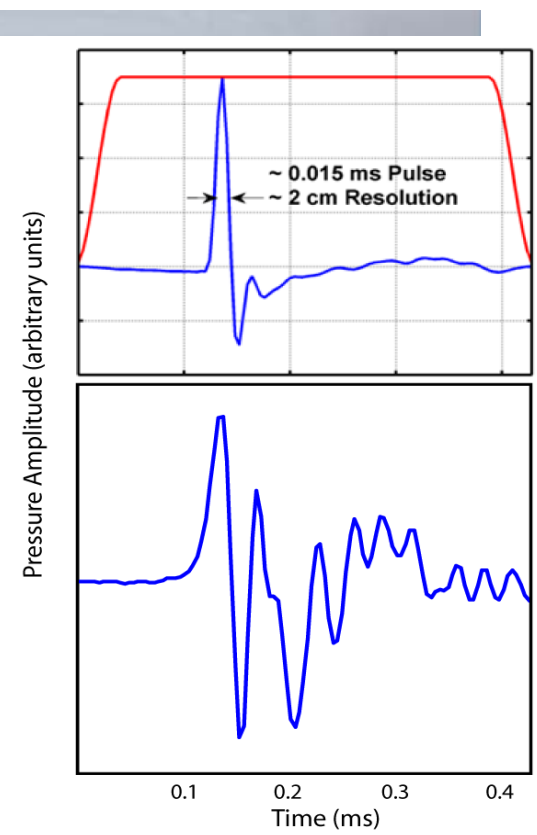

Figure 20. Acoustic source time profile (upper-sediment pool and lower-Duck).

There are a number of differences between the parameters of the sediment pool and Duck measurements. They are: (1) The hydrophone distance above the sediment interface is 0.5m for the Duck measurements and 0.2m for the sediment pool. (2) In the sediment pool measurements[11], a single hydrophone held by a slender robotic arm is scanned over the 2-dimensional receiver plane. A 32-element receiver linear array with the source mounted forward and above it is scanned in 3cm increments in the Duck exercise yielding small angle pseudo

mono-static responses versus the true bi-static data from the pool. The array is mounted and moved while attached to a large structure made of aluminum. (3) The targets are buried precisely at 10cm depths in the sediment pool facility. Thus there is a guaranteed minimum of 0.1 msec time separation between the interface and target returns. At Duck, however, the divers had much less control during the burial process. As a result, we believe the resulting, effective burial depth could be less than 10cm. (4) The resulting smaller time differential would make it much more difficult to separate the interface and target echoes. (5) Although designed to be a narrow impulse in time, there was much more temporal structure in the Duck incident acoustic pulse as monitored by the hydrophones than there was for the sediment pool source. As a result, while the sediment pool pulse is basically flat over the band of interest, there is considerable "resonant" structure in the Duck source spectrum as shown in Fig.20. Here, the time waveforms for the sediment pool and Duck exercises are compared. The red time window function indicated in the upper figure is that which is used for processing the pool source waveform to obtain the source spectrum. Clearly a longer time window is required for the Duck case since source energy appears to be present at longer times than for the pool source. More importantly, the elongated time structure in effect adds similar elongated time structure to all the echoes discussed above making it even more difficult to separate the target echo in time from the direct and interface signals and to definitively identify the target echo. Subsequent evaluation of the source itself showed that a crack in the piezo-ceramic was the cause of its anomalous time response. Having discovered this problem toward the end of the exercise, attempts were made to carry out additional measurements with a different source. However, during these attempts, additional problems involving the electrical cables were identified precluding the taking of new measurements in the short time remaining. (6) We can expect more background noise at Duck than there is in the sediment pool facility. (7) The real Duck marine sediment is expected to be less homogeneous than the more pristine laboratory sediment.

Numerical Simulation Results

An intensive numerical study had been carried out prior to the exercises simulating the Duck measurements with the Duck configuration parameters using the NRL STARS3D finite element-based code[8,9]. Results of this simulation for the five inch rocket buried horizontally are shown in Fig. 8a where in the upper map the amplitude of the received pressure signal is plotted while the pressure in decibels is plotted in the lower map. The 350 receiver positions indicated in these figures (the abscissa) are roughly centered on a patch just above the buried target location. This snippet begins at one end of the line receiver array, and as one goes from say 1050 to 1082 from the first to last of the 32 receivers, the real receiver array is fixed in space. The array is then moved 6cm, and the process is repeated to generate the display shown in Fig. 21a. Shown in Fig 21b are the same plots after all the returns from the source have been time aligned i.e. focused back to the source. This representation is useful when one wishes to reference various returns to the actual source level. Later, when forming target images, the data will be time-aligned (focused) with respect to the scattering target.

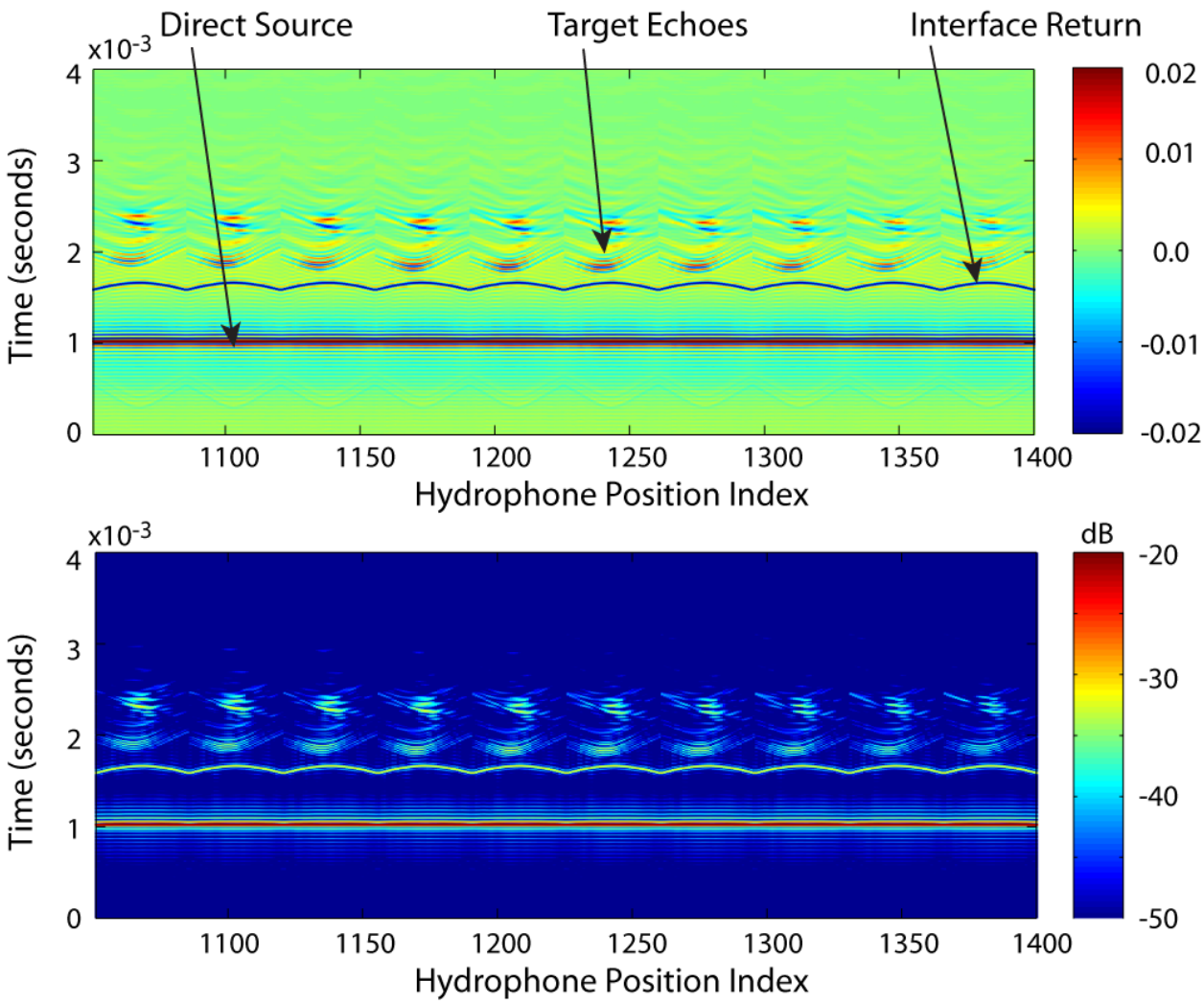

Figure 21. Numerical results for Duck simulation after time-alignment (target response increased by 10x)

These results were subsequently used to help develop an understanding of the impact the differences between the two configurations had on the Duck experimental results. One important finding relates to the sediment interface and target echo levels relative to the direct acoustic signal passing the hydrophones for the two scenarios. (See Fig. 21.) For the sediment pool facility measurements, these ratios are -6 dB and -13 dB, respectively. For the Duck measurements, the ratios are -10 dB and -20 dB as can be seen in Fig. 21. This presents the following issues for the Duck measurement scenario. First, that the target echo at the receiver is 10 dB lower than the sediment interface echo at Duck puts an increased demand on the processing required to separate the sediment interface and target echoes. Second, the divers at Duck had difficulty in burying the targets at the specified depth of 10cm. The actual burial results are only known approximately, but we have reason to believe that the final burial configuration was between the 10cm goal and a flush-burial condition with the sediment interface in the vicinity of the target possibly somewhat depressed and slanted. With even less time delay between the target and sediment interface echoes, our standard time-gating procedure

for echo separation is much less effective. Third, the Duck measurements exhibit an additional diffuse background from sediment volume scattering elements. Fourth, these effects together with the increased background noise did not allow clear identification of the elastic target echo even at times well beyond the arrival of the specular interface return. In this regard, the measured long time background signals at Duck (times for which in the pool measurements the target echoes were clearly observed) were found to be about 10 dB higher than in the Duck simulation results which assumed the usual narrow time impulse for the incident acoustic source signal and no additional background noise.

Processed Duck Data

Shown in Fig. 22 are the measured responses versus time as measured by a subset of the synthetic array. The 156 sampled positions shown in this figure are roughly centered on a patch just above the buried target location. As we go along the abscissa from say 1860 to 1892, the real hydrophone array is fixed in space. This particular data snippet begins at the hydrophone position at the beginning of the real array. After indexing to the end of the fixed array, the real array is then translated along the track a distance of 3cm, and the process is repeated to generate the display in Fig. 22. (Note that in the simulation, the real array was translated along the track in increments of 6cm resulting in the different indices for simulation and measurements.) In the data presented in Fig. 22, all the signals have been time-aligned to coincide with the arrival of the point source. Without this alignment, the direct source signal versus hydrophone position index would have the same scallop appearance as that in the simulation (Fig. 21a).

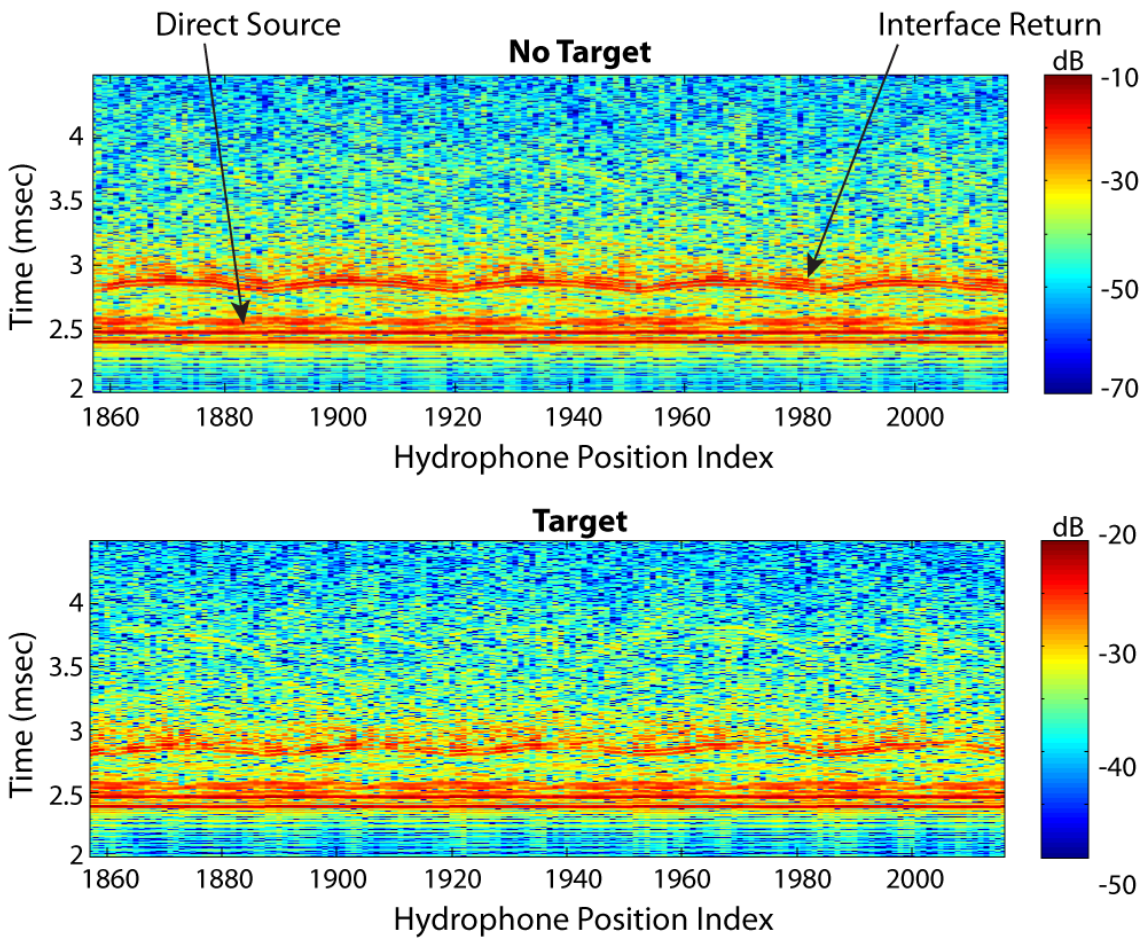

Figure 22. Measured signals at the receivers (horizontal target)

Examination of the numerical simulation results predicts that the target echo level is expected to be about 10 dB less than that from the sediment interface. Translating this scale factor to the Duck measurement results would predict that the target echo signals should be comparable to the levels which are actually observed in the "no target" case at times beyond those for the interface echo. Thus we conclude that at a minimum, data processing beyond simple time gating will be required to extract the target echo which would be immersed in comparable levels of spatially and temporally distributed signals from a variety of sources. These longer time competing responses seen in the no target case could be due to the following three effects: (1) scattering from inhomogeneous structure present in the natural Duck sediment; (2) ambient noise related to the marine environment; and (3) the unintended long time history of the acoustic source signal which among other things would spread the stronger interface echo out over a much longer time interval.

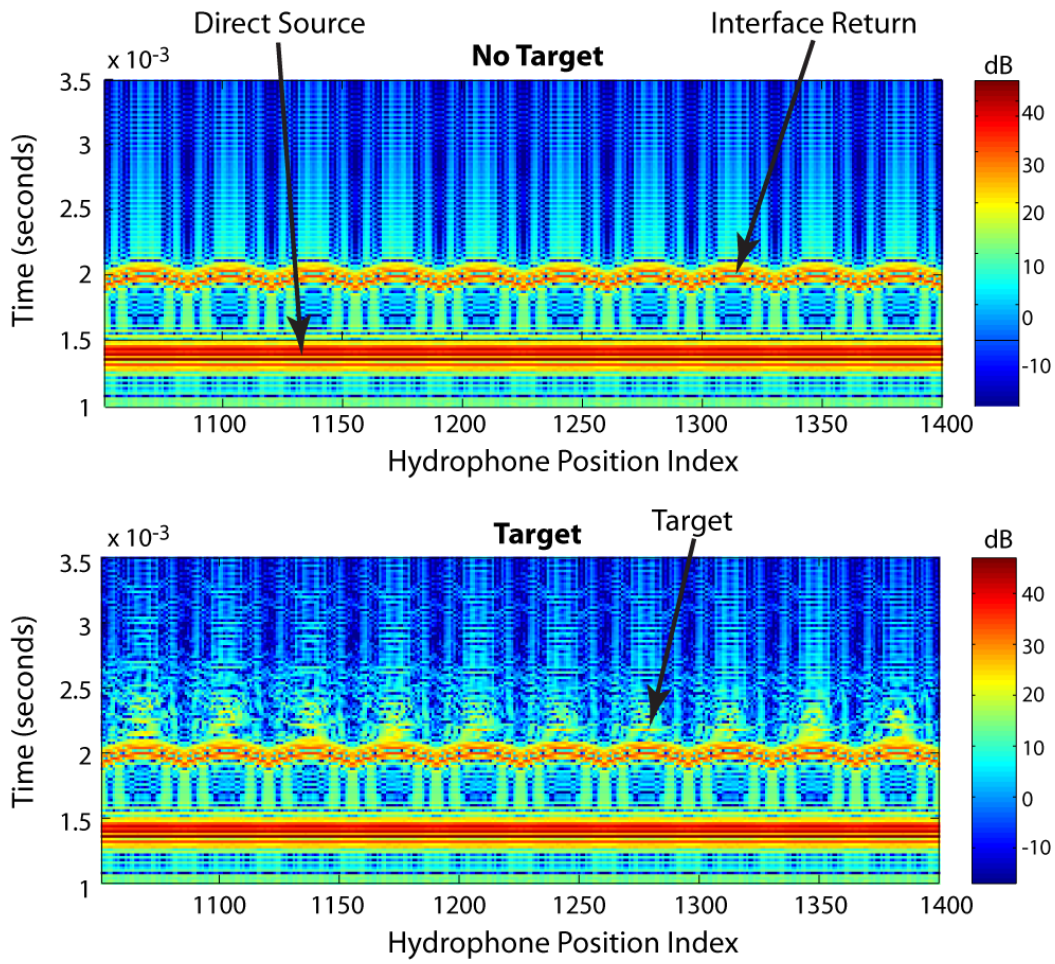

Figure 23. Duck Simulation with Source Convolution.

We believe that the major contributors to the large levels of spatially varying background signals (i.e. the significant components at times beyond the initial interface return) are associated with two of these effects: the unintended long time history of the acoustic source signal which acts to spread the larger interface echo out over a much longer time interval and scattering from the marine sediment volume. In order to examine the first, we carried out the simulations shown in Fig. 21 for the no-target case but this time convolving the responses with the known time history of the incident source signal (see Fig. 20). These results are shown in the upper part of Fig 23 where again we have time-aligned the signals so that the direct arrival from the source to each receiver arrives at the same time for all receivers. As can be seen, moderate signals exist far beyond the time for the initial interface return, and their levels can be seen to be as much as -14 dB compared to that for the interface echo. Comparison to the corresponding components in Fig. 21b shows them to be about the same level below the strong interface response. In Fig. 23, the features appear to be much more coherent than those in the measurement (Fig. 22), and this may be a consequence of the fluctuating ocean environment. We do not believe these fluctuations are due to environmental noise adding to the acoustic signals since hydrophone measurements made with the acoustic source turned off yielded RMS noise levels down about 30 dB from the direct source levels shown in Fig. 23.

We also believe that some of the diffuse background levels are due to volume reverberation from inhomogeneous structures in the sediment such as shells, trapped air, or a mixture of pockets of silt and mud. If we consider the longer times in Fig. 23 (say beyond 4ms), we might conclude from Fig. 23 that at these long times the effects due to the elongated source pulse spreading the interface return in time are minimal and that what is now dominant in the measurement (Fig. 22) is the diffuse scattering from the inhomogeneous sediment structures. Assuming that there is no volume reverberation in the water, the levels of reverberation from the scatterers in the sediment would be approximately proportional to the product of the acoustic travel distance during the extraction time window and the area of a spherical cap (actually an elliptical cap if the source/receiver are not co-located) formed by the sediment interface and all possible acoustic paths to the center of the TS extraction time window. The area of the cap is proportional to $(d+h)d$, where d is the depth below the sediment interface and h the source/receiver height, so that the volume reverberation increases roughly as the square of the depth d of the volume scatterers. Thus this effect can be significant at longer times i.e., from sediment structure present at the deeper depths. Considering Figs. 21 -23 and the measured ambient noise levels, we can conclude that on average, these sediment background scattered signals are about 5 dB lower than the UXO target echoes. The various component signal levels for both the Duck measurements and simulations are listed in TABLE 2.

TABLE 2 – Signal Levels for Measurements and Simulations

	Signal Level (dB) Duck Measurement	Referenced to Direct Source	Signal Level (dB) Duck Simulation	Referenced to Direct Source
Direct Source	-10	0	-20	0
Interface	-20	-10	-30	-10
Target	-30	-20	-40	-20
Diffuse Long Time	-35	-25	-∞	-∞
Noise	-40	-30	-∞	-∞

The diffuse long-time scattering components which we believe are associated with inhomogeneous structures present in the marine sediment (probably there in part due to the skirts of the just passing hurricanes) are in fact absent in the measurements made in the sediment pool facility. This is of course to be expected since the sediment installed in the sediment pool facility is known to be very homogeneous and has been characterized to be such many times[15,16]. For comparison purposes, we show in Fig. 24 the corresponding time-receiver position displays for measurements of the buried rocket made in the sediment pool facility. As can be seen, the long–time background level is quite low in contrast to that seen in the Duck measurements displayed in Fig. 22. In fact, in the sediment pool these levels are at least 25 dB below the interface echo level while only down 15 dB in the Duck sediment.

It is important to note that the -5 dB estimate refers to the relative levels of target echo and reverberant sediment volume scattering *as observed in the Duck measurement exercise*. In particular, with a properly functioning source, this relative level would be considerably lower owing to the effective processing gain that would be achieved since the target echo would be more localized in time compared to the sediment volume scattering. A crude estimate of this processing gain obtained from comparing the two waveforms shown in Fig. 20 for the properly functioning source versus the Duck source gives about 14 dB. In this case, the rocket target echo would be almost 20 dB higher than the reverberant background. Further, considering the monostatic target responses reported in Ref. 17 for a range of UXO sizes from the somewhat larger 155mm shell down to the much smaller 25mm cartridge, we speculate that the scattering levels for the smallest target would be about 10 dB down from that seen for the rocket in the current measurements. This suggests that detection and classification would be achievable for smaller targets in sediments similar to that at Duck. Of course, establishing the achievable classification performance versus target size must await more experimental results.

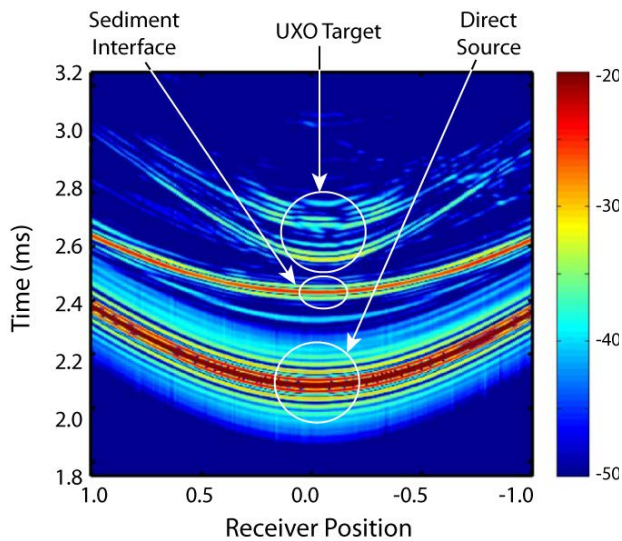

Figure 24. Measured signals at the synthetic array receivers in the sediment pool facility.

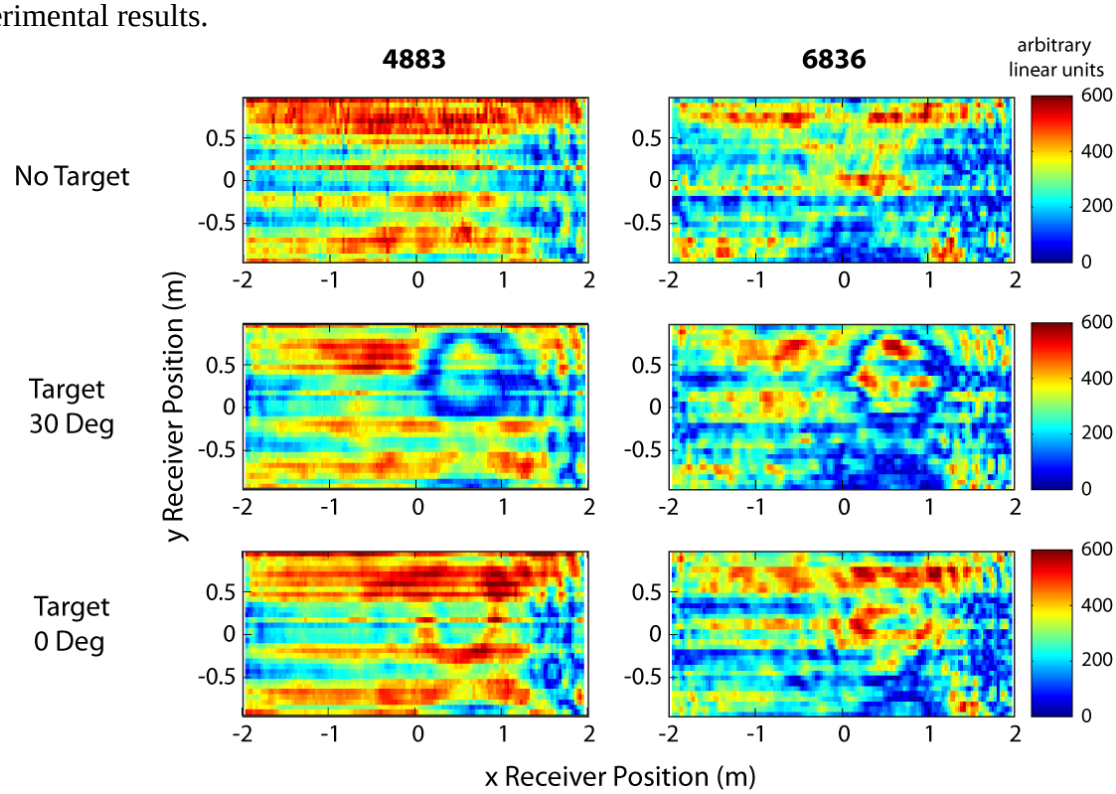

Figure 25. Preliminary processed data to extract target scattering levels.

Examination of Fig. 23 helps explain the difficulty in directly observing the target echoes immediately following the much stronger interface response in the Duck measurements with malfunctioning of the acoustic source. At those times, the levels associated with the direct source signal due to the elongated source time waveform are on the order of -10 to -20 dB with respect to the interface echo. Yet as can be seen in the simulations shown in Fig 21 and as summarized in TABLE 1, the target echo is expected to be at least 10 dB lower than the interface echo implying that the *long time* source signal and target echo signals are roughly the same level. This would make it difficult to clearly identify the target echo since we are looking for a target echo level which is comparable to the peak levels of the direct source signals at the longer times.

The following straightforward processing procedure was utilized to extract the target scattering spatial patterns from the receiver data shown in Fig. 22. The time signals from each receiver were time-aligned so that the direct arrival from the source to each receiver arrives at the same time for all receivers. (The actual spatial point for time alignment is arbitrary when generating frequency domain plots as is done below.) Next, the time-domain signals were windowed attempting to keep mainly the surface reflection and the target response. Unlike our work in the sediment pool, we were forced to keep both these signals in the processing stream. A Fourier transform was then applied to the windowed signals transforming them to the frequency domain. The resulting spatial scattering patterns are shown for two example frequencies in Fig. 25 where the color map is displayed in arbitrary units. Comparisons of the target/no-target cases for both burial angles clearly indicate the presence of target related scattering. Why the spatial structure present in the actual patterns for the target case appears as it does is not clear and may be in part a consequence of the elongated source time waveform and the resulting overlapping direct residual and interface signals.

We note that the scattering parameters displayed in Fig. 25 are proportional to the near field target strength which is defined in the usual manner as[17]:

$$\begin{aligned} &\text{Target Strength at } \vec{r}_n = 10\log\left|X_n(\omega)\right|^2 \\ &X_n(\omega) = D_n(\omega)\left|\vec{r}_n - \vec{r}_c\right| \end{aligned} \tag{1}$$

where r_n and r_c locate the nth receiver and target center, respectively, ω is the angular frequency, and $D_n(\omega)$ is the measured scattered pressure over the incident pressure.

Next, our standard imaging algorithm[11] was applied to the windowed data in order to obtain from the scattered echoes three dimensional images of the target. This process produces the localized image strength, σ, defined as[11]:

$$\text{Image Strength at } \vec{r}_i \equiv \sigma_i(\vec{r}_i) = \frac{1}{N}\sum_{n=1}^{N} 4\pi\left|\vec{r}_n - \vec{r}_i\right| d_n\left(\vec{r}_n \middle| \vec{r}_i, \frac{\left|\vec{r}_n - \vec{r}_i\right|}{c}\right) \tag{2}$$

Here r_i locates the scattering or image point, d_n is the inverse Fourier transform of $D_n(\omega)$, and C is the sound speed (here taken to be the same for the water and the sediment for simplicity). The resulting images for the horizontal burial case for the plan view (x,y) plane are shown in Fig.26.

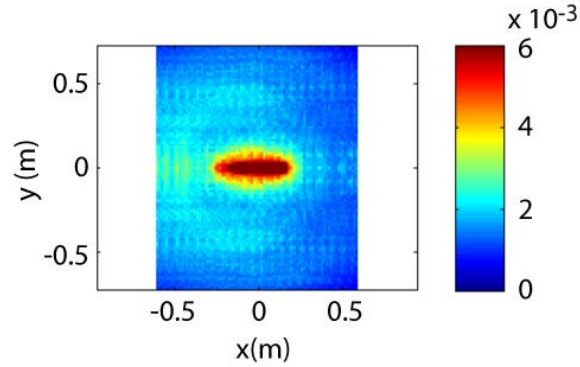

Figure 27. Plan view image without time gate filtering of the initial specular return.

Before commenting on these images, we point out the saliant differences among the Duck experiment, Duck simulation, and sediment pool measurement configurations. First, although unintended, the buried targets were oriented 90 degrees with respect to one another in the Duck experiment and Duck simulation as depicted on the right in Fig. 26. The upper two drawings related to Duck depict the 2m wide and 4m long rectangular scan area, the 2m line receiver array, the acoustic source (in purple), and the buried five inch rocket. The arrows depict the direction of motion of the receiver array and attached source. The lower drawing related to the sediment pool depicts the 1m square scan area, the center-placed stationary acoustic source, and the buried target. The arrows here indicate the two dimensional receiver scan. The effects of this difference are somewhat magnified by the fact that the source is mounted one meter out ahead of the horizontal receiver array. Second, the sediment pool system has the source right above the center of the target and at the center of the 2-D synthetic receiver array. Third, the sediment pool array is 0.2m above the sediment interface while this distance is 0.5m in the Duck geometry. Finally, the sediment pool measurement is a true *bi-static* measurement in which the source remains fixed above the target center and the receivers are generated synthetically over a symetric square patch[11]. The Duck measurements and simulations are small angle pseudo *mono-static* in nature with a moving source fixed at a small angle with respect to the real linear array which moves with the source.

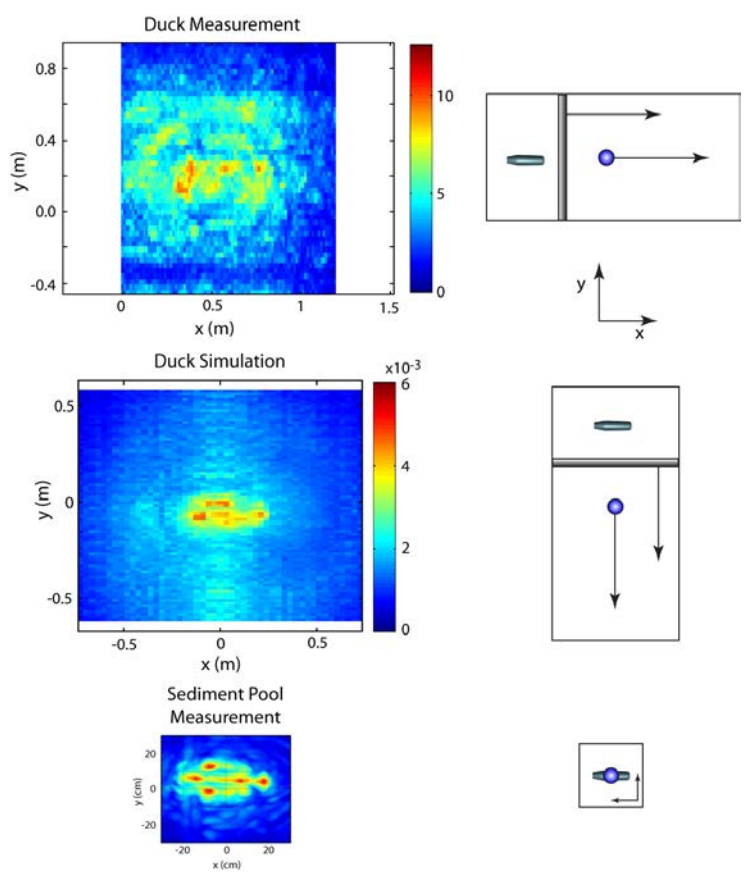

Figure 26. Plan view image from Duck data and measured sediment pool data (horizontal).

Compared to the single source angle bi-static case (sediment pool), the Duck geometry would be expected to produce a much stronger and spatially broader cylindrical highlight specular return. The actual simulated Duck image is shown

in Fig. 27. As can be seen, this high level, spatially extended highlight overwhelms the localized image features from the elastic effects seen in the sediment pool image (lower left of Fig. 26). In order to minimize the impact of this effect, in the Duck images shown in Fig. 26 we have removed a significant portion (but not all) of the strong specular return in both the Duck measurement and Duck simulation by increased time gating.

Notwithstanding these differences, we see that there is some degree of similarity in the three images shown in Fig.26. First, the spatial extents of the targets are similar. Second, there are localized "hot spots" in all three images. In the sediment pool case, the associated studies have shown that these are related to the following mechanisms which are identified in Fig. 28: (1) Elastic waves in the rocket wall which circumnavigate the target and re-radiate back to the fluid. Because this involves a phase matching effect between the waterborne acoustic wave and a circumferential wave in the steel wall, it occurs strongest at frequencies for which the product of acoustic wavenumber and cylinder radius equals 1. Accordingly, for a broadband pulse, the effect will tend to be dominant at a position along the rocket where the radius is changing most rapidly as can be seen in Fig. 28; (2) front and back air cavity resonances; and (3) the cylindrical beam specular highlight.

Considering first the specular highlight, we concluded that the Duck geometry least effective for its observation would be the Duck measurement arrangement. Indeed, one could make the argument that the actual Duck measurement (Fig. 26) does not exhibit a clear cylindrical beam highlight. Similar considerations lead to the conclusion that it should be more observable in the Duck simulations and sediment pool measurements, and this is indeed the case. The more or less omni-directional responses from the air cavity resonances should be observable for all three arrangements, and it is not unreasonable to conclude that this is borne out by examining Fig. 26. (Note that in the case of the Duck measurements and simulations, additional time gating was used to diminish the effect of the specular highlight thus making it possible to observe the other features.) The centers of the two air cavities are physically separated in the actual rocket by about 0.35m, and one can see two highlights separated by this distance in all three plan view images. Finally, analysis of the situation for the circumferential elastic wave re-radiation is somewhat more complicated. However, we have concluded that observation of this wave effect should be better for the Duck measurement versus the simulation. In particular, consideration of the simulation geometry (particulary how the forward-positioned-source and lagging-receiver pair moves perpendicular to the target axis)

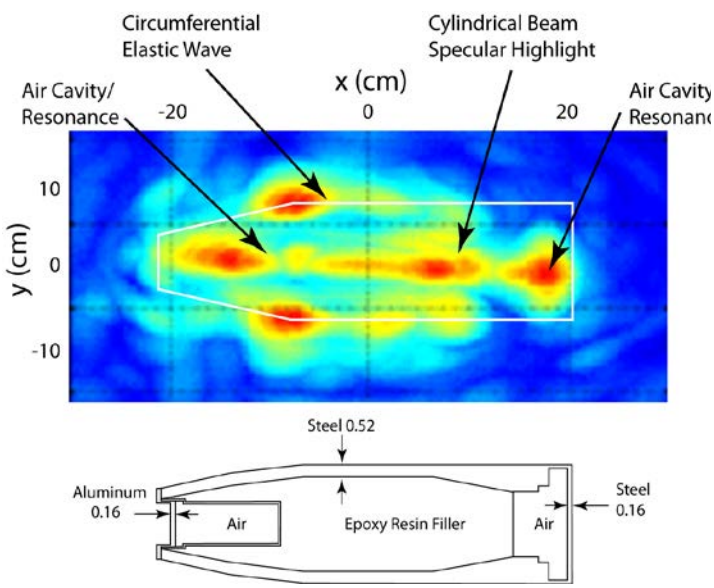

Figure 28. SA mechanism highlights in plan view rocket image.

leads one to believe that the circumferential wave highlight on the far side of the circumference might not be observeable in the simulation. In a plan view image, it is the presence and position of the two circumferential highlights on opposite sides that would coincide with the approximate width of the rocket. In fact, the width of this image in the simulation is about half what it should be, suggesting indeed that the far-side circumferential highlight is missing.

We conclude that the technique by which we reduce the contribution from the specular target return is a reasonable one to implement for data collected using the rail based system and the BOSS system as well. For the BOSS system we envision including both forms of processing – one including the full impact of the specular image and one in which much of the specular image has been filtered out. As explained previously, SAS generated data can be processed to yield both conventional 3-D acoustic images with resolutions much smaller than the target dimensions and scattering cross sections of the UXO-sized volume elements making up the larger illuminated region. The conventional specular dominated images provide direct information regarding buried target size, shape, and orientation whereas the return signal from each target-sized voxel can be presented to an identification algorithm previously trained on UXO structural acoustic features. Furthermore, the specular-filtered image can add additional features such as discussed with reference to Fig. 28.

Next we consider the other two orthogonal view images, i.e the images having depth into the sediment as one of the two display coordinates. We show in Fig. 29 these two images for the for the rocket buried horizontally in the sediment pool facility generated by applying Eq. 2 to scattering data scattering data collected with the synthetically generated 2-D array. In Fig. 30 we show the depth-axial images determined from measurements for the horizontally buried rocket in the Duck sediment. In the target case, one can see features not unlike those seen in corresponding sediment pool images. These include a specular return along the upper length of the target and

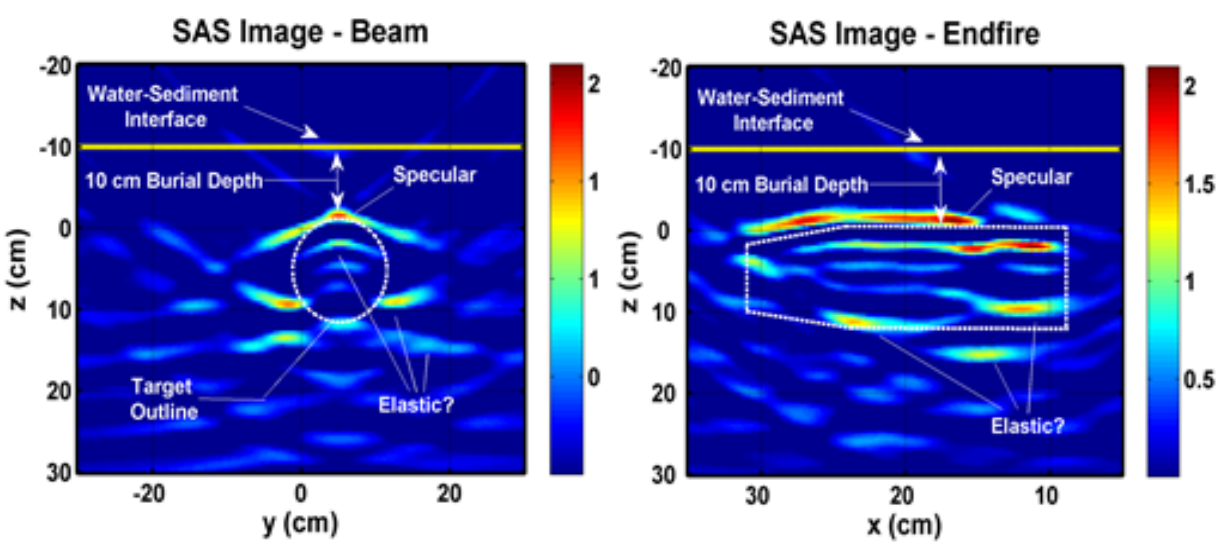

Figure 29. Vertical side view images of rocket buried in sediment pool.

elastic waves originating at lower positions.In Fig. 31 we show the measured depth-radial cross section images for the horizontally buried rocket in the Duck sediment. Again, in the target case, one can see features similar to those seen in the corresponding sediment pool images. These include at the top of the target and elastic wave components at the lower part of the target. In both these Duck measurement related images (Fig. 30 and Fig. 31), one can see the dominant horizontal feature associated with the sediment interface return which we are unable to remove effectively as has been discussed in the previous sections. Again, this is unlike the situation with the sediment pool images where for all intents and purposes, the interface return could be almost completely eliminated as can be seen clearly in each of the sediment pool depth related images (Figs. 29).

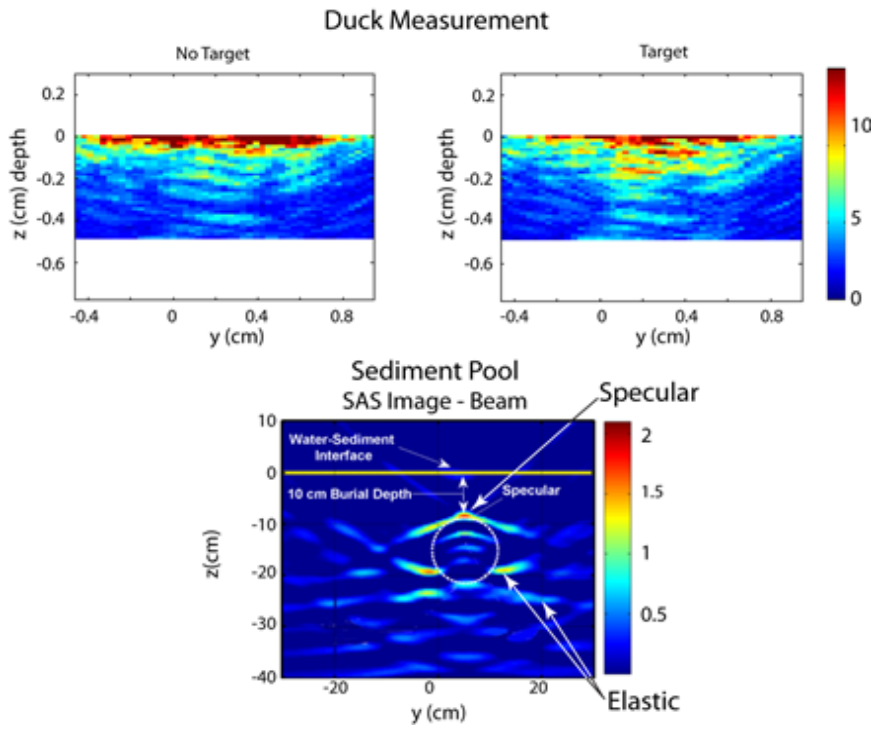

Figure 31. Depth-radial image (horizontal buried rocket target).

Next we compare in Fig. 32 the two orthogonal depth images for the horizontal burial case for the Duck measurements and the Duck simulations. Again, one can see the strong localized image of the sediment interface in both the (Z,X) and (Z,Y) displays. Next we show the two depth images generated from the Duck measurements together with the simulations for the

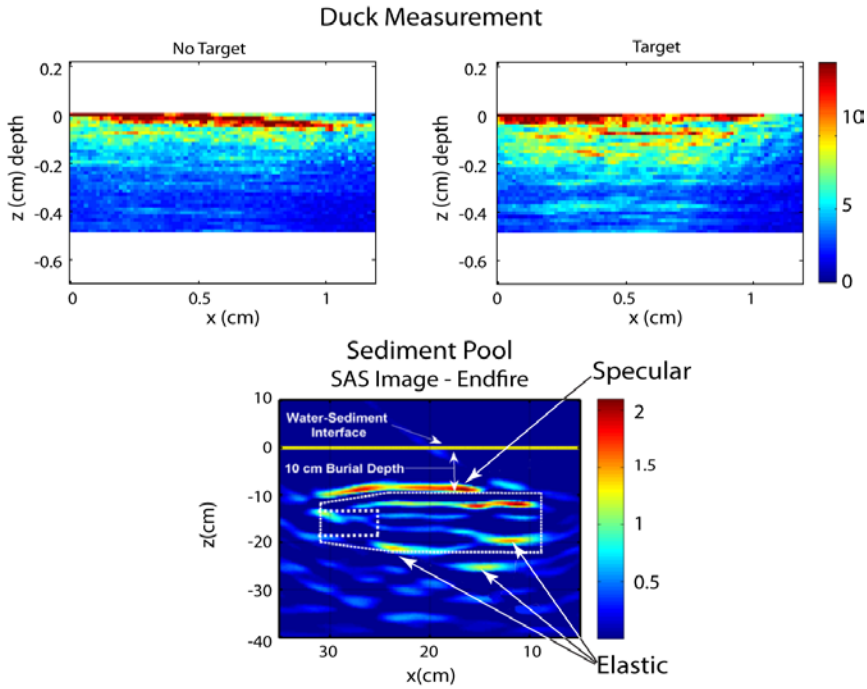

Figure 30. Depth-axial image (horizontal buried rocket target).

rocket buried at 30 degrees. These images are shown in Fig. 33. For the most part, it is difficult to explain these images in the context of simply rotating the corresponding images for the horizontal case shown in Figs. 26, 30 and 31 by 30 degrees in the counterclockwise direction. Further, there appears to be less agreement between measurement and simulation for the 30 degree burial case than is seen for the horizontal burial case. Both of these issues probably result from the sub-standard image generation which is a consequence of the malfunctioning source problem (resulting in artificially extended echoes in time). A curious feature is seen in the depth versus circumferential display (lower left in Fig. 33) in that the strong sediment interface return sags inward (producing a curved wavefront convex to the sediment interface above). This may be an indication that in the 30° case, the burial process has resulted in a sloping sediment interface as was mentioned earlier.

Although we were able to obtain very limited data during the Duck exercise, we thought it would be of interest to intuit how the RVM classification algorithm trained using the target strength correlation and image symmetry features as discussed earlier would perform on the three results obtained in the Duck exercise, namely the no target case and the rocket buried at two different vertical angles. However, both because the rocket in-plane orientation (not burial angles) for the Duck simulation was perpendicular to that for the Duck measurements and the target strength maps were of very low quality owing to the malfunctioning source, we did not attempt to train and test the algorithm as we had done for the sediment pool numerical and experimental data. Instead, we

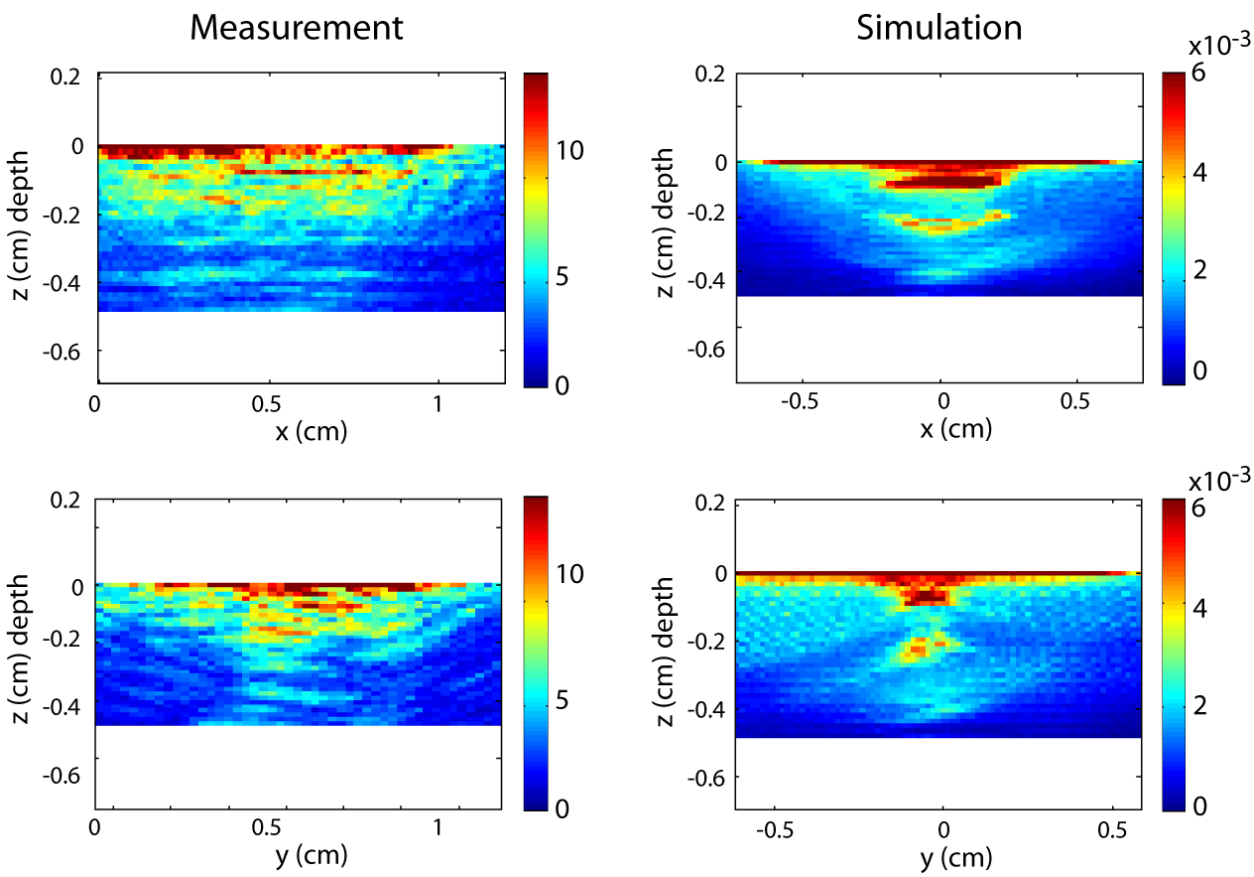

Figure 32. Depth images of rocket buried horizontally.

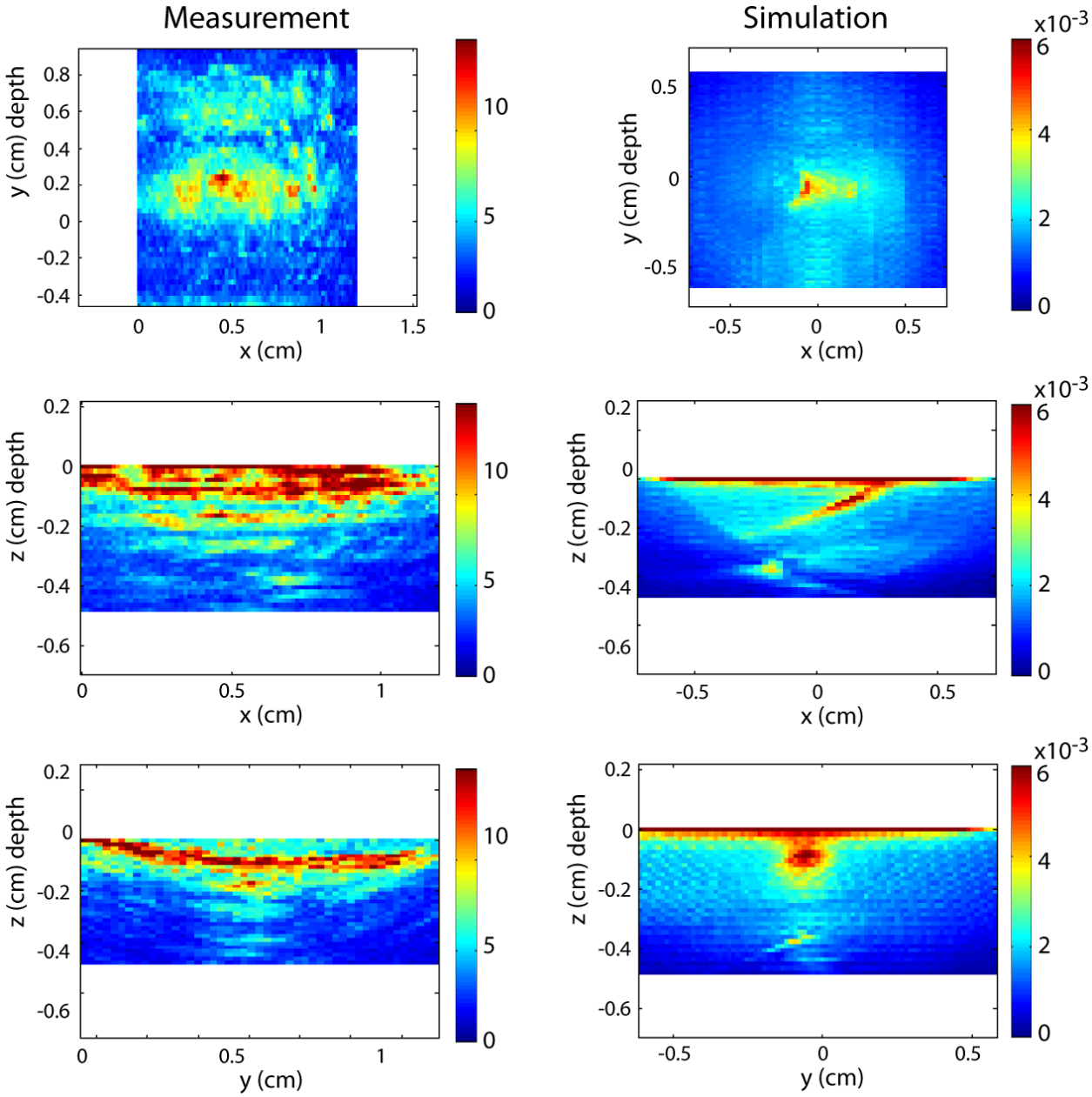

Figure 33. Depth images of rocket buried at 30 degrees.

computed the symmetry feature both from the experimental Duck data and from the simulated Duck data, and the results are displayed in Fig. 34. Again, these have been whitened in the same manner as has been discussed for the sediment pool case[11,14]. Examination of the simulation results shows that except for several problematic burial angle ranges (i.e. near 40 degrees and 140 degrees), the symmetry feature value is -1 or greater. To the extent that the algorithm trained on the sediment pool data is approximately valid for Duck, examination of Fig. 26 together with the simulated results in Fig. 34 suggests that a RVM classifier trained with

symmetry as one feature would still perform well. However, as can also be seen in Fig. 34, the symmetry feature values determined from measurements for the two rocket burial angle cases are well below the range of useful feature numbers. We believe this is a consequence of the poor image quality and low S/N which in turn is a consequence of the source malfunctioning. Nevertheless, we point out that unlike the sediment pool measurement geometry, the system geometry at Duck has an additional effect on the symmetry feature in that its value will depend to some degree on the angle between the in-plane target orientation and the source/receiver scan direction. This may result in reduced performance, even when the S/N is higher. If this is the case, additional simulations involving a range of in-plane target orientation angles would be required for training the RVM algorithm.

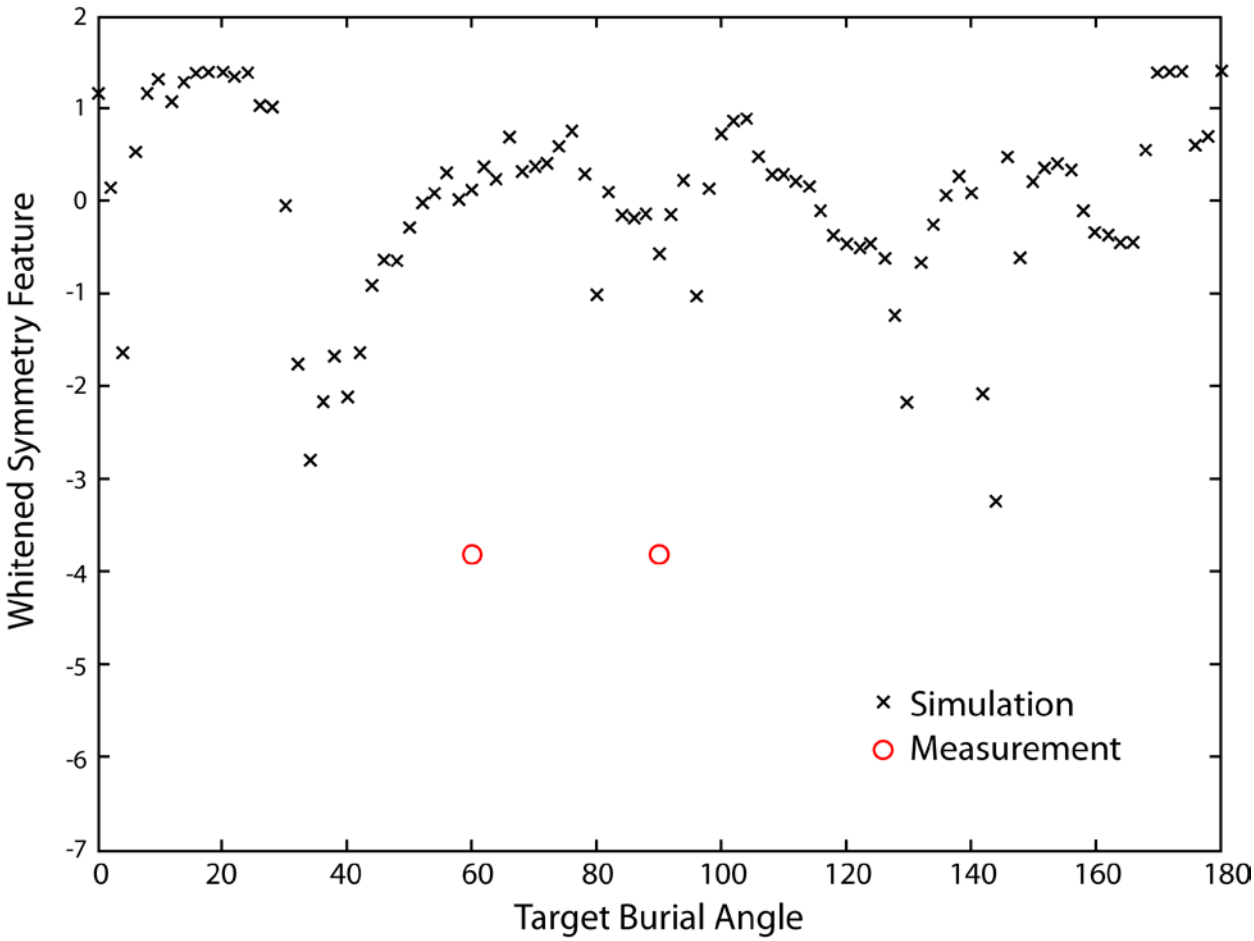

Figure 34. Whitened symmetry feature versus target burial angle for Duck.

Finally, we explore the efficacy of adding another new feature, viz., correlation of the plan-view image. This is in contrast to our earlier correlation feature which was based on the target strength correlation. We consider this because in the Duck case, the measured target strengths are of low quality due to the source malfunctioning whereas the images appear to be of higher quality. Again, both because the rocket in- plane orientation (not burial angles) for the Duck simulation

was perpendicular to that for the Duck measurements and the target strength maps were of very low quality owing to the malfunctioning source, we did not attempt to train and test an RVM algorithm as we had done for the sediment pool numerical and experimental data. Instead, we computed the image correlation feature both from the experimental Duck data and from the simulated Duck data, and the results are displayed in Fig. 35. Here the black circles, x's, and crosses are the plan view correlation features computed from the numerically generated data without noise (the template)

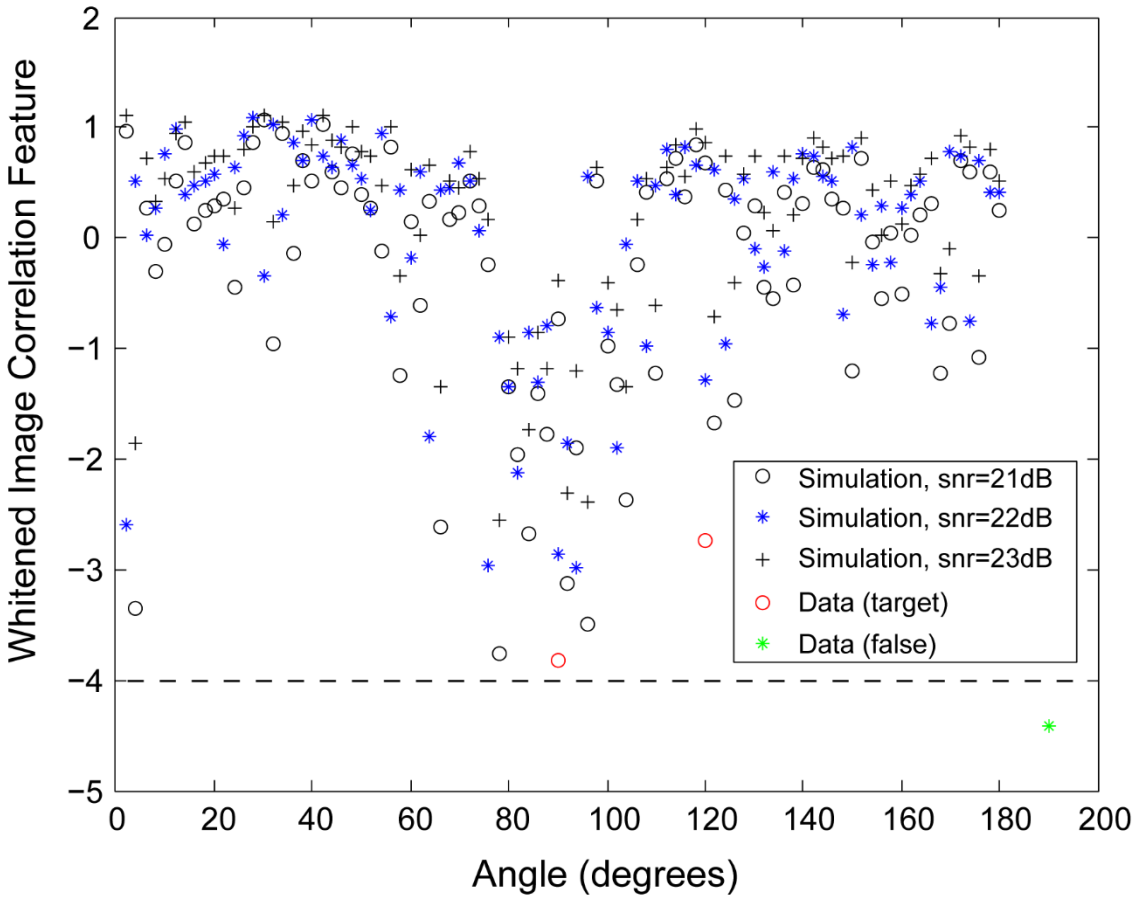

Figure 35. Whitened image correlation feature versus target burial angle for Duck.

correlated against that with noise added to the time signals to give a S/N of 21 dB, 22 dB, and 23 dB, respectively. If we draw a threshold level just low enough to include all the numerically generated data (e.g. at -4), we find that of our three Duck measurement cases (horizontally buried target, 30 degree downward-buried, and no target) the rocket targets fall above the threshold and the no-target case below. In considering the efficacy of exploiting this particular feature, it must be noted again that the quality of the experimental images from which the features have been extracted has been impacted significantly by the source malfunctioning. Further, as described previously, the target orientation in the *x,y* plane is different for the measurement and simulation so that we are using an imperfect template in extracting the correlation features for the

measurements. While the results in Fig. 35 show only marginal target/no target separation, they are based on sparse, problematic experimental data and imperfect templates. The results are, therefore, encouraging, and we intend to explore further the merits of the image correlation feature.

An interesting aspect of this result is that the whitened simulated features shown in Fig. 35 are generally much higher for non-horizontal burial conditions and lowest for the near horizontal cases. This is opposite to what we have found previously for the symmetry and target strength correlation features. This would suggest that the addition of the image correlation feature to the previous feature space may lead to a significant performance improvement.

Scattering from Sediment Inhomogeneous Structure

We now return to the discussion of sound scattering from heterogeneous sediment structure. Starting with Fig. 22 (the Duck measurements) and Fig. 23 (the Duck simulations), we make some heuristic arguments regarding the different echo returns at various times. These are shown in Fig. 36. In the circle on the upper right, the signal can only be due to sediment volume scattering and noise since the interface ringing has died down and there is no target in place. This implies that

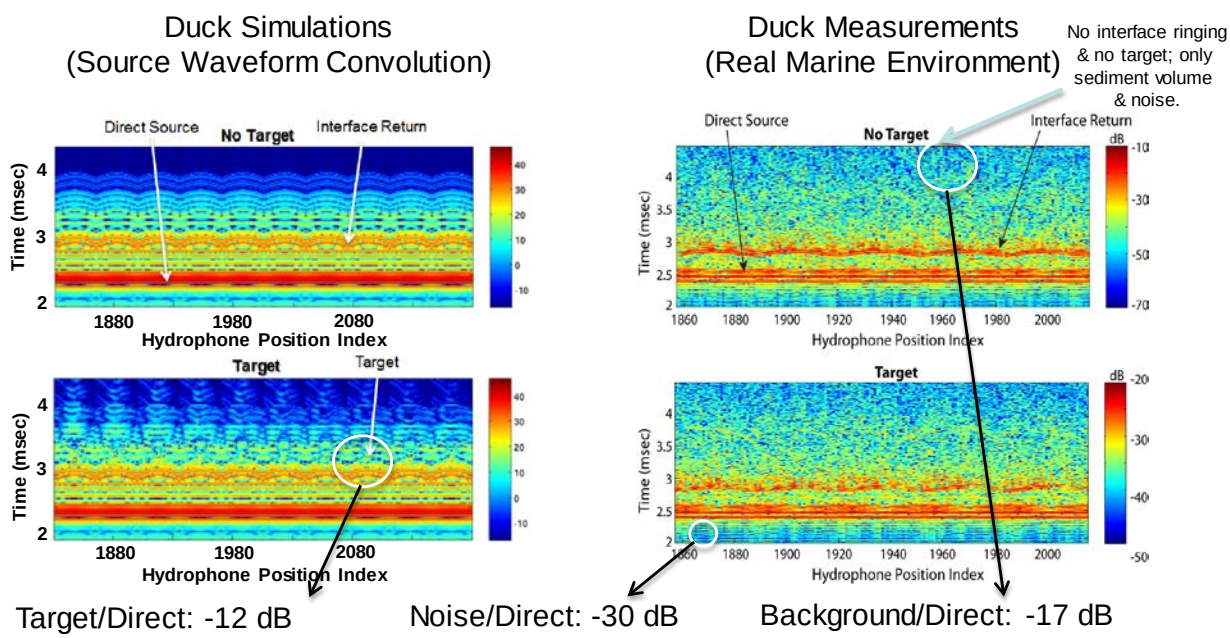

Figure 36. Direct simulations with source convolution (left) and measure signals at receivers (right) with estimates of some of the echo level ratios at various times.

the ratio of background to direct signal level is -17 dB. In the circle on the lower right, the source has not yet been turned on so that we know that the ratio of noise to direct is -30 dB. And in the circle on the left, we can estimate the target return by looking just past the interface return. This

implies that the ratio of target level to direct level is -12 dB. These together imply that: background to target level is -5 dB; noise to target level is -18 dB; and sediment volume scattering to target level is -5 dB. If we look at sufficiently long times in the no target case, we should see for the most part scattering from the sediment volume. If we integrate the levels seen in Fig 37 over all the receivers from 3.4ms out to 4.5ms, as indicated on the left of Fig. 37, these limits would correspond to sediment volume elements from 0.25 meters below the sediment interface to about 1 meter below. The result of this integration is shown in Fig. 38. As can be seen, the calculated levels actually fall with time, i.e. with deeper locations of the sediment scattering volume. At first, this would seem counter-intuitive since the scattering volume (as specified by the delay time) should grow at larger depths (longer times). In fact, we can estimate the depth dependence of this scattering volume by considering Fig. 39 where we indicate the spherical volume element in the sediment throughout which the time delay is roughly constant. This is admittedly an approximation. For example, in the rail system the source and receiver are not co-located. However, this should give a reasonable result regarding the general trend of the scattering levels as a function of time (depth) produced by scattering from inhomogeneous structure

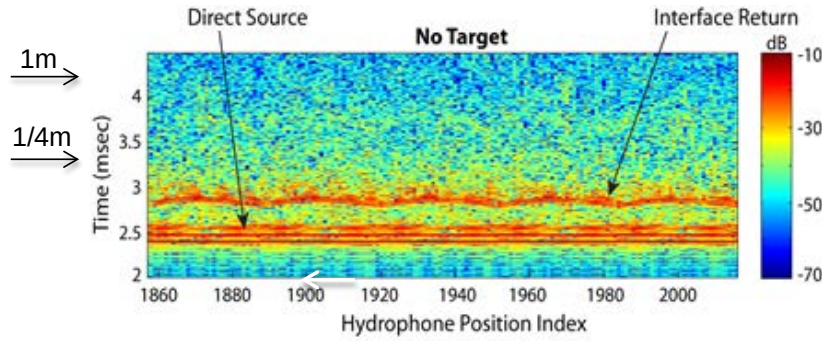

Figure 37. No target case for Duck measurements with 1m and 1/4m scattering locations indicated on the left.

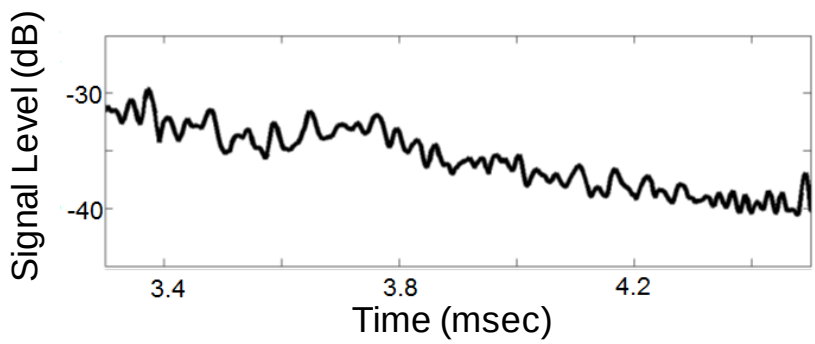

Figure 38. Integrated levels seen in Fig 37 over all the receivers from 3.4ms out to 4.5ms.

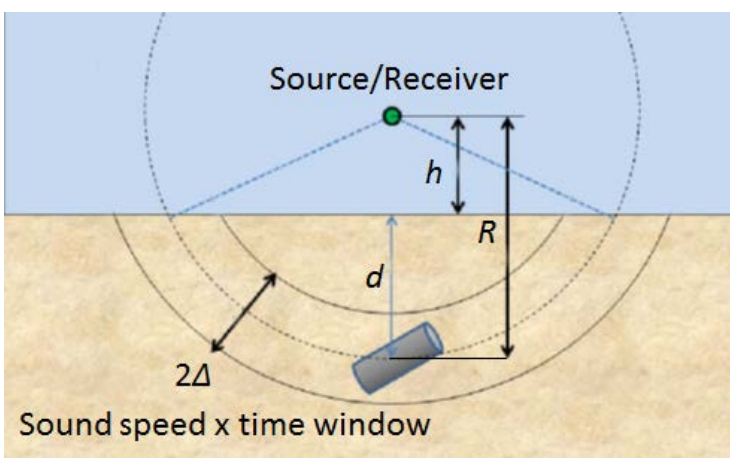

Figure 39. Diagram used to compute the sediment scattering volume within various time windows.

present in the sediment volume. It is straightforward to derive an expression for the scattering volume versus depth using the construct in Fig. 39. We find that the sediment volume in the time window $2\Delta/C$ is given as:

$$Vol(sed) \;=\; 4\pi\,\Delta\,[d^2 + dh + 2\Delta/3]. \qquad (3)$$

At long times, Eq.(3) predicts that the sediment scattering volume *grows* with time as t^2 which is opposite to what we see in the data (Fig. 38). We believe this difference is a consequence of the impact of sediment absorption whose frequency dependence is shown in Fig. 40 for a sandy sediment[18]. In Fig. 40, the dashed line (at frequencies above our band) indicates the range of absorption values seen from different experiments. Using the values of absorption shown here for the frequencies within our band and including these in the analysis leading to Eq. (3) give the results shown in Fig. 41. Here we present the predicted sediment scattering volume versus the time window center depth for two values of sediment absorption, α = 0 and α = 7 dB/m (the latter being the value from Fig. 40 seen at the center of our frequency band). In the displays shown in Fig. 41, the arrows indicate the 0.25m and 1.0m points beneath the sediment interface. The results for the α = 0 case show a scattering volume increasing with time in agreement with Eq.(3). However, as conjectured, the inclusion of a reasonable absorption coefficient into the analysis shows a sediment scattering volume which decreases with depth at long times in agreement with the experimental results shown in Fig. 38.

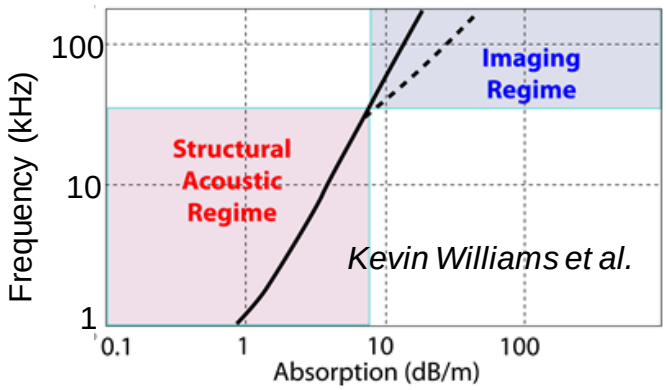

Figure 40. Sandy sediment sound absorption (Kevin Williams, et. al. Ref. 18 .)

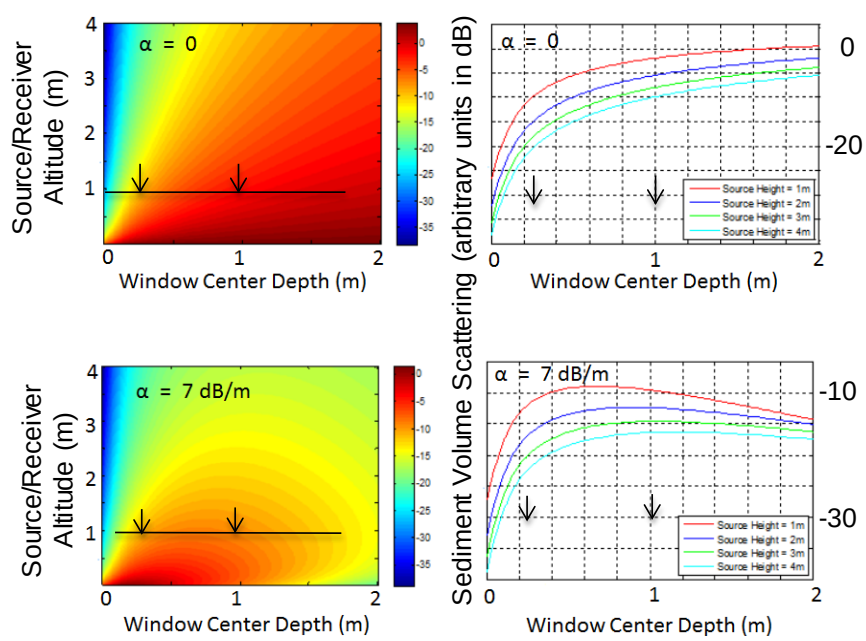

Figure 41. Predicted sediment scattering volume from Eq. 3 weighted by signal absorption versus window center depth.

We conclude from this that the sediment volume scattering

levels experienced at Duck are higher than those experienced in our more homogeneous pool facility experiments. It is important to recognize that this is a consequence of two factors: (1) the more inhomogeneous sediment at Duck and (2) the non-ideal elongated source time waveform used in the Duck experiments. As we determined earlier, sediment volume scattering level to target scattering level is -5 dB. We can estimate the impact associated with the elongated source time waveform by comparing it to the desired narrower impulse shown in Fig.20. This yields a potential processing gain of ~14 dB going from the long waveform shown on the bottom of Fig. 20 to that shown in the top. Had we been able to use the narrower waveform, the UXO echo detected at Duck would have been ~ 19 dB higher than the reverberant sediment return. If we consider the target echo response levels (see Ref. 17) for the range of UXO which we have studied (the largest being a 155mm shell down to the smallest a 25mm cartridge), we would find that the relative levels of the five inch rocket (the target at Duck) to the smallest (the 25mm cartridge) is -10 dB. This implies that with the narrow incident waveform, we would have a target-to-sediment volume echo ratio for the 25mm cartridge of +5 dB (ratio observed for the 5 inch rocket) -10 dB (relative TS of 25mm cartridge versus 5 inch rocket) +14 dB processing gain going from elongated to narrow incident waveform) or +9 dB. This is a level sufficient to support both detection and classification. With the narrower time waveform, the Duck target level to sediment scattering level would have been 19 dB. In the sediment pool studies, this ratio was found to be > 22 dB. This implies that the sediment volume scattering at Duck was >3 dB higher than that from the more homogeneous sediment pool.

The conclusions to be drawn from the exercise at Duck and the subsequent analysis are as follows.

(1) Volume scattering was detected and quantified. The Duck sediment produced volume scattering at least 50% higher than that from the more homogeneous pool facility sediment.

(2) Even when operating in a high sediment volume scattering environment like the shell and sandy silt bottom of post-hurricane Duck, there should be a high enough target echo to sediment scattering ratio to allow detection and classification of targets as small as a 25mm cartridge for burials on the order of 10 cm.

(3) Acoustic noise levels were as expected. The background acoustic noise was nominally 18 dB below the buried rocket echo levels. This is a positive result: previous simulations/RVM tests using the low noise sediment pool facility data added approximately this level of random noise to the time signals.

(4) The image symmetry feature was ineffective. Image symmetry exploited in the sediment pool work did not yield an effective classifying feature at Duck. This is due mainly to poor image quality because of the malfunctioning source, a conclusion to be validated by further analysis and measurements.

(5) A new image correlation feature was introduced which appears to have merit, especially regarding large non-horizontal burial angles.

(6) The RVM ID algorithm was extended. The ID algorithm demonstrated with the bi-static sediment pool data has been extended to the more complicated multi-static rail and BOSS configurations. This includes the introduction of a new concept: short time (specular) versus long time (elastic) images.

Measurements in the Gulf of Mexico

Background

In our work leading up to, and after, our measurements off the coast of Duck, NC, we developed a strategy for generating constructs for extracting target classifying features from the scattering data that would be obtained by flying an AUV-based sonar (BOSS) over a buried target field. As shown in Fig. 42, the constructs included: (a) the specular plan view and depth view images. These images are generated accepting all data within the echo time window so that specular scattering dominates over elastic effects allowing the formation of conventional images that conform to the target's shape[19,20]; (b) the specular-filtered plan view image. This is generated by using time windowing to suppress specular scattering in order to produce images with elastic highlights; (c) 2-D target strength where the scattering strengths are mapped versus (x,*y*) at each frequency; and (d) the target strength versus frequency as a function of *x* or *y* (or aspect[21,22]) also called *acoustic color*. We note that target strength shown here is defined in terms of the pressure magnitude; but we can derive features from the complex pressure as well.

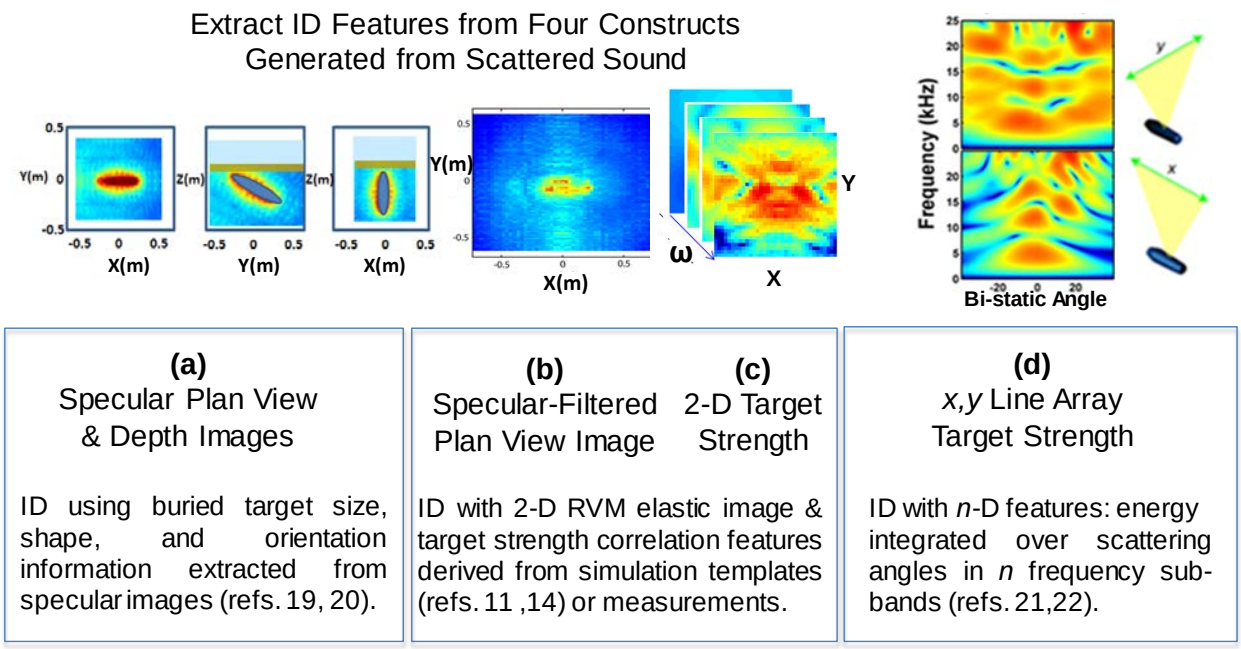

Figure 42. Constructs to be generated from the BOSS scattering data.

BOSS Exercises off the Coast of Panama City, FL

In June of 2013 NSWC, together with NRL and Bluefin Robotics, successfully flew the BOSS structural acoustic sonar in the Gulf of Mexico over a target field in which were buried nine NRL simulant-filled UXO's and 2 false targets and some 20 proud targets. Through this study we established (1) the ability to produce both 3-D images and target strength spatial/spectral maps of the *buried* targets and (2) that UXO targets and false targets can be separated using a multi-dimensional but otherwise straightforward feature set. The details of the BOSS system are described in the Appendix.

The general location of the target field is shown in Fig. 43 and is roughly 2 miles off the coast of Panama City, Florida. This location was the sight of a broader set of measurements made about the same time as part of the so-called TREX-13 exercise. For that program, a proud target field

Locations of the TREX13 operation areas for the June 24-25, 2013 measurements:

BOSS/SERDP operation area is 20 yards North of the RV Sharp center located at 30°03.5906'N 85°40.8650'W

The target deployment area is located ~ 8NM S-SE from NSWC PC, and the 30m by 40m box corner positions are:

30°03.6170'N 085°40.8775'W
30°03.6170'N 085°40.8525'W
30°03.6005'N 085°40.8525'W
30°03.6005'N 085°40.8775'W

Allowing for some over-scanning, the corner positions of the 50m by 80m surveyed box are:

30°03.6170'N 085°40.8900'W
30°03.6170'N 085°40.8400'W
30°03.5900'N 085°40.8400'W
30°03.5900'N 085°40.8900'W

Map of General Area

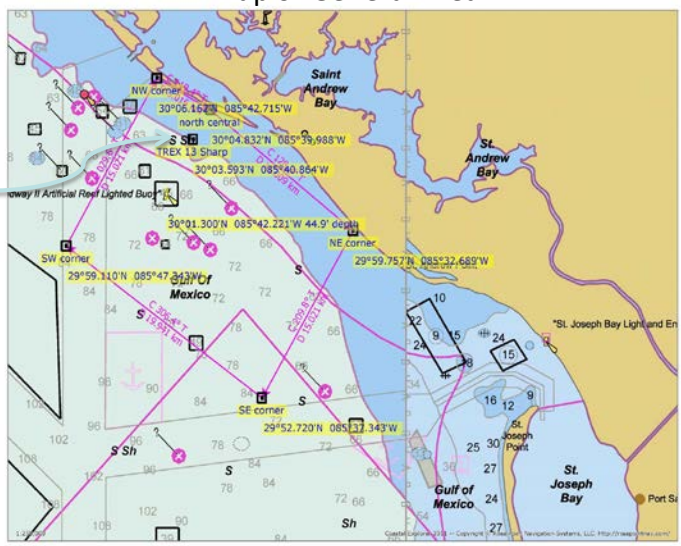

Figure 43. General operations area for TREX-13 off the Coast of Panama City, FL.

was created (see the proud targets listed in Table 3), and scattering measurements were carried out using sources and receivers mounted on towers along the northern perimeter of the target field. These assets were removed just prior to our exercise using the BOSS AUV system.

TABLE 3 – Proud and Buried Target List

Proud Targets				NRL Simulant–Filled Buried Targets	
T1	DEU Trainer	T14	Scuba Tank w/water w stem	N1	5inch Rocket nose-up 60°
T2	Rock	T15	2:1 Aspect Phone Pole Section	N2	5inch Rocket nose-up 30°
T3	55 Gallon Filled Drum	T17	2 ft Aluminum Cylinder	N3	5inch Rocket horizontal
T5	5:1 Aspect Phone Pole Section	T18	Cement Block	N4	155mm Projectile horizontal
T7	3ft Aluminum Cylinder	T19	Tire	N5	155mm Projectile horizontal 90°

T8	155mm Projectile w/o collar	T20	Aluminum UXO Replica	N6	155mm Projectile horizontal 20cm
T9	155mm Projectile w/ collar	T22	Original Material UXO	N7	155mm Projectile nose-up 30º
T10	Panel Target	T25	Bullet #1	N8	155mm Projectile nose-up 60º
T11	152 mm TP-T	T28	155mm Projectile w/collar	N9	120mm Mortar horizontal
T12	81mm Mortar	T29	Bullet #2	N10	Large Rock (no simulant)
T13	Scuba Tank w/water w/o stem	T30	Finned Shell #1	N11	Cinder Block (no simulant)

The nine buried NRL simulant filled UXOs include three 5 inch rockets, five 155mm projectiles, and a 120mm mortar. The two buried NRL false targets included a large rock and a conventional cinder block. These eleven NRL targets were buried by Dr. Kevin Williams (Applied Physics Laboratory at University of Washington) and his diving team aided by Dr. Michael Richardson about three weeks before the BOSS exercise. The plan was to bury all but one of the NRL targets in such a way that the highest point of the target would be 10cm below the sediment-water interface. The one exception was to be a horizontally buried 155mm projectile at a 50cm depth. Generally, the divers executed the plan fairly well given the difficulty of burying such relatively large objects in 60 foot waters. Although it was not possible to know the burial condition of each target precisely, the general consensus was that the depth and orientation achieved for each target were roughly according to plan. Two exceptions were that the cinder block burial depth was less than 10cm and the deeply buried 155mm projectile was closer to 20cm from the sediment interface. There were 23 targets placed proud on the sediment. These included some UXOs not filled with simulant, a rock, and a number of man-made objects. Together with the buried rock and cinderblock, 7 of these 23 proud targets serve as false targets in the target feature separation studies to be discussed later. These seven include the rock (T2), the 55 gallon water filled drum (T3), the 5:1 aspect telephone pole section (T5), the panel (T10 or CP), the 2:1 aspect telephone pole section (T15), the cement block (T18), and the tire (T19). The proud and buried targets in the target field are listed and labelled in Table 1. Their rough relative positions within the target field are illustrated in Fig. 44.

Figure 44. Planned placement of the targets listed in Table 1.

We show in Fig. 45 the many east/west and north/south flight paths executed in the June 2013 exercise by the AUV. In Fig. 46, we show the diagonal flight paths which were taken on day 2. We discuss below the progress we have made in processing the received signals received on the BOSS wing sensors for many of the east/west and diagonal flight paths described in Fig. 45 and 46. The data for the north/south flight paths has not yet been analyzed.

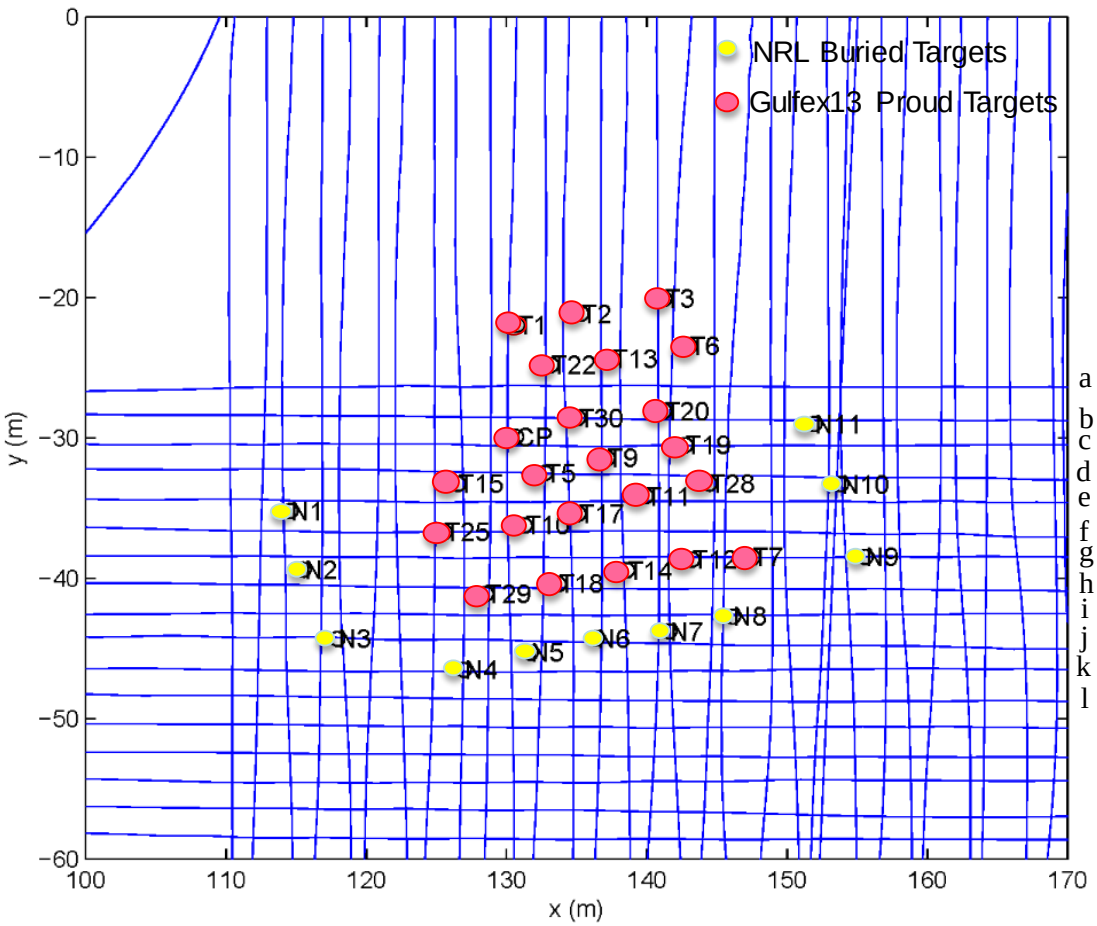

Figure 45. Target locations relative to the east-west and north-south AUV flight paths.

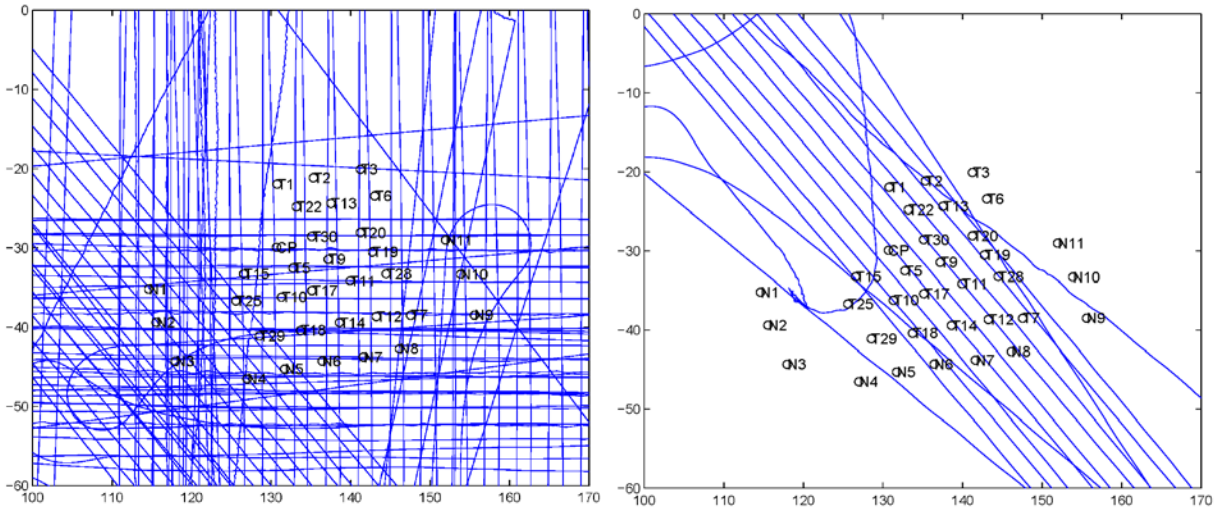

Figure 46. Addition to Fig. 45 of the diagonal flight paths.

Analysis of BOSS Data

In what follows, the vehicle moves in the x-direction. To produce images or do SAS processing, the measured field is initially time windowed to remove the bottom bounce (and everything arriving prior to it) and the surface reflection (with everything arriving after it). First, using the measured field from 40 pings (40 x positions of the vehicle), the image is produced as a function of x,y,z. The frequency range of 3 to 20 kHz is used to produce this image. Next the images at the same (x,y,z) locations are produced from a different set of 40 pings (vehicle x positions). This is repeated to produce a total of 33 images at a given (x,y,z) location, each from a different set of 40 pings. Out of the 33 images at a given (x,y,z) location, the maximum image value is chosen which becomes the final image at that (x,y,z) location.

To obtain a 2-d plot as a function of x and y, the maximum image value as a function of z is chosen for a given (x,y) coordinate. Similarly, to obtain a plot as a function of (y,z), the maximum value along x is picked and the same with the plot as a function of (x,z). The maximum in the y-direction is used.

To obtain the "long time" plan view image as a function of x and y from the three dimensional image, the image values that arrive early are set equal to zero. Then the maximum as a function of z is computed.

From the images, the coordinates of the center of the target is determined. At that location, SAS processing is performed. For each combination of source/receiver location, the source-to-target to-receiver distances are known. For each receiver location, the measured signals for neighboring receiver locations are time-aligned, and their mean value computed. The result, $p(x,y)$, becomes the SAS processed field value at that receiver location. At each receiver (y), $20\log p(x)$ is the acoustic color. Next, $20\log|p|$ is plotted as a function of x and frequency for the y-value that is closest to the center of the receiver array. $20\log|p|$ is also plotted as a function of x and y for given frequencies.

The six “constructs” described above were extracted from the measured data and are shown in the following figures (Fig. 47 – Fig. 49) for each of the nine buried UXO targets and for each of the two buried NRL non-UXO targets. For the 11 targets, individual paths were chosen that under inspection produced the best images; and the specific paths are indicated in the three figures. Note that as discussed in the previous paragraph, TS is displayed without including the standard range factor.

The constructs obtained for all the NRL buried targets are in a general sense similar. The AUV was also flown over diagonal flight paths, and the constructs from these are similar as well. We have not yet considered or analyzed the north/south path data, but we also would expect these to be similar. The depth images shown in Figs 47 – Figs. 49, in almost all cases, indicate a buried target. In general, the tips of the targets buried at a vertical angle are very near the surface as planned (and as expected since it would be very difficult to bury such a target with its bottom >> 10cm from the surface). In the case of the 60° five inch rocket, the image does not indicate the actual burial angle very well. All 155mm projectile depth views used path h, while three

different paths (e,h, and j) were used for the three rockets. The plan view images for the 155mm target used flight path h and are reasonable. The horizontal buried target N4 looks long and oriented ~20° above scan line; the rotated horizontal target N5 shows two dots; the deep target N6 looks long and is ~ along the scan line; the 30° target N7 looks elongated but shorter as it should and is ~30°

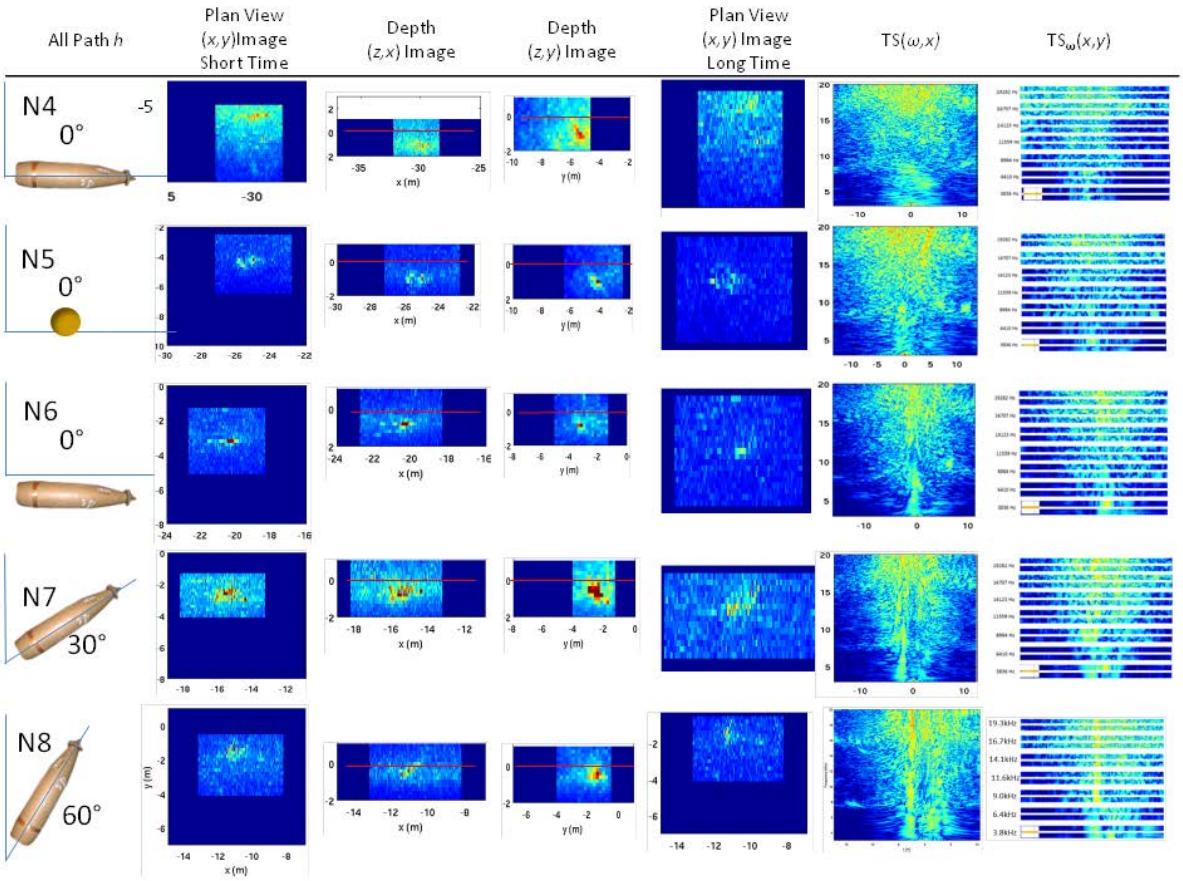

Figure 47. The six "constructs" described in Fig. 42 extracted from the measured data for the five buried 155mm shell.

off scan line; and the 60° target N8 looks elongated but shorter as it should and is ~30° off scan line. The plan view images for the three five inch rockets used flight paths j, h, and e. The plan view image of the cinderblock N11 is very strong and is probably oriented ~ 15° above flight path e direction. Comparisons of the long time and short time images need more careful work. The rough observations here for the long time images are: N4,N5 same structure but cloudier; N6 same structure but weaker; N7 probably a better image; N8 back side feature emphasized; N3 front side feature emphasized; N2 less structure; N1,N9 same structure less background; N10 center structure emphasized; N11 same but better focused structure. Target Strength vs (ω,x) (acoustic color) appears to be of high quality and high S/N for all targets. This is in contrast to the results obtained earlier at Duck, NC with the rail-based sonar. For the 155mm rocket, there are several features identified with specific mechanisms: (a) specular scatter off the tapered body; (b) filler elastic wave at quartering[3]; and (c) scattering from the front disc structure. There

are two other features with no mechanism suggested, and these are: (d) narrow-band feature (@ ~ 16 kHz) which sweeps over all x (the scan co-ordinate); and (e) broad-band level increases at the high frequencies over a limited x range centered around the target location. In general, the features associated with (a) through (e) more or less persist for all burial conditions with the followings caveats: (a) is not clear for N4; and (b) is not obvious on +x side of scan. For the 5 inch rocket, there are also several features in the acoustic color plots with which we believe we can associate specific mechanisms:

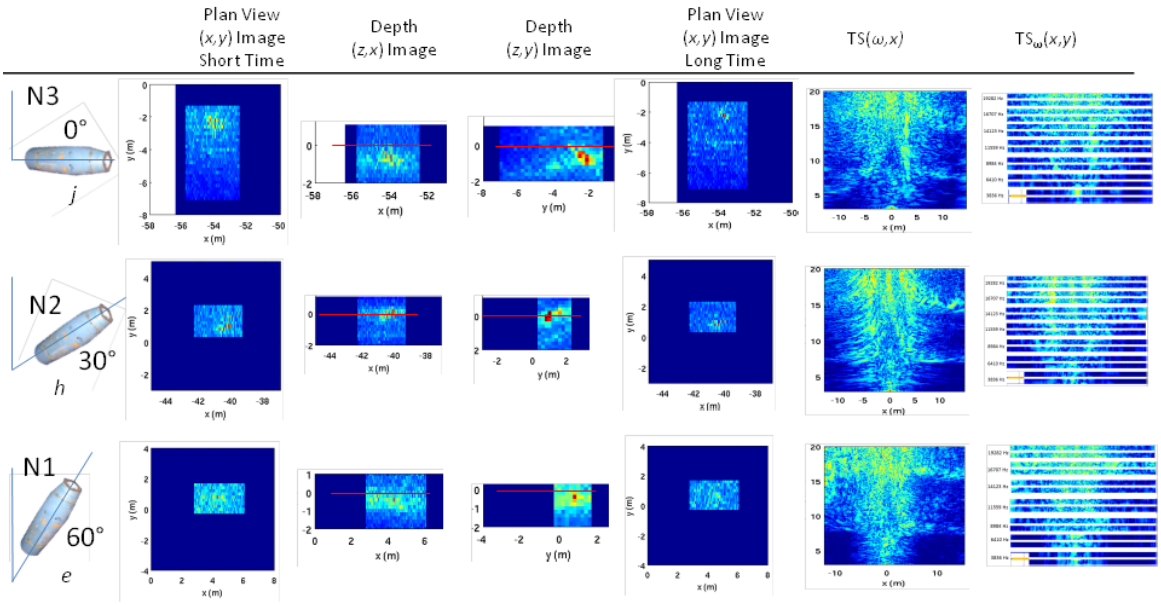

Figure 48. The six "constructs" described in Fig. 42 extracted from the measured data for the three buried five inch rockets.

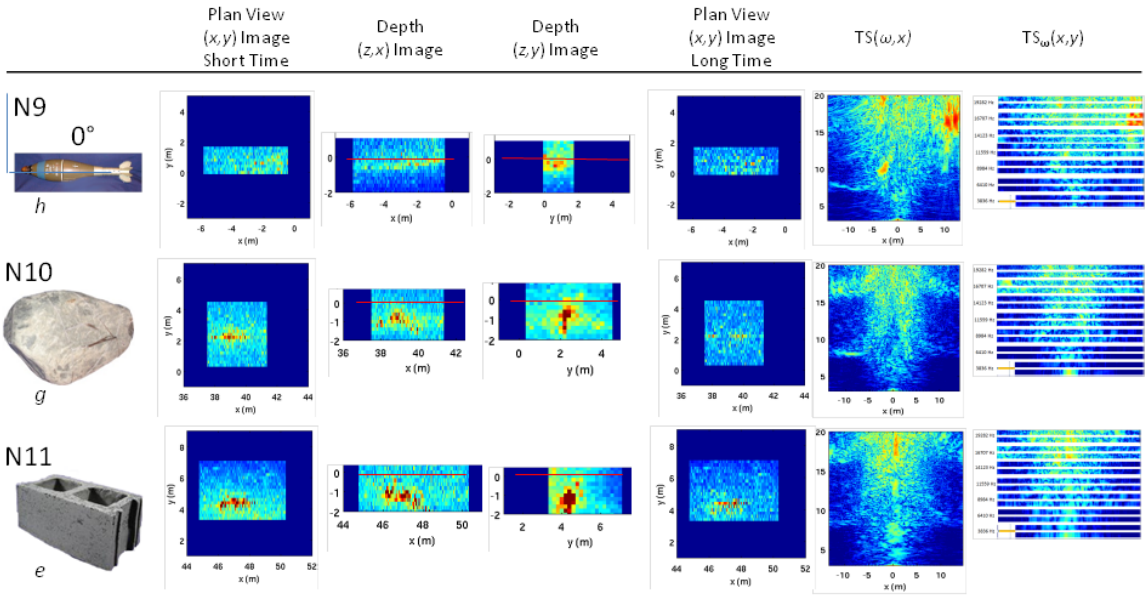

Figure 49. The six "constructs" described in Fig. 42 extracted from the measured data for the 120mm mortar, the rock, and the cinderblock.

filler elastic wave at quartering; specular off the beam (at higher frequencies); specular off taper; and perhaps front end scattering at higher frequencies. For the 120mm mortar, it appears that one major feature is the broadband, wide-angle specular scattering from the continuously tapered shape. There is also a strong feature which is perhaps scattering from the stern fin structure and possibly filler elastic wave scattering at quartering.

In the following figures, we illustrate where in acoustic color space some of these mechanisms express themselves. The first of these is Fig. 50 where we show (in arbitrary decibel units) the acoustic color plots, i.e. target scattering levels versus frequency and x position of the receiver for target N8, the 155mm shell buried nose-up 60 degrees. Note that the x position can be converted to the more conventional parameter, the receiver angle. In this and the following figures, we have illustrated beneath the plots the various source (black sphere) and receiver (blue bar) locations along x to help one to visualize the source/receiver angles relative to the x axis of the color plots. In this manner, one could recognize, for example, that filler elastic waves at quartering do indeed appear about where the source-receiver to target angle is 45°; and that the front disc return presents itself where the source/receiver are head-on to the target front end.

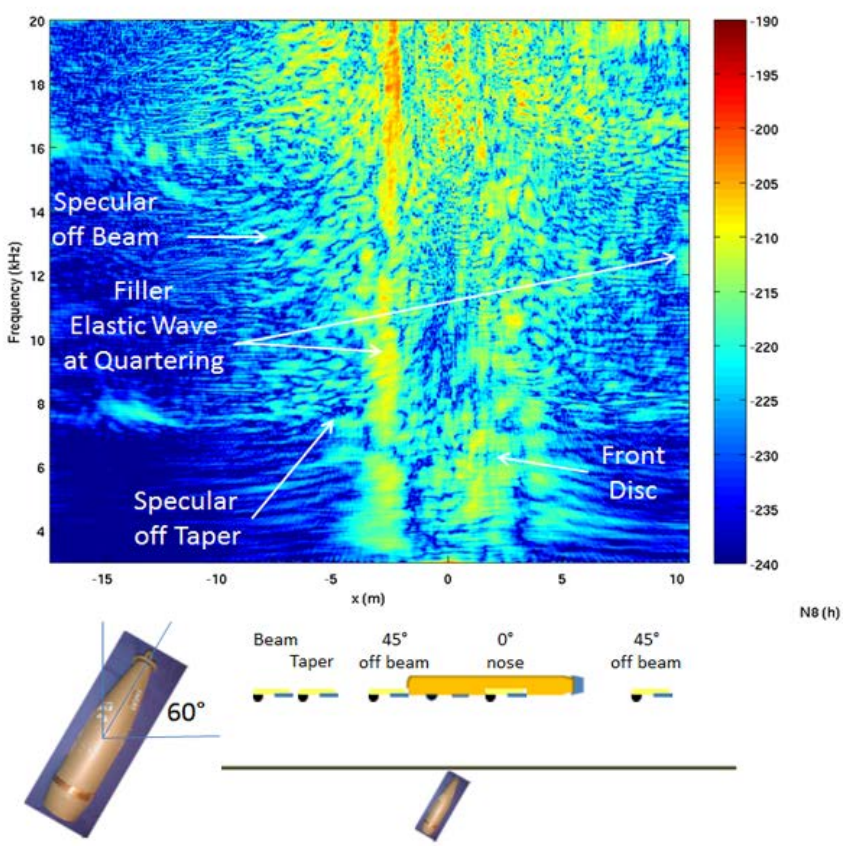

Figure 50. Acoustic color plots (arbitrary decibel units), i.e. target scattering levels versus frequency and x position of the receiver for target N8, the 155mm shell buried nose-up 60 degrees. We have illustrated beneath the plots the various source (black sphere) and receiver (blue bar) locations along x to help one visualize the source/receiver angles relative to the x axis of the color plots.

In Fig. 51 we show the similar display for target N6, the horizontally buried 155mm shell. In this case we can recognize the specular return from both the beam and taper of the target and the elastic waves at quartering.

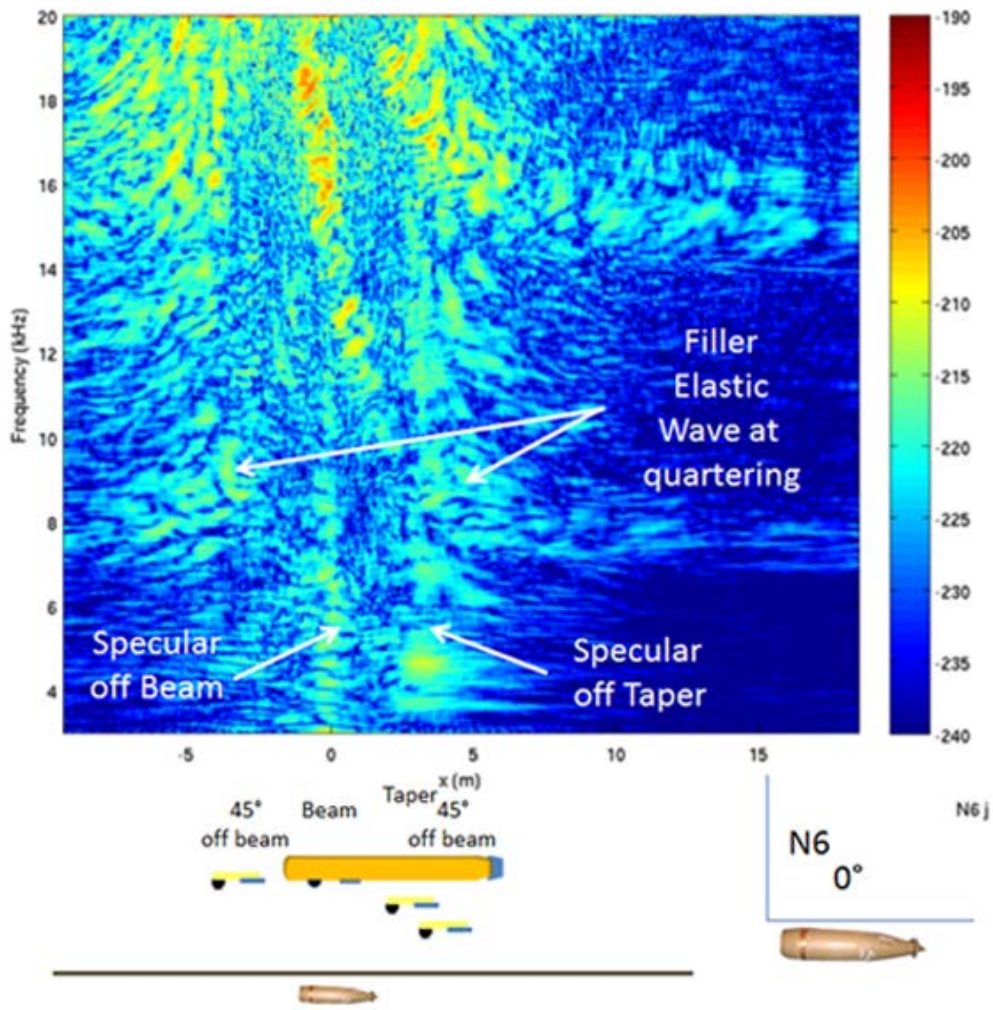

Figure 51. Acoustic color plots (arbitrary decibel units), i.e. target scattering levels versus frequency and x position of the receiver for target N6, the five inch rocket buried horizontally. We have illustrated beneath the plots the various source (black sphere) and receiver (blue bar) locations along x to help one visualize the source/receiver angles relative to the x axis of the color plots.

In Fig. 52 we show a comparison of the acoustic color plots for the 155mm shell obtained in earlier measurements made in the NRL sediment pool and the BOSS measurements. Both targets are horizontal, with the BOSS target buried 10cm beneath the sediment interface and the

sediment pool target proud on the sediment surface. With the aid of the added white lines, we can clearly see the similarity between the color plots for the highly controlled pool situation and the less controlled AUV-based measurements. This gives added confidence that we should be able to collect robust acoustic color data with the BOSS system.

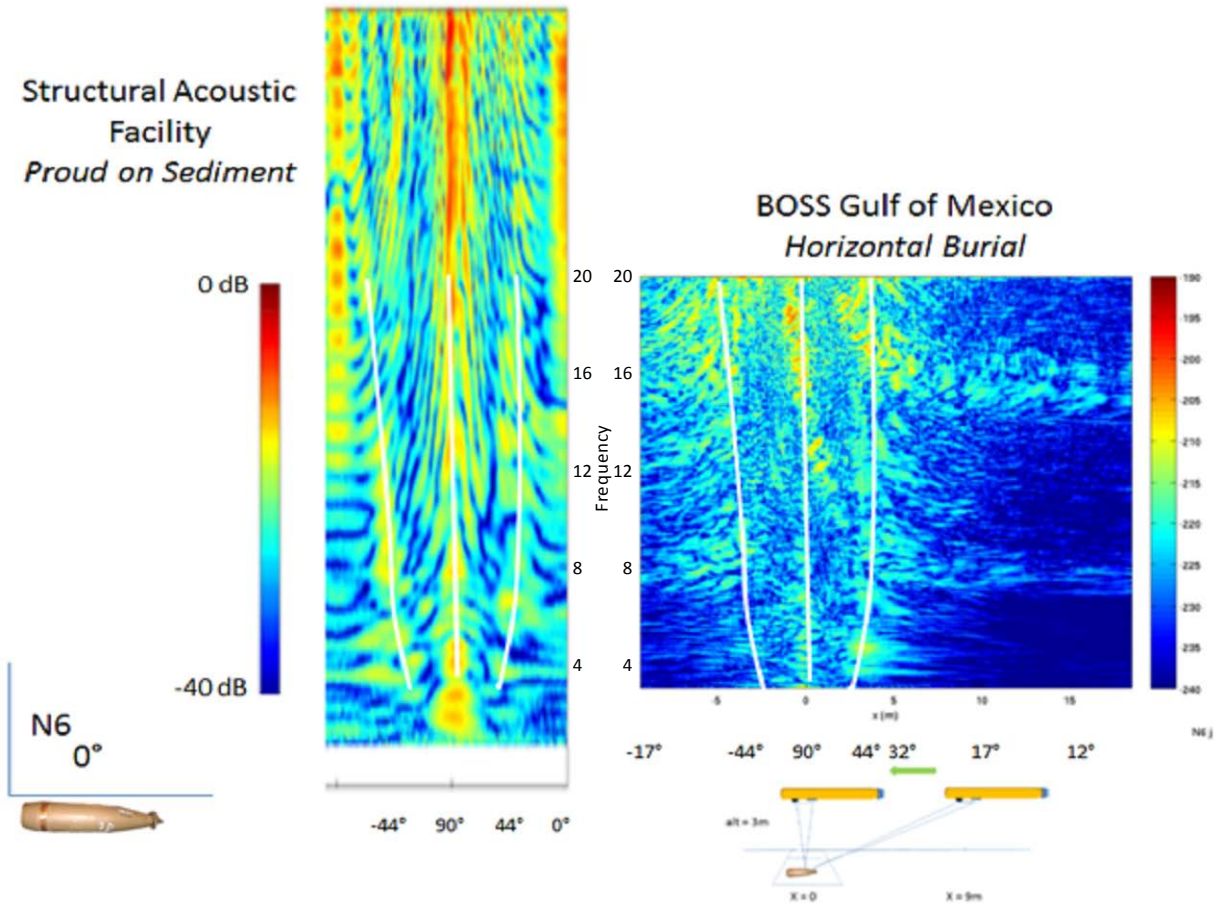

Figure 52. Acoustic color plots for N6 the 155mm shell buried horizontally. On the left, earlier measurement made in the sediment pool facility versus angle with the target proud. On the right, BOSS measurement (arbitrary decibel units) versus x position with target buried.

If we compare the results shown in Fig. 51 for the buried, simulant-filled 155mm Howitzer shell with results reported by Lim et al[23] for a proud 155mm Howitzer shell measured in their Pond facility, we find general agreement in the acoustic color map below 12 kHz. Noteworthy differences include the following: between 12 kHz and 20 kHz our data shows strong returns around quartering aspects whereas there are almost nulls in the latter. Both displays do show strong swaths of returns around quartering below 12 kHz. The broader-band (~ 12 kHz to ~20 kHz) quartering returns were observed in earlier measurements[23] made in our large pool facility on not only our 155mm target but several other simulant-filled UXO as well. We explained this response in terms of phase matching of the water-borne acoustic wave at these angles to interior waves in the filler. The longitudinal speed, C_L, is relatively low in the filler material, typically somewhere between 2000 m/s and 2900 m/s, and one could get phase matching for a waterborne wave incident at an angle from bow of θ to a longitudinal wave in the filler traveling along the length of the somewhat cylindrical target. Phase matching would occur when $\lambda_{filler} = \lambda_{water}/\cos\theta$,

or when $\theta = \theta_P = \cos^{-1} (C_{water}/C_{filler})$. The efficiency of phase-matching grows if multiple wavelengths extend along the target length, ergo the mechanism's appearance in our data at the higher frequencies. (At 10 kHz, there is barely a wavelength along the target's length.) The forcing acoustic pressure working against the casing (steel) material could be transferred to the interior filler material, and a longitudinal wave could be excited in the filler which would travel down the cylinder. If it could reflect efficiently from the target's end, it would travel back, and through the same phase-matching mechanism launch a backscattered echo. If the end conditions are right at front and back, we should see returns from this effect at θ_P, $180° \pm \theta_P$, and $360 - \theta_P$. The lowest value given above for the longitudinal speed in the filler (2000m/s) would give $\theta_P \sim 41°$ predicting returns at angles of 41°, 139°, 221°, and 319°. This is more or less what we see for the UXOs we have studied. However, this quartering response continues up beyond even 30 kHz in contrast to the case for Lim et al[23]. In the latter case, the shell contains no filler material which helps support our supposition of the broadband quartering mechanism being related to elastic waves in the filler. This conjecture is further supported by the results reported by Zampoli et al[24] for a proud, solid aluminum replica of a UXO similar in shape and size to the 155mm shell. Their results also show little response at quartering above 12 kHz similar to what is reported by Lim et al[23].

A final example is shown in Fig. 53 where the acoustic color display is shown for the horizontally buried 120mm mortar. Several new highlights are indicated here including that from the fin structure and the nose, and the broad angular swath coming from the continuously tapered body.

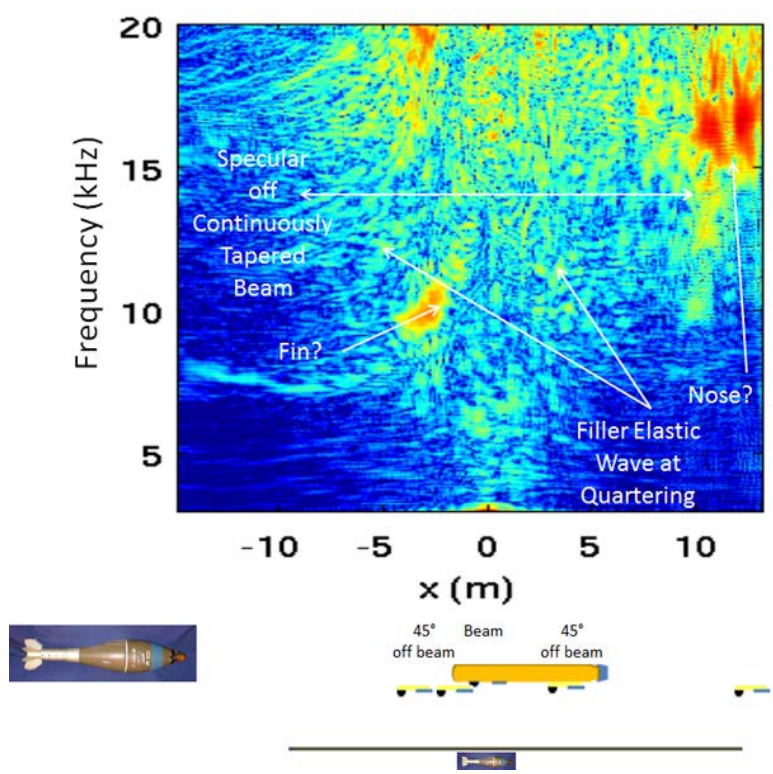

Figure 53. Acoustic color plots (arbitrary decibel units), i.e. target scattering levels versus frequency and x position of the receiver for target N9, the 120mm mortar buried horizontally. We have illustrated beneath the plots the various source (black sphere) and receiver (blue bar) locations along x to help one visualize the source/receiver angles relative to the x axis of the color plots.

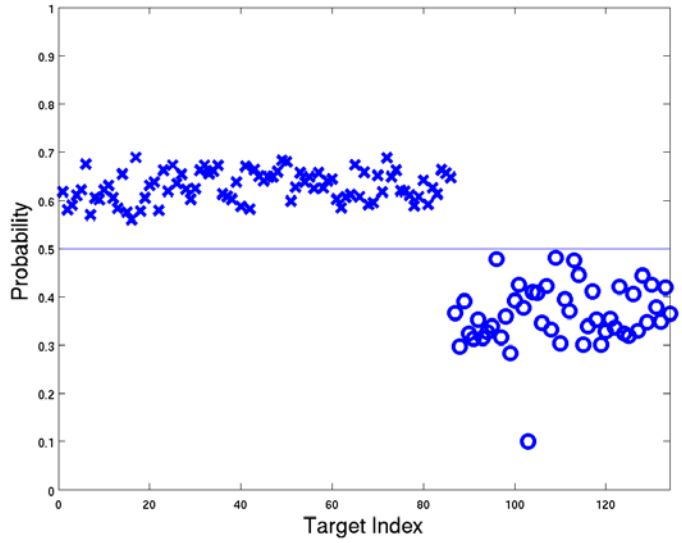

Figure 55. Probability that a target detected on a particular receiver is a UXO using the product of the probabilities shown in Fig. 54.

We assessed the amount of target strength SA (acoustic color) feature separation among the nine buried UXO, the two buried non-UXO, and the seven proud non-UXO targets. The features were extracted from the associated narrowband complex pressures as a function of receiver positions x and y. These complex scattered pressure values were extracted from the data for a fixed y co-ordinate (a particular receiver on the BOSS wing) at 39 equally spaced x co-ordinates (the flight path direction) as the AUV flew by. These 39 echo level values were then determined for each of the 383 frequencies in the 3 to 13 kHz band giving a ~15,000 dimensional feature for each of the 40 y positions on the receiver array. Regarding bandwidth, although data was collected up to 20 kHz, the RVM study was limited to frequencies 13 kHz and below to stay within the Nyquist sampling rate as determined by the receiver spacing (Δy) on the wings and the vehicle speed•Δt (Δx). The RVM identification algorithm was then trained with the even indexed y positions and tested on the odd. East/west and diagonal paths which presented reasonable target images were used. For a typical target, there were on average about six such paths. Overall, the training data as well as the testing data were based on approximately 120 realizations of the ~15,000 dimensional feature for each of the eleven buried targets - three 5 inch rockets, five 155mm projectiles, a 120mm mortar, a large rock and a cinder block and each of the seven proud non-UXO targets – a rock, a 55 gallon water-filled drum, a 5:1 aspect telephone pole section, a flat panel, a 2:1 aspect telephone section, a cement block, and a rubber tire. This resulted in over 2100 entries in the target/probability display shown in

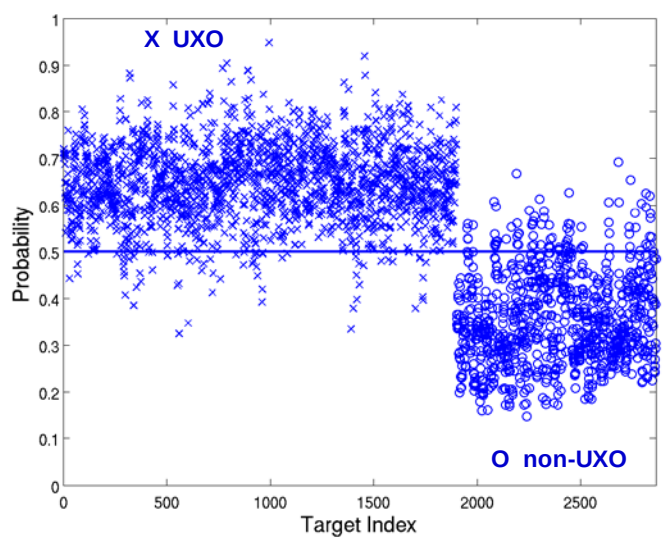

Figure 54. Probability that a target detected on a particular receiver is a UXO.

Fig. 54 where the probability (0 to 1) of being a UXO target is represented for the eighteen targets. It is important to note that in this display, different flight paths and y values for a specific target are treated as separate realizations. For the most part, there is good UXO/false target separation of this multi-dimensional TS feature for most of the targets. The failure to produce good UXO / false target separation for some realizations (~ 90 UXO realizations and ~ 60 non-UXO realizations), indicates that there are important differences in the measured acoustic color constructs ($TS_y(x,\omega)$) along the wing receivers and among the flight paths for some of the targets. (Note that there is only a relatively small number (~150) of outliers among the 2800 entries.)

In the above, the data from different flight paths/y positions for any specific target are treated as separate realizations. However, if the probabilities from the 20 y positions used for detecting a specific target are combined, one gets perfect results. Here, we use the combinatorial probability given by the product of the individual n probabilities raised to the 1/n power. When this is done, all the UXO targets now separate from all the buried and proud non-UXO targets as shown in Fig. 55. This indicates that the particular features used here can indeed provide the necessary "fingerprints" for our target classifier. The fact is that for any particular target, the flight path parameters of the wing receivers over which the target is detected can introduce some variation in the measured target strength. The added uncertainty in the resulting features leads to an RVM classifier exhibiting a less than perfect (although good) ROC curve. However, the 100% performance resulting from the combined probabilities is very encouraging suggesting further analysis to develop more robust geometric sampling strategies. The existence of robust classifying features would also promote the development of practical training methods for the ID algorithms.

Notwithstanding the encouraging feature separation performance represented in Figs.54 and 55, it is important to improve these results in two respects. (1) As can be seen in Fig. 55, the margin (separation distance between the target and non-target features) is relatively small. And (2), some realizations fail to produce target feature separation as seen in Fig.54 (~ 90 UXO realizations - the x's and ~ 60 non-UXO realizations – the o's).

Finally, we discuss the long time plan view images (see Fig. 42) in order to improve the quality of these "elastic" images which were so successfully exploited for classification in our sediment pool studies[11,14]. One of these is shown on the top in Fig. 56 for the 5 inch rocket together with the UXO diagram on the bottom indicating by color the UXO components responsible for the elastic highlights in the plan view image on the left. The features seen in this image produced in the sediment laboratory are known to be effective for identifying the target as a 5" rocket. These high quality elastic highlight images were readily obtained in the sediment pool facility where the source pressure time waveform in the water was precisely known allowing the accurate de-convolution required to remove the specular component (and the sediment interface echo) by time windowing. The equivalent images obtained in the BOSS measurements (see Fig. 47) do not present these expected elastic highlights. We believe this is at least in part due to our incomplete knowledge of the source pressure time waveform at the target. Instead, we were forced to use an estimate based upon the known electrical waveform applied to the source and the amplitude-only transfer voltage response curves provided for the source isolated from the vehicle. We can obtain the precise source waveform (amplitude and phase) in the water by means of near-field holography measurements in the NRL structural acoustic facility. These measurements would be made with the source mounted to the AUV so that all structural acoustic interactions would be properly accounted for. The resulting near-field acoustic holography measurements can be projected to any range so that we would have the precise pressure waveform incident on a particular target. We had planned to make such a measurement in our facility in the latter part of Project MR2103, but the BOSS vehicle was not available at that time. Such future studies could also lead to defining improved source requirements and/or exciting electrical waveform design. Another factor associated with the image differences is the source/receiver geometry. The sediment pool experiments were purely bi-static with the source at the center of a synthetically generated 2-D receiver array. In the BOSS exercise, the source was positioned ahead of the receiver but moving with it resulting in quasi mono-static scattering. The addition of data from the north/south paths is expected to result in improved images since in general this would provide images from orthogonal target aspects.

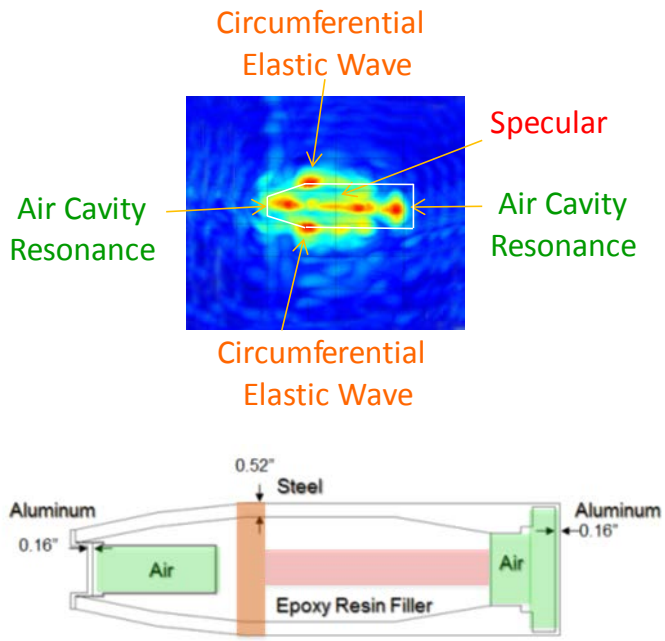

Figure 56. Elastic highlight image of 5inch rocket observed in the sediment pool (top).UXO geometry with color indicating each mechanism (bottom).

We examined the SAS images of proud and buried UXO generated and reported by a number of other researchers.[19,20,23] The Davis Point targets used in Ref. 20 included a number of empty UXO. There were no five inch rockets, but there were several 155mm shells. Although we have

not studied elastic highlight images for the 155mm shell, we would expect this target to have elastic mechanisms similar to the two shown in Fig. 56 for the five inch rocket. Examination of the images shown in Ref. 20 show no indication of elastic highlights which are so vivid in Fig 56. This is not surprising to us since the Davis Point BOSS exercise, like the Duck exercise, used a pseudo- mono-static geometry which favors the specular component over elastic effects. Further, as in the Duck exercise the pressure waveform striking the target is in reality only approximately known limiting the required deconvolutions. Similarly, we examined the images presented in Ref. 19 and found no definitive elastic highlight features. The previous comments regarding pseudo-mono-static geometry and incident pressure waveform apply as well to these measurements. Finally, we examined the SAS imagery presented in Ref 23 wherein data was collected on an aluminum shell UXO replica in a laboratory tank facility. These measurements included bi-static data. These images do show highlight-like structure with the general character of the highlight structure seen in Fig. 56. However, it is not clear whether these are indeed due to elastic scattering mechanisms.

Overall Progress in Target Classification

In this program (MR-2103) which focused our work for the first time on the large angle backscattered look down geometry, we considered several structural acoustic feature spaces and studied the effectiveness of each in separating buried UXO from buried (or proud) non UXO targets based on acoustic scattering obtained from several sonar configurations.

We began with the three feature spaces shown in Fig.5 *viz.* the two acoustic color maps (one along the buried target length and the other along the buried target radius) and the single frequency 2D spatial (x,y) target strength maps. In the acoustic color maps, features were generated by integrating target strength over a number of sub-bands and for the 2D maps by generating a band-limited target strength correlation coefficient. Using the sediment pool data for rockets buried at 0º, 30º, and 60º and 155mm shells buried at 0º, and 30º and a large buried rock and two buried cinderblocks, we established that the UXO were readily separated from the false targets for all three feature spaces. Further, using numerical simulation data we demonstrated that the receiver array aperture could be reduced significantly without seriously impacting the separation performance.

Next, we considered exploiting the fact that both acoustic color maps and images could be extracted from the acoustic scattering measured over spatially (angularly) scanned apertures within the structural acoustic frequency band. In this regard, we examined the use of two features together, *viz.* the plan view image symmetry together with the target strength correlation coefficient. In this study which used the sediment pool data, the latter feature was constructed using the numerically simulated target strength as the template. The results for a series of cases demonstrated the following: (1) that noise could be increased a fair amount without affecting performance significantly; (2) that the algorithm trained with numerical simulations for 90 different vertical burial angles still performed well and was able to classify the rocket regardless at which of three angles the target was buried; and (3) that a class-based version of this trained algorithm could work well when simultaneously testing for the five inch rocket and/or the 155mm shell. Finally, we trained the classifier using the image symmetry and target strength correlation features using only numerically simulated data for the 90 different rocket vertical

burial angles. Again using the sediment pool data for testing this numerically trained algorithm, we demonstrated the ability to classify the detected target as one of five UXOs (rocket buried at three burial angles and 155mm shell buried at two burial angles) with a probability of detection >0.99 and probability of false alarm < 0.01.

While this two feature space worked exceedingly well with the small set of false targets used in the sediment pool studies, it is important to note that the image symmetry feature might not be so effective when attempting to separate typical UXO from false targets possessing some degree of symmetry. Obvious examples would include objects such as pipes, both empty and filled barrels and drums, etc. Thus we felt that it was important to explore target separation using the acoustic color related features alone as well as image features other than symmetry.

At this point, the program focused on moving beyond the relatively benign environment of the sediment pool to 30 foot waters 2000 feet off the coast of Duck, NC. Here we used a rail-based sonar to collect buried target scattering data. In this sonar, a 2m linear hydrophone array was robotically moved perpendicular to its axis generating a partially synthetic 2m by 4m measurement array above the buried target. Because of an acoustic source failure whose impact was further exacerbated by the passing of two hurricanes, we were able to generate only crude images and no useful target strength acoustic color maps at the Duck site. Prior to the measurements, we had generated a numerical rocket target scattering data base for 90 vertical burial angles, this time using the rail-based sonar geometry and the Duck environmental parameters. We used this simulation data base to study how the symmetry feature would perform in this case compared to what we observed in the sediment pool situation. Except for two problematic burial angle regions (i.e. near 40º and 140º), the symmetry feature value was sufficiently high to suggest that a RVM classifier trained with image symmetry as a feature would perform well against non-symmetric false targets. However, in tests with the available experimental data (for the rocket buried horizontally and at 30º), the observed symmetry feature was too low to be useful as a classifying feature. We believe, however, that this is due to the poor experimental data quality and the subsequent coarse images caused by the malfunctioning source.

In an effort to explore features associated with the image not based on symmetry, we examined and tested a feature based on the image *correlation*, where the template is formed from the simulated data. First, using noise corrupted numerical data to test the algorithm, we found sufficiently high correlation parameter levels over the entire range of 90 aspects except at orientations centered on the target's beam indicating that such a feature has merit. We then tested on the available Duck measured data i.e. for the rocket buried horizontally and at 30º. We included the "no-target" case as a false target. The horizontal case produced a low correlation co-efficient as had the simulation. However, the feature for the 30º case was significantly above that for the no-target case. Given the sparse problematic experimental data obtained at Duck, we believed that we did not have reason to abandon the image symmetry feature for asymmetric false targets nor the image correlation feature in general. Both image-related features continued to be considered as effective classifying features.

The final phase of the program was carried out exploring these features from data collected with BOSS off the Coast of Panama City, FL. Since most of the nine non-UXO targets deployed at

this site possessed a degree of symmetry similar to the nine UXO targets themselves, we focused our target feature separation analysis on the acoustic color-related construct and the image correlation feature. However, regarding the latter, we point out that the elastic highlight images that were so successfully exploited in the sediment pool case were of much lower quality in the case of the BOSS data compared to those formed with the sediment pool data.

We carried out several analysis efforts regarding the use of image-based features for target ID. This included using the plan view short-time images (picking the maximum along the depth direction) generated in the BOSS exercise and extracting a feature based on correlation of a UXO image with different realizations associated with different flight paths versus correlation with different realizations of the false target images. For the most part, although the UXO correlation coefficients had a smaller spread than those for the false targets, the average correlation coefficients were not sufficiently different to effect any meaningful target separation. We also carried out this correlation feature study using the 3-D images for 22 realizations (paths) of the eight UXO targets in which we averaged the results for each individual UXO target and false target. Here only about 20 % of the false targets separated from the UXO. We then repeated this 22 UXO realization study using the plan view images (with maximum in the depth direction) and found the false target separation percentage increased to ~ 30%. We then repeated this 22 UXO realization study using the image view in depth and x and found only 4% of the false targets separated from the UXO. We concluded that use of the image correlation features for the flight paths used in this BOSS exercise would not provide robust classifying features.

In contrast, “acoustic color” related features were successfully exploited in these BOSS exercises. The “acoustic color” features were extracted from the associated narrowband complex pressures measured by BOSS as a function of receiver positions x and y, where x is along the vehicle flight path and y is along the wing receivers. These complex scattered pressure values were extracted from the data for a fixed y co-ordinate (a particular receiver on the BOSS wing) at 39 equally spaced x co-ordinates (the flight path direction) as the AUV flew by. These 39 echo level values were then determined for each of the 383 frequencies in the 3 to 13 kHz band giving a ~15,000 dimensional feature for each of the 40 y positions on the receiver array. The RVM identification algorithm was then trained with the even indexed y positions and tested on the odd using on average six east/west and diagonal paths which presented reasonable target images. Overall, the training data as well as the testing data were based on approximately 120 realizations of the ~15,000 dimensional feature for each of the eleven buried targets - three 5 inch rockets, five 155mm projectiles, a 120mm mortar, a large rock and a cinder block and each of the seven proud non-UXO targets – a rock, a 55 gallon water-filled drum, a 5:1 aspect telephone pole section, a flat panel, a 2:1 aspect telephone section, a cement block, and a rubber tire. This resulted in over 2800 entries in the target/probability display in which there is good UXO/false target separation of this multi-dimensional TS feature for most of the targets with only a relatively small number (~150) of outliers among the 2800 entries.

When the probabilities from the 20 y positions used for detecting a specific target were combined, we found that *all* UXO targets separate from *all* the buried and proud non-UXOs. This indicates that the particular features used here can indeed provide the necessary “fingerprints” for our target classifier. Notwithstanding this success, we would like to improve these results in two respects: (1) the margin (separation distance between the target and non-

target features) is relatively small and needs to be widened; and (2), some realizations (~5%) fail to produce target feature separation. The 100% performance resulting from the combined probabilities is very encouraging suggesting that further analysis to develop even more robust geometric sampling strategies can improve these two aspects of the classifier.

CONCLUSIONS AND IMPLICATIONS FOR FUTURE RESEARCH/IMPLEMENTATION

The SERDP program "Wide Area Detection and Identification of Underwater UXO Using Structural Acoustic Sensors" (MM1513 and 2009 MM Project of The Year) successfully demonstrated that scattered signals from typical UXO contain structural acoustic (SA) frequency/angle features which can be used to separate UXO from other targets[2,3] without the need for high resolution imaging[1]. In our subsequent SERDP project (MR 2103), we developed a strategy for generating constructs for extracting target classifying features from the scattering data collected by a receiver array (real or synthetic) in the water column above the sediment volume of interest. Example SA sonars include rail-based systems in which a line receiver array is moved along a fixed rail[25], AUV-based sonars such as BOSS[7] which fly over a buried target field, and sonars on towed bodies[26]. As shown earlier in Fig. 42, the constructs include: (a) the specular plan view and depth view images. These images are generated accepting all data within the echo time window so that specular scattering dominates over elastic effects allowing the formation of conventional images that conform to the target's shape[19,20]; (b) the specular-filtered plan view image[11,14]. This is generated by using time windowing to suppress specular scattering in order to produce images with elastic highlights; (c) 2-D target strength where the scattering strengths are mapped versus (x,y) at each frequency[11,14]; and (d) the target strength versus frequency as a function of x or y (or aspect[21,22]) also called acoustic color. We note that target strength shown here is defined in terms of the pressure magnitude; but we can derive features from the complex pressure as well. In June of 2013, in a collaboration with NSWC, the BOSS structural acoustic sonar was successfully flown in the Gulf of Mexico over a target field in which were buried nine NRL simulant-filled UXO's and 2 false targets and some 20 proud targets. In this study we established (1) the ability to produce both 3-D images and target strength spatial/spectral maps (acoustic color) of the buried targets and (2) that buried UXO targets and false targets can be separated using a multi-dimensional but otherwise straightforward feature set. The issues which crystalized as a result of this work are: 1. What methods, source/receiver configurations, and flight paths should be used to allow the sonar to capture echo data from the most effective aspects and angular apertures in order to support robust measured target strength spatial/spectral maps (acoustic color) as well as more exploitable acoustic images and the associated imbedded classifying features? 2. Are there additional features to be exploited, and how should these be fused? 3. What are practical effective experimental or numerical methods for training the RVM identification algorithms?

Given successful resolution of these issues and taking into account expected advances in related autonomy and processing power technologies, we envision the following capability in the not-too-distant future. At a particular site potentially requiring remedial action, sub-bottom sonar and sediment classification surveys would be conducted as part of the preliminary assessment to obtain sediment properties versus depth and range. This would be obtained by using existing sub-bottom profiling technologies. One such technology is EdgeTech's 3200-XS profiling system interfaced to an SB-216S towfish[27], an example output of which is shown in Fig.57 where one can see at this particular region (off the coast of Boston) a sandy sediment layer in the upper meter or so of the bottom and a bedrock layer about ten meters down whose depth varies along the sediment. Information about UXO types expected to be present at the site, garnered from both a preliminary assessment and subsequent site inspection studies, would be combined with information about the sediment properties (density, sound speed, etc,) and used in high fidelity structural acoustic finite element-based numerical models to provide the data required for simulation-based RVM identification algorithm training. The remedial investigation would then involve the autonomous flight of a structural acoustic sonar over the site in paths planned initially from analysis of the simulation data base. This system might be the winged BOSS or more likely a modified BOSS or newly designed system. With the autonomy technology and processing power advances expected to take place, in the not-too-distant future it is not unreasonable to envision a system in which flight paths could be altered through either goal driven autonomy[28] (GDA) software or more advanced partially observable Markov decision processes[29] (POMDP). This autonomous path-altering process would be driven by information obtained from real-time sonar detections/localization and crude "classification" calls. With or without such advanced autonomy, after the sonar completes its flight paths over the entire site, the resulting acoustic data base would be processed off-line to provide 3-D images and acoustic color constructs for all detected targets. The images can be projected onto three 2-D planes (plan view and two depth views) which will provide target locations and burial depths. Taken together, the three images will also provide target burial orientation. This information in turn will allow target shape and size estimates and target localization. Next acoustic color constructs will be processed using the trained RVM identification algorithm providing the probability that a specific target is or is not an UXO. Depending upon the degree of RVM training, specific UXO target ID calls might also be made.

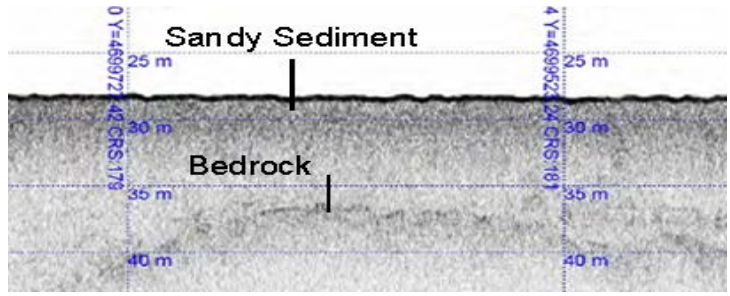

Figure 57. Example of an actual sediment profile obtained with EdgeTech's sub-bottom profiler off the coast of Boston.

LITERATURE CITED

1. B. H. Houston, J.A. Bucaro, T. Yoder, L. Kraus, and J. Tressler, J. Fernandez, T. Montgomery, T. Howarth, "Broadband Low Frequency Sonar for Non–Imaging Based Identification," IEEE Oceans 2002.

2. J. A. Bucaro, B.H. Houston, M. Saniga, H. Nelson, T. Yoder and L. Kraus, and L. Carin, "Wide Area Detection and Identification of Underwater UXO Using Structural Acoustic Sensors," 1st Annual SERDP Report, NRL/MR/7130—07-9014, January 12, 2007.

3. J.A. Bucaro, B.H. Houston, M. Saniga, A. Sarkissian, H. Nelson, T. Yoder, L. Kraus, and L. Carin, "Wide Area Detection and Identification of Underwater UXO Using Structural Acoustic Sensors – 2nd Annual SERDP Report," NRL/MR/7130—08-9103, August 12, 2008.

4. J. A. Bucaro, B.H. Houston, H. Simpson, L. Kraus, T. Yoder, M. Saniga, A. Sarkissian, and L. Carin, "Wide Area Detection and Identification of Underwater UXO Using Structural Acoustic Sensors," 3rd Annual SERDP Report, January 2009.

5. J. A. Bucaro, B.H. Houston, H. Simpson , M. Saniga, A. Sarkissian, D. Calvo, L. Kraus, T. Yoder and L. Carin, "Wide Area Detection and Identification of Underwater UXO Using Structural Acoustic Sensors," 4th Annual SERDP Report, July 21, 2010.

6. J. A. Bucaro, B.H. Houston, H. Simpson, Z. Waters, M. Saniga, S. Dey, A. Sarkissian, D. Calvo, L. Kraus, and T. Yoder, "Wide Area Detection and Identification of Underwater UXO Using Structural Acoustic Sensors," Final Report SERDP Report, July 8, 2011.

7. S. G. Schock and J. Wulf, "Buried Object Scanning Sonar for AUV's," Oceans 2003, 494-499.

8. S. Dey and D.K. Datta, "A Parallel hp-FEM Infrastructure for Three Dimensional Structural Acoustics," Int. J. Numer. Methods Eng. 68, 583-603 (2006).

9. Saikat Dey, Angie Sarkissian, Eris S. Mestreau, Brian H. Houston, and Larry Kraus, "Three-Dimensional Structural-acoustics Modeling and its Validation for Free-field and Littoral Environments," J. Acoust. Soc. Am. 125, 2702 (2009).

10. M. Tipping, "Sparse Bayesian Learning and the Relevance Vector Machine," Journal of Machine Learning Research/, vol. 1, pp. 211-244, 2001.

11. Z. J. Waters, H.J. Simpson, A. Sarkissian, S. Dey, B.H. Houston, J.A. Bucaro, and T. Yoder, "Bistatic, Above-critical Angle Scattering Measurements of Fully Buried Unexploded Ordnance (UXO) and Clutter," J. Acous. Soc. Am., vol. 132, pp. 3076–3085 (2012).

12. E. G. Williams, Fourier acoustics: Sound radiation and nearfield acoustic holography. (Academic Press, San Diego, 1999).

13. I. Ulusoy and C. M. Bishop, “Generative versus discriminative methods for object recognition,” in Computer Vision and Pattern Recognition, 297 IEEE Computer Society conference (2005), Vol. 2, pp. 258–265.

14. Joseph A. Bucaro, Zachary J. Waters, Brian H. Houston, Harry J. Simpson, Angie Sarkissian, Saikat Dey, and Timothy J. Yoder, “Acoustic Identification of Buried Underwater Unexploded Ordnance Using a Numerically Trained Classifier,” J. Acoust. Soc. Am. 132, 3614-3617 (2012).

15. H. J. Simpson and B. H. Houston, "Laboratory Measurements of Sound Scattering from a Buried Sphere Above and Below the Critical Angle." J. Acous. Soc. Am. 113, 39-42 (2003).

16. Harry J. Simpson, Brian H. Houston, and Raymond Lim, “Laboratory Measurements of Sound Scattering From a Buried Sphere Above and Below the Critical Angle,” J. Acoustic. Soc. Am. 113, 39-42 (2003).

17. J.A. Bucaro, B.H. Houston, M. Saniga, L.R. Dragonette, T. Yoder, S. Dey, L. Kraus, and L. Carin, “Broadband Acoustic Scattering Measurements of Underwater Unexploded Ordnance (UXO),” J. Acous. Soc. Am. 123, 738-746 (2008).

18. Kevin L. Williams, Eric I. Thorsos, Darrell R. Jackson, and Brian T. Hefner, “Thirty years of sand acoustics: A perspective on experiments, models and data/model comparisons,” AIP Conference Proceedings 1495, 166 (2012); DOI: 10.1063/1.4765914.

19. 8. Paul J. Carroll, “Underwater (UW) Unexploded Ordnance (UXO) Multi-Sensor Data Base (MSDB) Collection,” Final report SERDP Project MM-1507, July 2009.

20. Robert A. Leasko, Charles L. Bernstein, Richard Holtzapple, and Jesse I. Angle, “Munitions Detection using Unmanned Underwater Vehicles Equipped with Advanced Sensors,” Interim Report, ESTCP Project MR-201103, June 29, 2012.

21. J.A. Bucaro, “Wide Area Detection and Identification of Underwater UXO Using Structural Acoustic Sensors,” SERDP In-Progress Review Meeting, February 27, 2007.

22. J. A. Bucaro, B.H. Houston, M. Saniga, H. Nelson, T. Yoder , L. Kraus, and L. Carin, “Wide Area Detection and Identification of Underwater UXO Using Structural Acoustic Sensors,” SERDP Report NRL/MR/7130--06-9014 (2006).

23. R. Lim, D.E. Malphurs, K.H. Lee, J.L. Kennedy, and J.L. Lopes, “Comparisons of SAS-Processed Data from Ordnance Replicas over Various Scales: Experiments and Acoustic Models,” in Proceedings of Oceans Conference, MTS/IEEE (IEEE,2012), 1,p1.

24. M. Zampoli, A.L. Espana, K.L. Williams, S.G. Kargl, E. Thoros, J.L. Lopes, J.L. Kennedy, and P.L. Martson, “Low-to Mid-Frequency Scattering from Elastic Objects on a Sand Sea Floor: Simulation of Frequency and Aspect Dependent Structural Echoes,” J. Comp. Acoust. 20, 124007:1-14 (2012).

25. J.A. Bucaro, A. Sarkissian, B.H. Houston, H. Simpson, Z.J. Waters, D. Anon, K. Jig, S. Liskey, and T. Yoder, "SERDP MR-2103 Interim Report, Dec. 2012.

26. Steven G. Schock, Arnaud Teller, Jim Wulf, Jason Sara, and Mark Ericksen, "Buried Object Scanning Sonar," IEEE J. Oceanic Eng. 26, 677-689 (2001).

27. EdgeTech, 4 Little Brook Road, West Wareham, MA 02576: 4200FS Towfish and 4200-FSL Lightweight Towfish.

28. M. Molineaux, M. Klenk, and D. Aha, "Goal-Driven Autonomy in a Navy Strategy Simulation," Proc. 24 AAAI Conference on Artificial Intelligence (AAAI-2010).

29. Q. Zhao, L. Tong, A. Swami, and Y. Chen, "Decentralized Cognitive MAC for Opportunistic Spectrum Access in Ad Hoc Networks: A POMDP Framework," IEEE Journ. Selected Areas in Communications, 25, 589-600 (2007).

APPENDICES

A. Supporting Data

The wing BOSS system (photograph shown in Fig. A1) is designed to scan for buried underwater objects using two 1m hydrophone arrays mounted as wings of an unmanned underwater vehicle (UUV). An under-view and head-on view of the system is shown in the diagram in Fig. A2. The

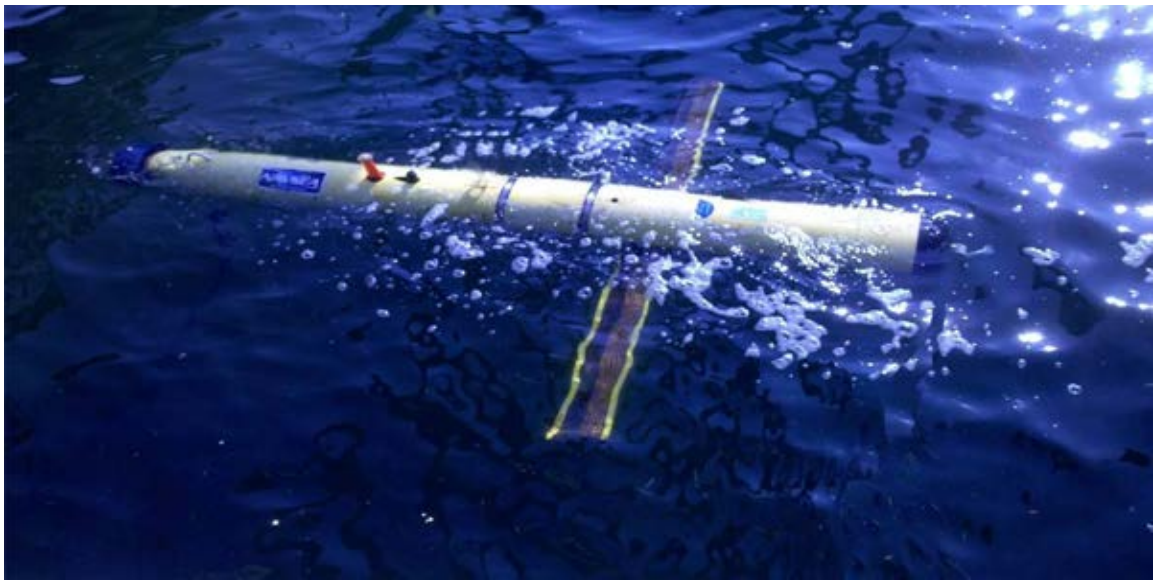

Figure A1. Photograph of BOSS in the Water.

AUV system used here is the Reliant Bluefin 12 vehicle designed and fabricated by Bluefin Robotics. (See Figure A3.) Each wing contains 20 hydrophone channels, yielding a 40-channel strip array used to collect the sonar returns. This system uses an omnidirectional projector that transmits a FM pulse over the frequency band 3-20 kHz. The wing BOSS is smaller and more mobile than the previous BOSS vehicles, as the wing arrays tend to produce less drag than the large circular array.

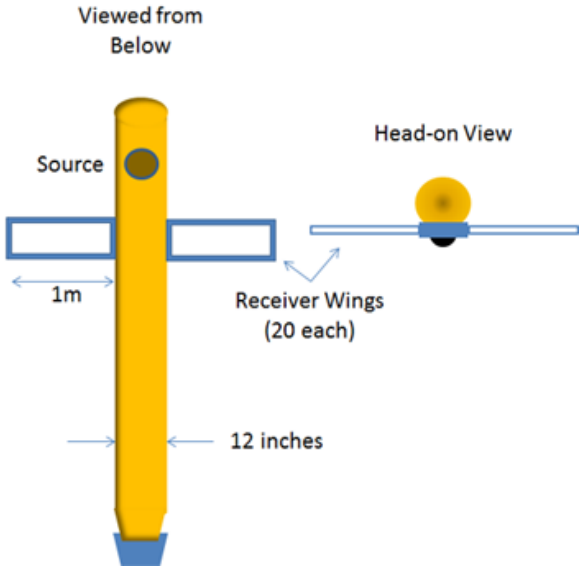

Figure A2. Plan view and head-on view of BOSS.

In order to improve the resolution of target imagery, the wing BOSS utilizes time-delay focusing extended to hydrophone data collected over several transmissions. With synthetic aperture processing, the along-track resolution of target imagery improves with distance traveled while forming the synthetic aperture. The use of synthetic aperture processing also allows the along-vehicle dimension of the array to be significantly

reduced compared to a real array thereby reducing the hydrophone array drag and surface area and increasing the ease with which BOSS can be deployed on an AUV.

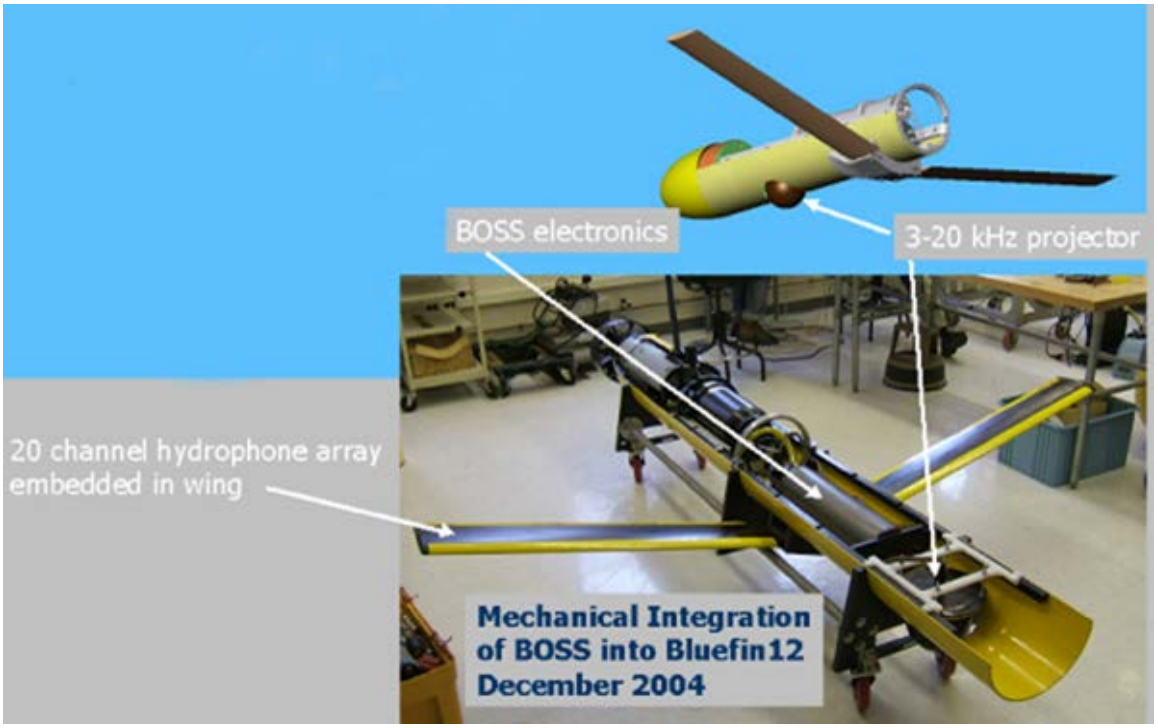

Figure A3. Photograph of BOSS prior to complete assembly showing some of the internal components.

Three-dimensional SAS imagery is generated using a navigation solution based on measurements from a Doppler Velocity Log (DVL) and an Inertial Measurement Unit (IMU) to time-delay and coherently sum matched-filtered phase histories from subsurface focal points over a large number of pings. The focused data consist of a large set of three dimensional SAS data cubes created by a sliding window of ping intervals, where adjacent data cubes have greater than 90% overlap. By using navigation/registration information, these data cubes are fused into a single large three dimensional dataset, in which each voxel's intensity is the maximum intensity of the co-registered voxels across all original data cubes. For improved image contrast, the intensity of the specular seafloor return (a shallow swath of voxels beneath the platform) is spatially nullified with an automated process employing measured backscatter statistics. Fig. A4 shows mosaics of top-view maximum intensity projections for data runs collected over the TREX13 target field in the Gulf of Mexico. These results were obtained by R. Holtzapple and N. Pineda as reported in their "Quick Look Analysis" document following the June 2013 BOSS exercises.

As can be seen in the top portion of Fig. A4, all proud and buried targets in the field of view of these 3 meter altitude west-east flights are detected via the plan view images displayed in this figure. The three 2-D images generated from these are shown for four of the buried NRL targets in the lower part of the figure. In each of these, the plan view image is repeated in the upper left

while the images with depth (*x*,*z* and *y*,*z*) are shown in the lower left and upper right images, respectively. As can be seen, the N5 and N6 (*x*,z) images correctly show horizontally buried targets while those for N7 and N8 correctly show targets buried nose up at about 30° and 60° angles.

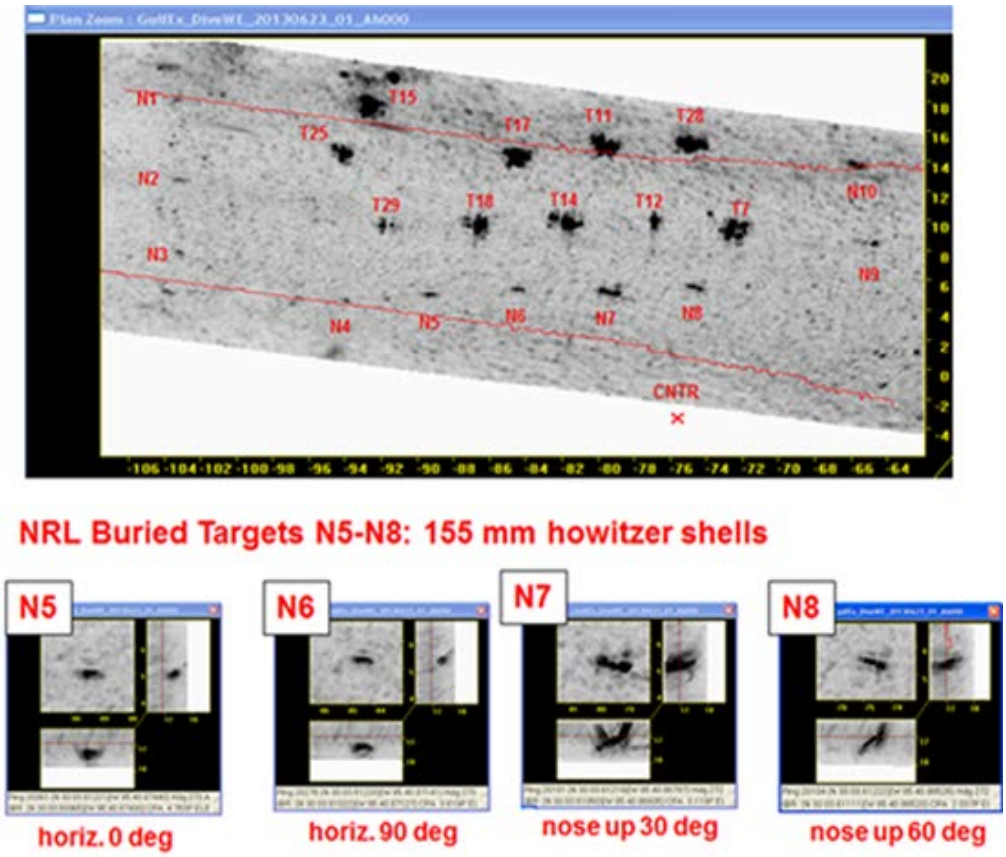

Figure A4. Preliminary 3-D images obtained from June 23, 2014 BOSS data by Richard Holtzapple and Nick Pineda.

B. List of Scientific/Technical Publications

1. Articles in peer-reviewed journals.

a) Saikat Dey, William G Szymczak, Angie Sarkissian and Joseph A Bucaro, "Scattering from targets in three-dimensional littoral and surf-zone environments with multi-layered elastic sediments based on an interior-transmission formulation", Comput. Methods Appl. Mech. Engr. 260, 24-39 (2013).
b) Angie Sarkissian, Brian Houston, Joseph Bucaro and Larry Kraus, "Near-field to far-field projection algorithm for free-field or buried scatterer," J. Acoust. Soc. Am. 133, 912-917 (2013).
c) Z. J. Waters, H.J. Simpson, A. Sarkissian, S. Dey, B.H. Houston, J.A. Bucaro, and T. Yoder, "Bistatic, Above-critical Angle Scattering Measurements of Fully Buried

Unexploded Ordnance (UXO) and Clutter," J. Acous. Soc. Am., vol. 132, pp. 3076–3085 (2012).

d) Joseph.A. Bucaro, Zachary J. Waters, Brian H. Houston, Harry J. Simpson, Angie Sarkissian, Saikat Dey, and Timothy J. Yoder, "Acoustic Identification of Buried Underwater Unexploded Ordnance Using a Numerically Trained Classifier," J. Acoust. Soc. Am. 132, 3614-3617 (2012).
e) S. Dey, A. Sarkissian, H. Simpson, B.H. Houston, F.A. Bulat, L. Kraus, M. Saniga, and J.A. Bucaro, "Structural-acoustic modeling for three-dimensional freefield and littoral environments with verification and validation," J. Acoust. Soc. Am. 129, 2979-2990 (2011).

2. Technical reports

a) J.A. Bucaro, A. Sarkissian, B.H. Houston, H. Simpson, Z.J. Waters, D. Anon, K. Jig, S. Liskey, and T. Yoder, "SERDP MR-2103 Interim Report, Dec. 2012.

3. Conference or symposium proceedings – N/A

4. Conference or symposium abstracts

a) Angie Sarkissian, Saikat Dey, Brian Houston, and Joseph A. Bucaro, "Scattering by a Cylindrical Shell Buried in an Elastic Sediment," 167th Meeting of the Acoustical Society of America, Providence Rhode Island, 5-9 May (2014).
b) Z.J. Waters, "Exploitation of above critical angle geometries in low frequency broadband techniques," Office of Naval Research Unmanned Maritime Systems Technology Review, Panama City Beach, FL, January 2013.
c) Z.J. Waters, "Acoustic imaging and structural acoustic analysis of scattering from buried targets at above-critical grazing angles," J. Acoust. Soc. Am., 130, p. 2340, November 2011.
d) H.J. Simpson, Z.J. Waters, B.H. Houston, K.K. Jig, R.R. Volk, T.J. Yoder, J.A. Bucaro, "Acoustic imaging and structural acoustic analysis of laboratory measurements of scattering from buried targets above critical grazing angles," J. Acoust. Soc. Am., 130, p. 2341, 2011.

5. Text books or book chapters – N/A

C. Other Supporting Materials

Patents – N/A

Protocols/user guides – N/A

Scientific or technical awards or honors

U.S. Naval Research Laboratory (NRL) research scientist, Dr. Brian Houston, received the Office of Naval Research Dr. Arthur E. Bisson Prize for Naval Technology Achievement Award, April 24, 2013, for his exceptional technical and engineering leadership in the development, demonstration, and transition of a new broadband underwater mine hunting sonar.